# Bio-inspired Cellulose Nanocomposites

**Karthik V. Pillai**

Dissertation submitted to the faculty of the Virginia Polytechnic Institute and State University in partial fulfillment of the requirements for the degree of

**Doctor of Philosophy**

**in**

**Macromolecular Science and Engineering**

Scott H. Renneckar, Chair

Alan R. Esker

Charles E. Frazier

Kevin J. Edgar

Maren Roman

April 26, 2011
Blacksburg, Virginia

Keywords: Nanocellulose, Nanocomposite, Biomimetic, Layer-by-layer (LbL), QCM-D, AFM

**Bio-inspired Cellulose Nanocomposites**

Karthik V. Pillai

# Abstract

Natural composites like wood are scale-integrated structures that range from molecular to the macroscopic scale. Inspired by this design, layer-by-layer (LbL) deposition technique was used to create lignocellulosic composites from isolated wood polymers namely cellulose and lignin, with a lamellar architecture. In the first phase of the study, adsorption of alkali lignin onto cationic surfaces was investigated using a quartz crystal microbalance with dissipation monitoring (QCM-D). Complete coverage of the cationic surface with alkali lignin occured at low solution concentration; large affinity coefficients were calculated for this system at differing pH levels. Adsorption studies with organosolv lignin in an organic solvent, and spectroscopic analysis of mixtures of cationic polymer with alkali lignin revealed a non-covalent interaction. The work demonstrated how noncovalent interactions could be exploited to molecular organize thin polyphenolic biopolymers on cationic surfaces. The second phase of the study examined the adsorption steps during the LbL assembly process to create novel lignocellulosic composites. LbL assembly was carried out using oxidized nanocellulose (NC) and lignin, along with a cationic polymer poly(diallyldimethylammonium chloride) (PDDA). QCM-D was used to follow the sequential adsorption process of the three different polymers. Two viscoelastic models, namely Johannsmann and Voigt, were respectively used to calculate the areal mass and thickness of the adsorbed layers. Atomic force microscopy studies showed a complete coverage of the surface with lignin in all the deposition

cycles, however, surface coverage with NC was seen to increase with the number of layers. Free-standing composite films were obtained when the LbL process was carried out for 250 deposition cycles (500 bilayers) on a cellulose acetate substrate, following the dissolution of the substrate in acetone. Scanning electron microscopy of the cryo-fractured cross-sections showed a lamellar structure, and the thickness per adsorption cycle was estimated to be 17 nm. The third phase of the study investigated the effect of LbL ordering of the polymers versus a cast film composed of a blended mixture of the polymers, using dynamic mechanical analysis. A tan $\delta$ peak was observed in the 30 – 40 ºC region for both films, which was observed in the neat NC film. Heating of the samples under a compressive force produced opposite effects in the films, as the LbL films exhibited swelling, whereas the cast films showed densification. The apparent activation energy of this transition (65 – 80 kJ $mol^{-1}$) in cast films, calculated based on the Arrhenius equation was found to be coincident to those reported for the $\beta$ transition of amorphous cellulose. The peak was seen to disappear in case of LbL films in the second heat, whereas it was recurring in case of cast films of the blended mixture, and neat NC films. Altogether, the work details a novel path to integrate an organized lignin and cellulose molecular structure, albeit modified from their native form, into a three-dimensional composite material.

# Acknowledgements

I would like to express my most sincere gratitude to my major advisor Dr. Scott Renneckar for his invaluable help and support during this endeavor. I would like to take a few leaves out of his book, especially on being patient, and not losing cool, which I am sure I have tested many times. I really appreciate his spirit of thinking out of the box, and his receptiveness to new ideas, exemplified by the countless hours I have spent in his office discussing potential research topics. I thank him for being a good friend and wish him all the very best in his career and life.

I would also like to thank my committee members Dr. Kevin J. Edgar, Dr. Charles E. Frazier, Dr. Alan R. Esker and Dr. Maren Roman for their valuable input and constructive criticisms, which has helped this work very much. I am also very thankful to all of them for allowing me easy access to the resources in their labs.

The staff members of the Wood Science and Forest Products Department have been very helpful and have always been very friendly. I would like to thank Angela Riegel and Debbie Garnand for all the administrative help. Thanks to David Jones and Kenny Albert (retired) for their help in the wood and metal shops respectively. Special thanks to Rick Caudill for his help on a lot of undefined tasks and for always being very friendly.

I thank my good friends Dr. Sudip Chowdhury and Dr. Fernando Navarro for their help with DMA and AFM respectively, and also for their good friendship. I would also like to thank Stephen McCartney at the Nanoscale Characterization and Fabrication Laboratory for his help with the SEM.

My lab-mates at the ‘SAWMIL group’ have been a great bunch of people to be around with. I want to thank them for their good friendship, constructive criticisms and questions at group meetings, and also for the support they have given me. I wish them all the very best.

I would like to thank my family members and friends for giving me the moral and inspirational support.

Last, but definitely not the least, there are no words to describe how thankful and grateful I am to my dear wife Remya for all her sacrifices and support to see me finish my Ph.D. This work is as much hers as it is mine.

***Dedicated to my dear wife and baby***

# Table of Contents

# List of Figures

# List of Tables

# Chapter 1. Introduction

Naturally occurring materials have the unique combination of toughness and stiffness as a result of controlled arrangement and organization of the constituent materials into hierarchically ordered structures.[1, 2] Classical examples of such materials are wood and bone, which are formed in living organisms under ambient conditions of pressure and temperature. Assembly of these materials occurs in an aqueous medium creating a highly energy efficient process guided by cellular control.[3] Wood is mostly composed of a lignified secondary cell wall, which in simplest terms is a nanocomposite composed of cellulose microfibrils embedded in a matrix of hemicellulose and lignin.[4] The unique properties of woody materials have made them valuable as structural, textile, pulp and paper products, etc., among many possible uses. Additionally, there is a growing interest in these materials as feedstocks for our energy and materials needs thereby reducing our reliance on petroleum-based products.

Nature uses a scale-integrated approach to reap the benefits of the respective nanoscale building blocks. For synthetic composites, blending nanoparticles in a polymer matrix can lead to significant improvement in mechanical and thermal properties compared to the neat polymer.[5, 6] The use of cellulose whiskers as a reinforcement in a latex matrix was first carried out by Favier et al.[6] They used cellulose nanocrystals (CNCs) obtained by acid hydrolysis from mantles of tunicates, which had a width of 10-20 nm, lengths of several microns, and an aspect ratios on the order of 100. As a result of the reinforcement, they observed an increase in the shear modulus of the composite material in the rubbery state (1.0 MPa to 100 MPa). Following this initial study, a multitude of

works on cellulose nanocomposites have been published and a detailed review of the use of CNCs in nanocomposites was written by Samir et al.[7] Solution casting of composite films from aqueous systems with water soluble matrix polymers or latex is the most studied procedure due to the stability and dispersibility of CNCs in water. In order to use organic solvents for solution casting, the CNCs need to be either coated with surfactants or chemically surface-modified by attaching different functionalities.[7]

Another technique for creating thin films of nanoparticles is the layer-by-layer (LbL) deposition technique,[8-11] which can be used to obtain freestanding thin films.[12] LbL films with CNCs and microfibrillated cellulose (MFC) have recently been published.[13-16] In contrast to CNCs, MFC is created by unraveling the microfibril structure of the cell wall using severe mechanical treatment.[17, 18] This material is unique with its ribbon like 50 nm diameter fibrils. However, the isolation method is energy intensive with a resulting distribution of fibril diameters. Since its discovery, MFC has been produced with pretreatment stages that lower the energy requirement by loosening the hydrogen bonds amongst fibrils with enzyme and chemical treatments.[14, 19] Recently, interest in nano-cellulosic materials that have dimensions of carbon nanotubes has led to the development of a low energy method for isolation of the now commonly referred to nanocellulose.[20, 21] This method uses a commercially known process to oxidize the cellulose pulp fibers in a heterogeneous solution.[22] As a result, the fibrils within the fibers are substituted with carboxylate salts, and a combination of repulsive forces and hydrodynamic pressure is used to overcome the myriad of hydrogen bonds holding the fibrils together. Nanocellulose suspensions of the elementary fibril (3-5 nm diameter) are directly

produced from the TEMPO (2,2,6,6-tetramethyl piperidine-1- oxyl)-mediated oxidized pulp using mechanical agitation from a blender or ultrasonicator.[20, 23] The use of nanocellulose in a bio-based nanocomposite was reported for the first time by Johnson et al.[23] They manufactured solution cast films of hydroxypropyl cellulose reinforced with nanocellulose, with a loading of nanocellulose up to 5%. Their results showed an improved fiber matrix interaction as evidenced by the higher values of storage modulus under elevated temperatures, compared to a similar system reinforced with CNCs and MFC.[23]

In plants, the combination of strength and interfacial stability is achieved by coating cellulose with matrix polysaccharides that can interact with other cell wall polymers like lignin in secondary cell walls and proteins in primary cell walls.[24] According to the commonly accepted model of secondary cell wall in plants, the cellulose microfibrils are coated with hemicellulose to form larger units, which are embedded in a lignin-hemicellulose matrix in a distinct lamellar pattern.[25] This structure has evolved over millennia and nature has selected that this organization offers the best performance for the survival of the plant. Analogous structural motifs of the lamellar architectures are found in biological materials such as ivory, horn, bone, and nacre. The crux of this dissertation is to understand how this lamellar architecture at the nanoscale enhances performance of the structure.

## 1. 1 Research Questions

- What factors influence lignin adsorption onto a cationic surface from solution?

- Can free-standing lamellar-structured LbL films be prepared from nanoparticles obtained from wood (nanocellulose and lignin)?

- Does the lamellar structure impact performance for films of cellulose and lignin relative to a randomly-oriented cast film of the same materials

The goal of this study is to build composite films with controlled molecular structure from isolated building blocks of wood using non-covalent interactions. This study is divided into three parts; *Chapter 4* quantifies the adsorption of lignin to cationic surfaces, elucidating potential mechanisms for templating; *Chapter 5* of the study quantifies build-up of LbL films and shows a route for the creation of free standing wood polymer films; and *Chapter 6* investigates how ordered structure influences dynamic mechanical properties of the materials using parallel plate rheology. The significance of this study lies in the interest of going beyond current technologies to utilize plants to derive chemicals and fuels. Cellulose is often quoted as the most abundant polymer on earth, however it is always closely integrated with lignin, and this is the crux of truly making biobased fuels and chemical platforms from renewable feedstocks a reality. New model substrates of the cell wall with known composition would allow the integration of samples into many state-of-art chemical and imaging equipments to follow real-time deconstruction of the cell wall materials.

## 1. 2 References


1. Baer, E.; Hiltner, A., *Phys. Today* **1992,** 45, 60.
2. Science, N. A. o., *Heirarchical structures in biology as a guide for new materials technology*. National Academy Press: Washington DC, 1994.

3. Teeri, T. T., Brummer III, H., Daniel, G., Gatenholm, P., *Trends Biotechnol.* **2006,** 25, 299-306.

4. Fengel, D.; Wegener, G., *Wood-Chemistry, Ultrastructure, Reactions*. Walter de Gruyter: New York, 1989.

5. Kojima, Y.; Usuki, A.; Kawasumi, M.; Okada, A.; Fukushima, Y.; Kurauchi, T.; Kamigaito, O., *J. Mater. Res.* **1993,** 8, 1185-1189.

6. Favier, V.; Canova, G. R.; Cavaillé, J. Y.; Chanzy, H.; Dufresne, A.; Gauthier, C., *Polym. Adv. Technol.* **1995,** 6, 351-355.

7. Samir, M. A. S. A.; Alloin, F.; Dufresne, A., *Biomacromolecules* **2005,** 6, 612-626.

8. Decher, G.; Hong, J. D.; Schmitt, J., *Thin Solid Films* **1992,** 210, 831-835.

9. Schmitt, J.; Gruenewald, T.; Decher, G.; Pershan, P. S.; Kjaer, K.; Loesche, M., *Macromolecules* **1993,** 26, 7058-7063.

10. Lvov, Y.; Decher, G.; Moehwald, H., *Langmuir* **1993,** 9, 481-486.

11. Decher, G., *Science* **1997,** 277, 1232.

12. Mamedov, A. A.; Kotov, N. A., *Langmuir* **2000,** 16, 5530-5533.

13. Podsiadlo, P.; Choi, S.-Y.; Shim, B.; Lee, J.; Cuddihy, M.; Kotov, N. A., *Biomacromolecules* **2005,** 6, 2914-2918.

14. Wågberg, L.; Decher, G.; Norgren, M.; Lindstrom, T.; Ankerfors, M.; Axnas, K., *Langmuir* **2008,** 24, 784-795.

15. Jean, B.; Dubreuil, F.; Heux, L.; Cousin, F., *Langmuir* **2008,** 24, 3452-3458.

16. Medeiros, E. S.; Mattoso, L. H. C.; Bernardes-Filho, R.; Wood, D. F.; Orts, W. J., *Colloid. Polym. Sci.* **2008,** 286, 1265-1272.

17. Herrick, F. W.; Casebier, R. L.; Hamilton, J. K.; Sandberg, K. R., *J. Poly. Sc.* **1983,** 37, 797-813.

18. Turbak, A. F.; Snyder, F. W.; Sandberg, K. R., *J. Poly. Sc.* **1983,** 37, 815-27.

19. Paakko, M.; Ankerfors, M.; Kosonen, H.; Nykanen, A.; Ahola, S.; Osterberg, M.; Ruokolainen, J.; Laine, J.; Larsson, P. T.; Ikkala, O.; Lindstrom, T., *Biomacromolecules* **2007,** 8, 1934-1941.

20. Saito, T.; Nishiyama, Y.; Putaux, J.-L.; Vignon, M.; Isogai, A., *Biomacromolecules* **2006,** 7, 1687-1691.

21. Saito, T.; Kimura, S.; Nishiyama, Y.; Isogai, A., *Biomacromolecules* **2007,** 8, 2485-2491.

22. Saito, T.; Isogai, A., *Cellulose Communications* **2004,** 11, 192-196.

23. Johnson, R.; Zink-Sharp, A.; Renneckar, S.; Glasser, W., *Cellulose*.

24. Teeri, T. T.; Brumer III, H.; Daniel, G.; Gatenholm, P., *Trends Biotechnol.* **2007,** 25, 299-306.

25. Uhlin, K. I.; Atalla, R. H.; Thompson, N. S., *Cellulose* **1995,** 2, 129-144.

# Chapter 2. Literature Review

## 2. 1 Introduction to Composite Materials

### 2. 1. 1 Synthetic Composites

Atoms are composed of electrons, neutrons and protons; molecules are composed of atoms; and at the nanoscale materials are composed of large molecules or molecular aggregates. Many materials, like wood, sedimentary rocks and metal alloys appear as homogeneous materials on a macroscopic scale, when in fact they are composed of different constituents where there is specific order at molecular, nano-, and micro- scales. Dietz [1] gave the following definition for a composite material: "composites are combinations of materials differing in composition or form on a macro scale, and the constituents retain their identities in the composite, that is, they do not dissolve or otherwise merge completely into each other, although they may act in concert". From a materials engineering stand point, a composite material consists of an assemblage of two materials of different nature allowing mankind to obtain a material of which the set of performance characteristics are greater than that of the components taken separately. In the most general case, a composite material consists of one or more discontinuous phases distributed in one continuous phase. The discontinuous phase is usually harder and with mechanical properties superior to those of the continuous phase, although there are exceptions, such as rubber-toughened epoxy.[2] Composites take many forms; they may consist of particles or fibers distributed in a matrix; they may be layered materials laminated together; and they may be organic, metallic, ceramic, or a combination of these. In load-bearing or structural applications, composites in most cases comprise a bulk phase enclosing a fibrous reinforcing phase. The bulk phase is called the matrix and

the fibrous material is called the reinforcement. The matrix binds the reinforcement together, transfers the external load to the reinforcement and protects it from external environmental factors such as high temperatures, water, UV, etc. The matrix also gives the composite its shape, appearance and provides for the overall durability. The fibrous reinforcement carries most of the structural loads and for the most part dictates the stiffness and strength of the composite.[3] Based on the form of the reinforcement, composite materials can be classified either into a fiber or particle composite. Fibers differ from particles because the latter does not have a directional dependence on properties. Based on the nature of the matrix material, the composite may be classified as organic, metallic or mineral matrix composites.[3]

### 2. 1. 2 Nanocomposites

The incorporation of nanoparticles into polymers is a design concept that is used in many areas of material science. The concept is attractive because it enables the creation of materials with new or improved properties by mixing multiple constituents and exploiting synergistic effects. One important thrust is the development of structural materials with improved mechanical and thermal characteristics.[4] Nanocomposites are characterized by an extremely fine dispersion of a phase of nanometer scale within a polymer matrix. The extremely small size of the nanometer scale phase/filler gives the composite material advantages over conventional composites.[5] Nanoparticles include carbon nanotubes, clay particles, CNCs, and metals among many others, and are characterized by very high aspect ratios and moduli. One important advantage of using nano-reinforcement or nano-fillers is that only a small amount (1-5%) of the nano-material is required for the desired property enhancement. This result is due to the dramatic increase in surface area of the

nano-particles from conventional reinforcements or fillers. However, incorporation of these particles into composites is not always accompanied by an improvement in properties, due to poor dispersion.[6]

Polysaccharides, especially cellulosics, are a very promising source of nanoparticles of different geometries and properties. These nanoparticles are also amenable to surface modification using well established carbohydrate chemistries.[7] Cellulose nanocrystals (CNCs), which have very high aspect ratios, have been used as reinforcing particles in composite materials.[8] CNCs have been shown to be very high modulus materials. Raman spectroscopic analysis of cellulose chain deformations of tunicin derived CNCs yielded a high elastic modulus value of 143 GPa.[6] CNCs from a variety of sources have been used as reinforcing filler with different types of polymer matrices.[9] CNCs were first used as reinforcement in a latex matrix composed of poly(styrene-co-butyl acrylate). The resultant composite was found to have an increase in shear modulus by two orders of magnitude.[10] Since this first report, CNCs obtained from different sources have been used to reinforce synthetic[11-14] as well as natural polymer matrices.[15-19] Although there are several advantages, the negative aspects of using cellulosics are their poor miscibility with non-polar petroleum-based thermoplastics, difficulty in processing at higher temperatures due to their degradation above 200°C, and high moisture absorption, which leads to dimensional changes and decrease in mechanical properties.[8]

### 2. 1. 3 Natural Nanocomposites: Hierarchical Scale Integrated Structures

Materials found in nature have properties that are not present in synthetic materials because nature has devised techniques to organize molecules in hierarchical organization over several length scales. Biological structures are characterized by hierarchical

architectural designs in which organization is controlled on length scales ranging from molecular, nano-, micro- to the macroscopic.[20] These materials are multifunctional and are produced *in situ* at room temperature and atmospheric pressure. Moreover, nature achieves blending of dissimilar materials (hard and soft or hydrophobic and hydrophilic phases) through highly organized events. Intermolecular interactions play a key role in the assembly of secondary and tertiary structures[21]. One example is the mixing of cellulose and lignin components within the plant cell wall (Figure 2. 1). Examples of such organization can be found in wood and bone, which are structural composites that provide multiple and precise functions to the organisms.

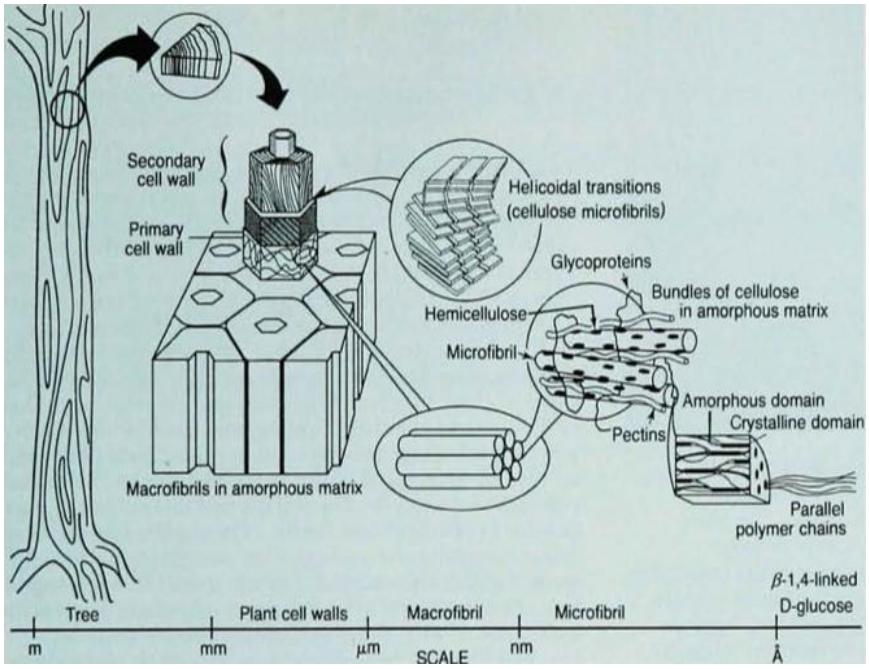


**Figure 2. 1** Hierarchical organization of cellulose from molecular to macroscopic scale (Baer, E.; Hiltner, A., *Phys. Today* **1992**, 45, 60-67, used under the fair use guidelines, 2011).

This integral organization has enabled trees to grow and become the largest organisms on the planet with lignin providing for vertical competition amongst terrestrial adapted plants. A similar model for a multiphase material is found in bone, a protein-inorganic

composite,[23] where a nano-scale inorganic component (hard phase) such as hydroxyapatite is grown within the collagen-based tissue (soft phase).[24] Natural systems ensure maximum extent of interfacial contact amongst domains with hybrid properties that are different from the individual bulk materials. The characteristics of hierarchical biological material systems are: recurrent use of molecular constituents; controlled orientation of structural elements; durable interfaces between hard and soft materials; sensitivity and critical dependence on water; properties that can vary in response to requirements; fatigue resistance and resiliency; controlled and complex shapes and self-repair.[20]

## 2. 2 Bio-emanent Materials – Copying Nature in vivo and in vitro

As described in the previous section, biological composites are generally organized on discrete scale levels or hierarchical order ranging from molecular to macroscopic. The components are held together at each level by specific interactions and organized to optimize the ultimate function of the whole system. The concept of hierarchical organization in synthetic composite technology is new, and in the future, composite technology will increasingly imitate life within the constraints of the industry.[22] In this context, the concept of bio-emanent materials may offer solutions to the challenge of incorporating scale integrated structures or hierarchical order in synthetic composites.

The term "bio-emanent material" describes a material that owes its origin to a biological process.[25] A biological process might have been involved in one or more stages of synthesis, or a biological process or microstructure may have served as the inspiration or template for the structure of the material. According to Viney,[25] the broad term bio-

emanent materials can be subdivided into the following categories; biosynthesized, bioderived, biomimetic, and bioduplicated.

- **Biosynthesized**: A material synthesized by an organism
- **Bioderived**: Biosynthesized materials that have been subjected to post-harvesting derivatization or to significant other additional processing steps.
- **Biomimetic**: The microstructure copies that of a natural material, but at least the processing steps by which the microstructure is obtained are entirely artificial.
- **Bioduplicated**: Hierarchical structures produced by synthesis and process routes that approach those in nature. However, they need not duplicate those of an organism.

The value and logic behind following the route of bioduplication may be questioned considering the complexity of the processes involved. The synthesis of natural polymers, even the simplest of them, involves complex biosynthetic pathways and action of more than one type of enzyme. The complexity of these biochemical pathways precludes their economical *in vitro* duplication in the foreseeable future. Moreover, it is extremely difficult, if not impossible, to duplicate the spatial organization of the chemistry of thousands of chemical reactions that occur simultaneously in a small volume within the confines of living cell.[25] Therefore, biomimetic materials offer a route of material production for systems *in vitro*, framed with given boundary conditions, to engineer materials with properties that may approach their natural analogs.

## 2. 3 Wood

Wood is an organic material constituting the primary component of the stems of woody plants, especially trees, but also shrubs. These perennial plants are characterized by stems

that grow outward and upward year after year. Woods and the plants that produce them are divided into two categories: hardwoods and softwoods. Although hardwoods and softwoods fall under the same botanical division, spermatophytes (seed producing), they belong to two different subdivisions, namely *angiospermae* and *gymnospermae*, respectively. Angiosperms are characterized by production of seeds within ovaries, whereas gymnosperm seeds lack this covering and hence are commonly termed as naked seeded plants.[26]

### 2. 3. 1 Ultrastructure and Formation of Wood

Woody tissue originates from the vascular cambium. There are two types of cambial cells, namely fusiform initials and ray initials. The periclinal division of fusiform initials leads to the formation of two kinds of cells, of which one becomes another fusiform initial and the other becomes either a xylem or phloem mother cell. The xylem or phloem mother cell may undergo one or more divisions before transforming into a fully formed xylem or phloem. Ray initials, as the name suggests, are the precursors of ray cells.[26]

During xylem differentiation, thin walled precursor cambial cells undergo dramatic transformations including secondary cell wall deposition, bordered pit formation, lignification and programmed cell death.[27] The developing xylem of wood is highly specialized for secondary cell wall production with a biochemical commitment to lignifications.[28] During secondary wall formation, a complex architecture of polysaccharides is first established and the resulting structure is impregnated with lignin precursors that are polymerized by *in situ* protein catalysts.[29] Between two adjacent cells, there is a middle lamella rich in pectic substances that hold the cells together. Though individual cellulose fibrils might cross the middle lamella, this layer has very little

cellulose (Figure 2. 2). The transition from middle lamella to the adjacent cell wall layers is not well defined, therefore the middle lamella and adjacent primary cell walls are together termed as a compound middle lamella.[30] The thin expandable primary cell wall of cambium cells contains relatively more xyloglucans and pectins, and a lesser amount of cellulose than secondary walls, which consist of extensive cellulose deposition embedded in hetero-polysaccharides.[31] The secondary wall deposits on the inner surfaces of the existing primary wall, thereby reducing the size of the cell lumen. Completion of cell enlargement and differentiation is followed by cell death. According to the generally accepted terminology, the cell walls of tracheids are divided into several concentric layers.[32,33] The secondary cell walls of tracheids are composed of three structurally distinct layers termed as S1, S2 and S3, as shown in Figure 2. 2. The S1 layer is the layer closest to the primary cell wall, followed by S2 and S3 layers. Another way to put it would be that the S3 layer surrounds the cell lumen. The concentric arrangement of cell wall layers is due to the difference in the chemical composition and also due to the different orientations of the structural elements.[30]

The major component of the secondary cell wall is cellulose, which is a homo-polysaccharide with repeating units of $\beta(1\rightarrow4)$ linked D-glucose molecules. Several chains of cellulose aggregate forming a microfibril, which serves as the reinforcement for the cell wall, much like the steel rods in reinforced concrete. The microfibrils in the three different layers (S1, S2 and S3) are deposited in different orientations called the 'microfibrillar angle'. Microfibrillar angle is defined as the angle between the microfibril and the axis of the tracheid. The angle with the tracheid axis also leads to the formation of a helix, which is denoted as either S for left-handed or Z for right-handed. Since about

80% of the entire cell wall thickness is composed of the S2 layer, the microfibrillar angle of the S2 layer is often considered synonymous to that of the entire cell wall.[34] The microfibrillar angle of the S2 layer influences mechanical properties such as shrinkage, longitudinal tensile strength and longitudinal modulus of elasticity.[35,36] S1 and S3 layers are determinants of transverse elasticity of tracheid cell walls.[37]

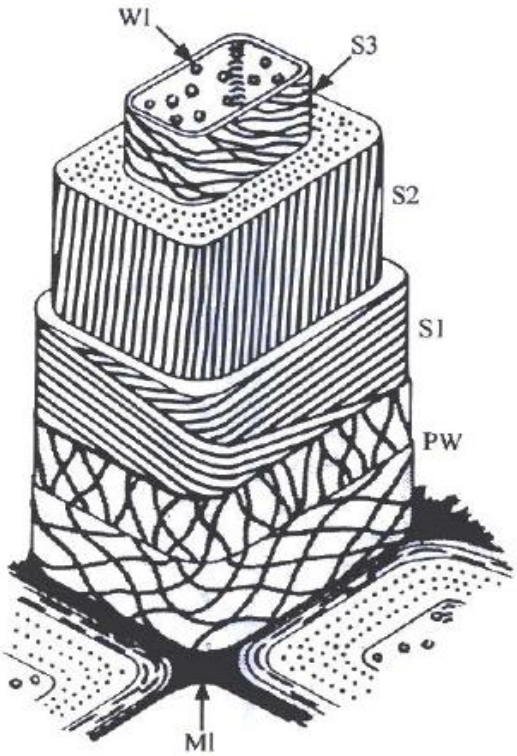


**Figure 2. 2** Model of the cell wall structure of softwood tracheids. ML = middle lamella, PW = Primary wall, S1 = secondary wall 1, S2 = secondary wall 2, S3 = secondary wall 3 and W = wart layer[30].

Meier and Wilkie[38] and Meier[39] carried out pioneering work on polysaccharide distribution within cell wall. They isolated radial sections from xylem of *Pinus sylvestris*, *Picea abies* and *Betula verucossa*, separated each into sub cellular fractions by a micromanipulator, and analyzed the monosaccharide composition of the different

polysaccharide fractions by paper chromatography. From these studies, it was concluded that, in softwood tracheids, the outer parts of the S2 layer were the richest in cellulose, while S3 layer was the richest in glucuronoarabinoxylan, and the glucomannan content gradually increased toward the lumen. On the other hand, in hardwood fibers, the inner parts of S2 and S3 were richest in cellulose, while S1 and the outer part of the S2 showed a high glucuronoxylan content. Lignification is one of the final stages of xylem cell differentiation, where lignin is deposited within the polysaccharide matrix of the cell wall by infilling of voids, and at the same time, formation of chemical bonds with the non-cellulosic carbohydrates. Lignification begins at the cell corners in the middle lamella and S1 regions, eventually spreading across the secondary wall towards the lumen. Lignification of the middle lamella and primary wall typically begins after the start of secondary wall formation, while lignification of the secondary wall usually begins when secondary wall formation is complete, as judged by the presence of an S3 layer.

### 2. 3. 2 Primary Cell Wall

Cells of both plants and animals are surrounded by a plasma membrane, but only in plants are the cells surrounded by a 'wall'.[40] The wall is located to the exterior of the plasma membrane and is itself part of the apoplast. Apoplast refers to everything that is located between the plasma membrane and the cuticle and is largely contiguous. Thus, the apoplast includes the primary cell wall, the middle lamella (polysaccharide rich region between primary walls of adjacent cells), intercellular airspaces, water and solutes.[41] In a growing cell, the primary wall and the middle lamella account for most of the apoplast. Thus, in the broadest sense, the 'wall' corresponds to the apoplast. However, for an analytical chemist, the wall is the insoluble material that remains after

the plant tissue or the cells have been homogenized and treated with aqueous buffers, organic solvents and enzymes.[42] Some authors have proposed terms such as extracellular matrix[43] or 'exocellular matrix',[44] as they considered it to be more appropriate than calling it a 'wall', because they suggested it to be a more dynamic organelle than an inert rigid box.[41] Up to 90% (dry weight) of the primary wall of higher plants is composed of polysaccharides. The rest is composed of lesser amounts of structural glycoproteins (2-10 %), phenolic esters (< 2 %), ionically and covalently bound minerals (1-5 %), and enzymes. Twelve different glycosyl residues in different amounts have been found to be the constituents of all primary cell walls. The glycosyl residues include the hexoses [D-Glucose (D-Glc), D- Mannose (D-Man), D-Galactose (D-Gal), L-Galactose (L-Gal)], the pentoses [D-Xylose (D- Xyl), L-Arabinose (L-Ara)], the 6-deoxy hexoses [L-Rhamnose (L-Rha), L-Fucose (L-Fuc)] and the hexuronic acids [D-Galacturonic acid (D-GalA) and D-Glucuronic acid (D-GlcA)].[41]

The primary walls of angiosperms and gymnosperms are composed of cellulose, hemicelluloses (xyloglucan , glucomannan or arabinoxylan), and pectic polysaccharides (homogalacturonan, rhamnogalacturonans and substituted galacturonans). Based on the structure and amount of hemicellulosic polysaccharides and relative amount of pectic polysaccharides, there are two general types of primary cell walls. Type I walls, which typically contain xyloglucan and/or glucomannan and 20-35% pectin, are found in all dicotyledons, the non-graminaceous monocotyledons and gymnosperms.[45] Type II walls are present in *Poacea* (e.g. rice and barley) and are rich in arabinoxylan, but contain <10% pectin.[46]

### 2. 3. 3 Cellulose

Cellulose is often referred to as the most abundant macromolecule on earth[46] and most cellulose is produced by vascular plants. Apart from plants, cellulose synthesis also occurs in many groups of algae, *Dictyostelium*, a number of bacterial species (including the cyanobacteria), and tunicates. Cellulose is an extracellular polysaccharide, and with the exception of bacteria and the tunicates, it is part of the cell wall in plants, algae and *Dictyostelium*.[47] Cellulose is composed of linear polymer chains of $\beta$-(1$\rightarrow$4) linked glucose residues (Figure 2. 3). Depending on the source from which cellulose is obtained, the physical properties, crystalline state, degree of crystallinity, and molecular weight may be highly variable. The crystalline state of cellulose is determined by the arrangement of the glucan chains with respect to each other in a unit cell.[47] In nature, most cellulose is produced as crystalline cellulose and is defined as cellulose I. The glucan chains in cellulose I are parallel to each other and are packed side by side to form microfibrils that in most plants are 2-3 nm thick, but which reach widths of 20 nm in certain algae.[48] Differing amounts of the two crystalline sub-allomorphs of cellulose I, namely $I_\alpha$ and $I_{\beta,}$ are found in the cellulose obtained from natural sources.[49] Cellulose $I_\alpha$ and cellulose $I_\beta$ differ with respect to their crystal packing, molecular conformation and hydrogen bonding.[50] Another kind of cellulose, namely cellulose II, has been found in a mutant form of *Acetobacter xylinum*.[51] It differs from Cellulose I in that it has antiparallel glucan chains as opposed to parallel glucan chains in Cellulose I. Amorphous or para-crystalline regions of cellulose have also been observed within the microfibril.[47] It is now widely accepted that cellulose microfibrils are synthesized by membrane-localized

‘rosette’ shaped terminal complexes, as observed by microscopy of freeze fractured plant cells.[52,47]

**→ 4)- *β* -D-Glc*p*- (1→ 4) – *β*-D-Glc*p* -(1→ 4)- *β*-D-Glc*p* -(1→ 4)- *β*-D-Glc*p* –(1→**

**Figure 2. 3** Partial structure of the β (1→4)-linked glucose units of cellulose.

Cellulose is the most abundant component of wood, accounting for almost 40-50%.[30] The chemical composition of cellulose in the secondary cell wall is the same as that in the primary cell wall. The difference is in the denser packing of cellulose microfibrils and the different orientations of the cell wall layers. Because of the denser packing and crystalline nature of the cell wall in the secondary cell wall, it appears birefringent under plane-polarized light.

### 2. 3. 4 Hemicellulose

Heteropolysaccharides, known as hemicelluloses, are defined as those plant cell wall polysaccharides that are not solubilized by hot water or chelating agents, but are solubilized by aqueous alkali. According to this definition, the hemicelluloses include xyloglucan, xylans (glucuronoxylan, arabinoxylan, glucuronoarabinoxylan), mannans (glucomannan, galactomannan and galactoglucomannan), and arabinogalactan.[41] Chemically, hemicelluloses can also be defined as plant cell wall polysaccharides that are structurally homologous to cellulose, in that they have a backbone composed of (1→ 4) linked *β*-D pyranosyl residues such as glucose, mannose and xylose, in which O4 is in the equatorial orientation. However, under this definition arabinogalactan does not fall under hemicelluloses. The structural similarity between hemicelluloses and cellulose most likely gives rise to a conformational homology that can lead to strong, noncovalent association of the hemicellulose with cellulose microfibrils.[41]

Softwood xylan consists mainly of (1→ 4) linked *β*-D Xyl*p* chains with (1→ 2) linked *α*-D-Me-Glu*p*A units and (1→ 3) linked *α*-L Ara*f* branches (Figure 2. 4). So softwood xylans can be termed as arabino-methylglucuronoxylans and comprise 5-10% of total wood.[53] The mean ratio of the three components of softwood xylan was shown to be 8:1.6: 1 (Xyl : Me-Glu*p*A : Ara) although variation may occur between species. Hardwood xylans differ from those of softwoods by the absence of *α*-L Ara*f* units and the presence of O-acetyl groups at the C2 and C3 of the xylan backbone.[30] It is an O-acetyl-4-O-methylglucurono-β-D-xylan, also called glucuronoxylan, which comprises about 10-15% of the wood and the Xyl:Acetyl: Me-Glu*p*A ratio is 10:7:1.

**→ 4)-*β*-D-Xyl*p*(1→ 4)-*β*-D-Xyl*p*(1→4)-*β*-D-Xyl*p*(1→ 4)-*β*-D-Xyl*p*(1→**

**2 3**

**↑ ↑**

**1 1**

***α*-D-Me-Glc*p*A *α*-L-Ara*f* (a)**

**→ 4)-*β*-D-Xyl*p*(1→ 4)-*β*-D-Xyl*p*(1→4)-*β*-D-Xyl*p*(1→ 4)-*β*-D-Xyl*p*(1→**

**2,3 2**

**↑ ↑**

**Acetyl 1**

***α*-D-Me-Glc*p*A (b)**

**Figure 2. 4** Partial structures of arabino-4-O-methylglucuronoxylan from (a) softwood and (b) O-acetyl-4-O-methylglucurono-β-D-xylan from hardwood.

Softwood glucomannan is a heteropolymer consisting of (1→ 4) linked *β*-D Man*p* and *β*-D Glc*p* residues to which acetyl groups (1 acetyl per 3-4 hexose units) and *α*-D Gal*p* residues are attached (Figure 2. 5). Hence the softwood mannans are normally termed as O-acetyl-galactoglucomannans and constitute about 20% of softwoods. They differ from hardwood glucomannans in that the latter do not have O-acetyl or galactose residues

attached to the glucomannan backbone chain, which may however be slightly branched[30]. They comprise about 2-5% of hardwood and the Glc:Man ratio may vary from 1:1 to 2:1 depending on species.[53]

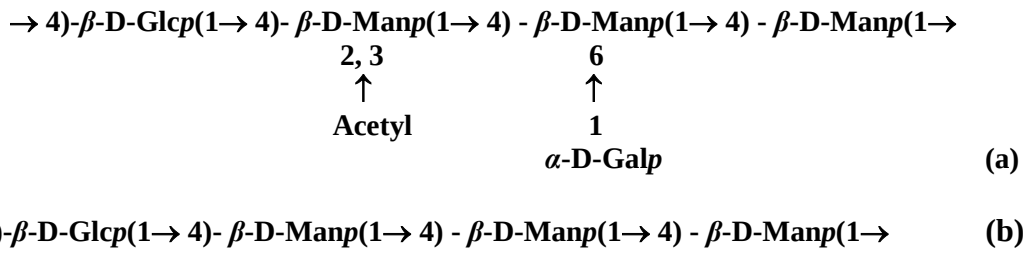


**Figure 2. 5** Partial structure of O-acetyl –galactoglucomannan from softwood (a) and glucomannan from hardwood(b).

Galactans found in gymnosperms are arabinogalactans which consist of *β*-(1→ 3) linked galactose units and side chains of *β*-(1→ 6) linked galactose, arabinose, and single galactose, arabinose and glucuronic acid units (Figure 2. 6). Arabinogalactans are water soluble and have been found in high proportions, especially from larch wood (10-25%).[30]

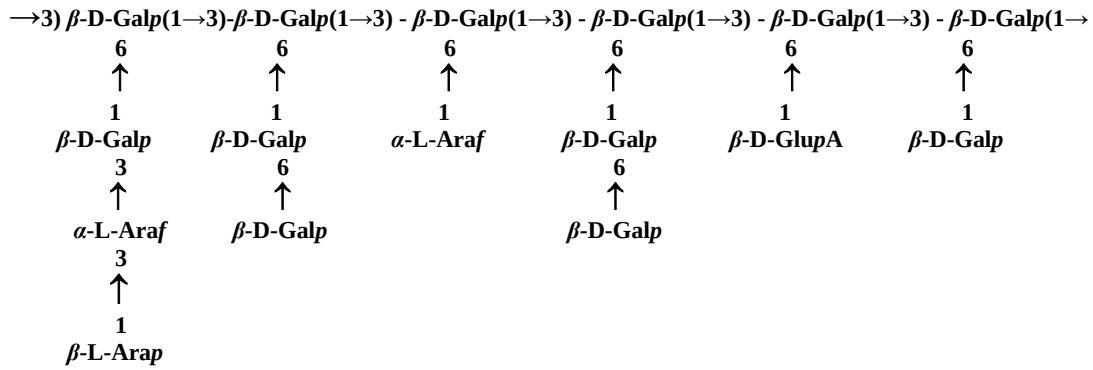


**Figure 2. 6** Partial structure of arabinogalactan from larch wood.

### 2. 3. 5 Lignin

After cellulose, lignin is the most abundant and important polymeric organic substance in the plant world. Up to one third of the woody tissue is composed of lignin, which is enzymatically polymerized from substituted phenyl propanol structures such as coniferyl

alcohol.[62] Lignification occurs at cell wall maturation when the polysaccharide and protein structures are present, creating a template for the polymerization of lignin.[63] The function of lignin in the cell wall is to act as a matrix material that binds the plant polysaccharides, thereby imparting strength and rigidity to the cell wall. Studies with radioactive carbon isotopes revealed that lignin is comprised of three p-hydroxy-cinnammyl alcohol building blocks, namely p-coumaryl(4-hydroxy cinnamyl), coniferyl (3-methoxy-4 hydroxy-cinnamyl) and sinapyl (3,5-dimethoxy-4-hydroxy-cinnamyl) alcohol (Figure 2. 10).[30] These three alcohol units give rise to p-hydroxyphenyl, guaiacyl, and syringyl units, respectively.

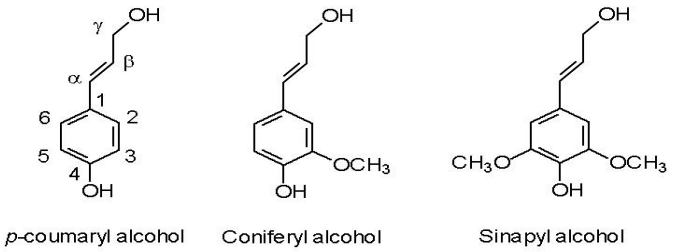


**Figure 2. 7** Lignin precursors: a) p-coumaryl alcohol, b) coniferyl alcohol, and c) sinapyl alcohol

The lignin monomers are produced in plant cells through two enzymatic pathways; the first pathway is termed shikimate pathway, wherein D-glucose is converted to either L-phenylalanine or L-tyrosine. The second pathway is called the cinnamate pathway, which converts L-phenylalanine and L-tyrosine to p-hydroxy-cinnamyl alcohol monomers.[64] The lignin monomers are synthesized in the cytoplasm within the golgi bodies or endoplasmic reticulum and released to the cell walls from vesicles as monolignols or monolignol glucosides.[29] The monolignols are polymerized to form a complex polymeric structure by C-C bonds or by ether linkages and these linkages change with respect to the location within the cell wall from the outer cell corners to the inner cell wall. The most

common linkage types found in a complex lignin molecule are $\beta$-O-4, $\alpha$-O-4, $\beta$-5, 5-5, 4-O-5, $\beta$-1 and $\beta$-$\beta$, which are possible on various locations of the phenolic unit. This polymerization of monolignols has been shown to be possible by the action of various free and bound enzyme complexes like peroxidases and oxidases associated with the plant cell wall.[29]

Approximately 93-98% of gymnosperm lignin is composed of guaiacyl units and a small proportion is composed of p-hydroxyphenyl units, whereas in angiosperms, approximately 30-45% is composed of guaiacyl and 50-75% syringyl units. The highest concentration of lignin is found in the compound middle lamella, however the highest proportion of lignin (>90%) is present in the secondary cell wall.[64]

### 2. 3. 6 Pectic Polysaccharides

Pectic polysaccharides are mostly confined to the primary cell wall, especially the middle lamella, where they act like glue to hold the adjacent cells together.[48, 54] After secondary cell wall formation, this function is mostly carried out by lignin, which also acts as water resistant glue.[28] Three types of pectic polysaccharides have been isolated and characterized from primary cell walls of plants. They are homogalacturonan, rhamnoglacturonan and substituted galacturonans.

Homogalacturonan (HG) is a linear chain of (1→ 4) linked $\alpha$-D-galactopyranosyluronic acid (Gal*p*A) residues in which some of the carboxyl groups are methyl esterified (Figure 2. 7). These polymers with a high degree of methyl esterification are referred to as pectin, whereas HGs with low or no methyl esterification is termed as pectic acid.[41]

**→ 4)-α-D-Gal*p*-A-(1 → 4)-α-D-Gal*p*-A-(1→ 4)-α-D-Gal*p*-A-(1 → 4)-α-D-Gal*p*-A-(1→**

**Figure 2. 8** A partial structure of homogalacturonan (HG).

Rhamnogalacturonans are a group of closely related cell wall pectic polysaccharides that contain a backbone of the repeating disaccharide (1→ 4)-*α*-D-Gal*p*A- (1→ 2)-*α*-L-Rha*p*.[55] Between 20 and 80% of the Rha*p* residues, depending on the plant source and the method of isolation, are substituted at the C-4 position with neutral pectic polysaccharides (Figure 2. 8). The polysaccharides consist of linear or branched arabinans, galactans and arabinogalactans.[56-59]

**→2)-*α*-L-Rha*p*-(1→4)- *α*-D-Gal*p*A-(1→2)-*α*-L-Rha*p*-(1→4)- *α*-D-Gal*p*A-(1→**
**4**
**↑**
**neutral pectic polysaccharides**

**Figure 2. 9** The backbone glycosyl-residue sequence of rhamnogalacturonan I. Neutral pectic polysaccharides can attach to C4 of the rhamnopyranosyl residues.

Substituted galacturonans are pectic polysaccharides with (1→ 4) linked *α*-D Gal*p*A backbone. Xylogalacturonans are characterized by *β*-D-Xyl*p* residues attached to the C-3 position of the Gal*p*A backbone, whereas apiogalacturonans are characterized by *β*-D-Api*f* residues attached to the C-2 position of the Gal*p*A backbone.[41]

Rhamnogalacturonan II is found in cell walls of all higher plants.[60] The glycosyl sequence of RG-II is to a large extent conserved in gymnosperms, monocotyledons and dicotyledons. Rhamnogalacturonan II is a small-molecular-mass pectic polysaccharide that can be solubilized from the cell wall using endo-polygalacturonase. Rhamnogalacturonan II contains eleven different glycosyl residues, including the unusual monosaccharides apiose, 3-carboxy-5-deoxy-L-xylose (aceric acid), 3-deoxy-D-*manno*-

octulosaric acid (Kdo), and 3-deoxy-D-*lyxo*-heptulosaric acid (Dha) as shown in Figure 2. 9.[61]

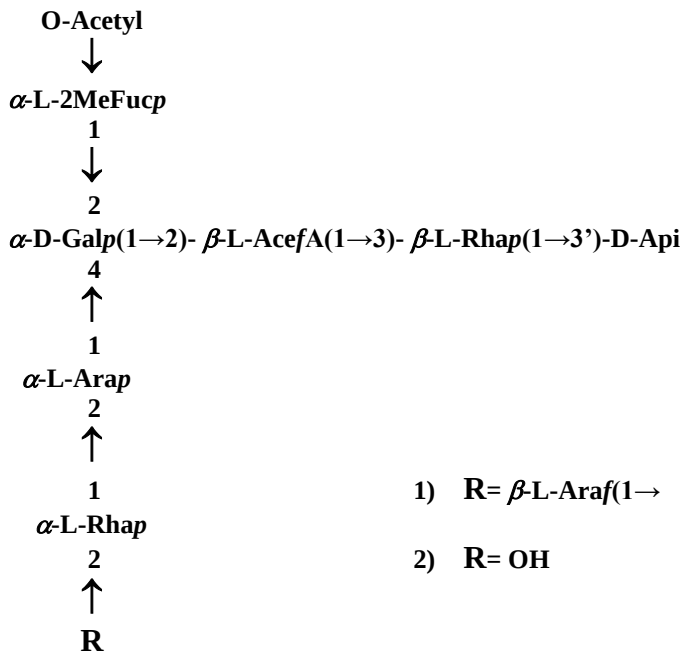


**Figure 2. 10** An octasaccharide released from sycamore cell wall rhamnogalacturonan-II (RG-II) by selective acid hydrolysis.

## 2. 4 Biomimicking Woody Tissue

### 2. 4. 1 Biomimetics of Secondary Cell Wall

"Biomimetics is a field of science that investigates biological structures and processes for their use as models for development of artificial systems. Biomimetic approaches have considerable potential in the development of new high-performance materials with low environmental impact".[65] Biological composites found in nature, like wood, bone, enamel and abalone shells, are formed through highly energy efficient, smart processes, involving moderate temperature, pressure and water as solvent. The low energy inputs and higher efficiencies are achieved by extremely precise and ordered molecular arrangement of biopolymers, leading to an efficient self-assembly process.[65] A lion share

of the current commercial composite materials are derived from petroleum based products. The dwindling petroleum resources and ever increasing emphasis on renewable resources has brought biological materials into the limelight. Self-assembly may provide a route that exploits the inherent functionality of biobased polymers to replace these petroleum based materials.

One of the most important bio-composite used in our day-to-day life is wood. As indicated in the previous section, wood is mostly composed of 'secondary cell wall', which in turn is composed of three distinct classes of compounds, namely cellulose, hemicellulose and lignin.[30] It is generally accepted that cellulose acts as the stiff reinforcing material, lignin acts as the matrix material that provides rigidity and protection, and hemicellulose acts as a compatibilizer at the interface between cellulose and lignin. Hence all components serve a general role in the function within the tree; however, the organization of the polymeric components is not well defined because of the complexity of the cell wall. In plants, it is proposed that the combination of strength and interfacial stability is achieved by coating cellulose with matrix polysaccharides that can interact with other cell wall polymers, like lignin in secondary cell walls and proteins in primary cell walls.[65]

At present, most of the industrial applications of cellulose require it to be separated from lignin and chemically modified to render it amenable to processing and meet end goals. However, these chemical modifications usually compromise the native structure and strength of cellulose.[66] It is possible to extract native components of the cell wall that resemble the constituents within the wall, either in supramolecular or polymeric form. These native components, such as the cellulose fibrils and native–like lignin, provide

model materials for the creation of simple models of organization of wood cell wall structure.

## 2. 5 Nanoscale Celluloses

### 2. 5. 1 Microfibrillated Cellulose (MFC)

In MFC, the cellulose fibers have been expanded and unravelled to form fibrils and microfibrils. MFC is obtained by mechanical fibrillation, which is a two-step process (refining and homogenization). The starting material is pulp fiber, which is passed though a refiner, where it is subject to cyclic stresses within a disk refiner. The disk refiner consists of rotor and stator disks fitted with bars and grooves against which dilute fiber suspensions are subject to cyclic stresses. In the second step, the refined dilute fiber slurries are pumped though a high pressure loaded valve assembly. The rapid opening and closing of the valves create huge pressure drops, which create shear and impact forces that lead to microfibrillation of the fibers (Figure 2. 11). Microfibrillated cellulose is characterized by very high water retention values, a high degree of chemical accessibility and the ability to form stable gels in water or other polar solvents.[67-69]

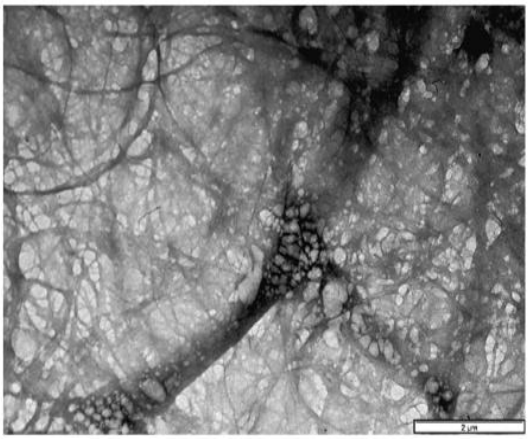

**Figure 2. 11** Transmission electron micrograph of microfibrillated cellulose (Lu, J.; Askeland, P.; Drzal, L. T., *Polymer* 2008, 49, 1285-1296, used under the fair use guidelines, 2011).

### 2. 5. 2 Cellulose Nanocrystals (CNCs)

Native cellulose microfibrils are composed of highly organized, crystalline and paracrystalline domains. The paracrystalline regions within the microfibrils are accessible to acid hydrolysis, which yields colloidal suspensions of rod-like cellulose crystallites.[70, 71] Mineral acids, especially sulfuric acid, are commonly used to produce cellulose nano-crystals. A common method involves the use of sulfuric acid (64 % w/w) at 45 °C for 45 min, after which the acid is diluted 10 fold to stop the hydrolysis reaction. The resulting solution is centrifuged to extract the nanocrystals (Figure 2. 12) followed by dialysis against water until the pH is neutral. The product is then sonicated to create particles of colloidal dimensions.[8, 72]

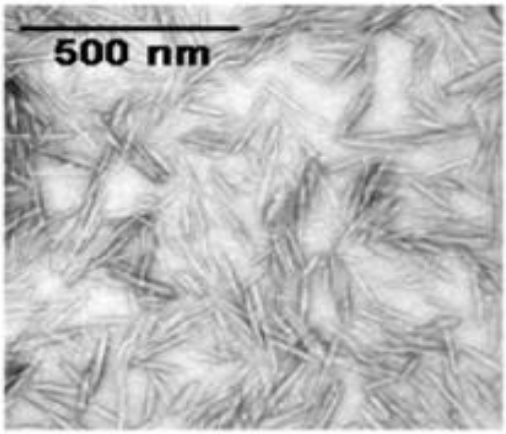


**Figure 2. 12** TEM micrograph from a suspension of CNCs obtained from cotton (Samir, M. A. S. A.; Alloin, F.; Dufresne, A., *Biomacromolecules* 2005, 6, 612-626, used under the fair use guidelines, 2011).

### 2. 5. 3 TEMPO Oxidized Nanofibrillated Cellulose (nanocellulose)

Oxidation of polysaccharides with nitrogen oxides is one of the oldest and the most common choices for obtaining polyuronic acids.[73-75] However these methods were not regioselective, hence pure polyglucuronic acids were hard to obtain.[76] A promising way

for selectively oxidizing primary alcohols is the use of the stable organic nitroxyl radical 2,2,6,6-tetramethyl-1-piperidinyloxy (TEMPO) as a mediator.[77] TEMPO has been used with NaOCl/NaBr oxidizing-regenerating system to selectively oxidize water soluble polysaccharides, where NaOCl acts as the primary oxidant, whereas TEMPO and NaBr function as the catalyst/mediator.[75] The proposed mechanism of TEMPO mediated oxidation is depicted in Figure 2. 13. The TEMPO-NaBr-NaOCl system was later used to selectively oxidize insoluble polysaccharides like cellulose and chitin.[76, 78] Extensive research on regioselective oxidation of primary hydroxyls of celluloses by TEMPO mediated oxidation has been carried out by the Isogai group.[76, 79-90]

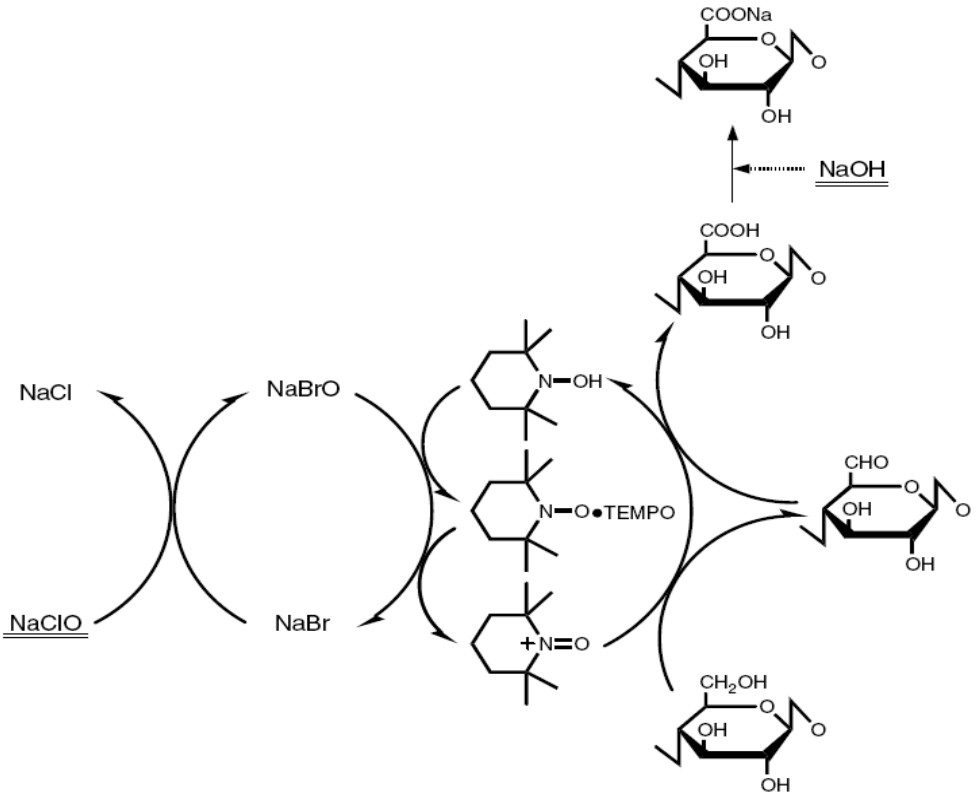


**Figure 2. 13** Proposed mechanism of TEMPO mediated oxidation of the primary hydroxyl groups of cellulose to produce celluronic acid (Saito, T.; Okita, Y.; Nge, T. T.; Sugiyama, J.; Isogai, A., *Carbohydr. Polym.* 2006, 65, 435-440, used under the fair use guidelines, 2011).

Saito, et al. found that, when carboxylate content due to the oxidation of the primary alcohols reached approximately 1.5 mmol/g, mechanical treatment of the resulting oxidized pulp/water slurries produced individualized cellulose nanofibers (Figure 2. 14).[90] To carry out the oxidation, cellulose fibers are suspended in water containing 0.1 mmol TEMPO and 1 mmol NaBr. The oxidation of the cellulose fibers is initiated by the addition of NaClO solution (1.5 - 5.0 mmol per gram of cellulose), the pH of which has been pre-adjusted to 10. The reaction is carried out at room temperature and the pH of the reaction mixture is maintained at 10 throughout the reaction by the addition of 0.5 N NaOH solution. The reaction is complete when no more NaOH is needed to stabilize the pH.[88]

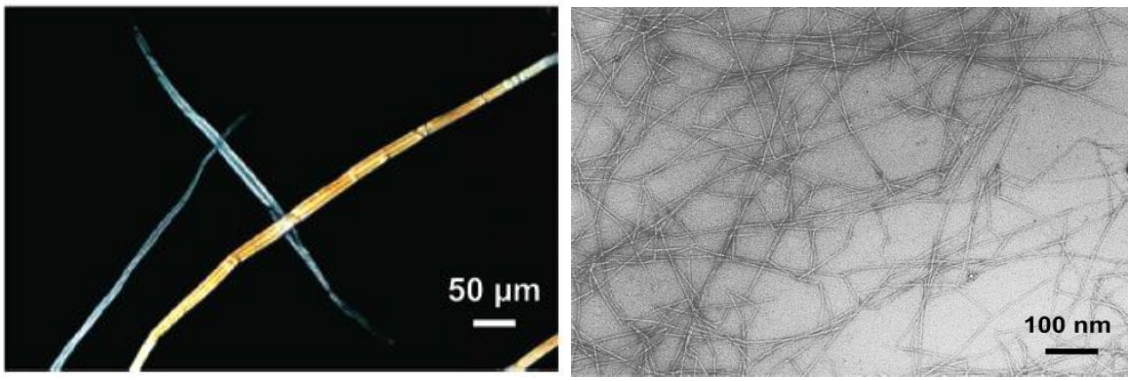


**Figure 2. 14** Polarized light micrograph of TEMPO oxidized pulp fiber (left) and TEM image of nanofibers (right) obtained from it after mechanical stirring for 10 days (Saito, T.; Kimura, S.; Nishiyama, Y.; Isogai, A., *Biomacromolecules* 2007, 8, 2485-2491, used under the fair use guidelines, 2011).

## 2. 6 Isolated Lignins

### 2. 6. 1 Technical Lignins

Technical lignins are by-products of the commercial pulping process. The first commercial pulp production was established in Sweden in 1874 utilizing the sulphite

process.[53] The by-product of the sulfite process is the lignosulfonate-lignin, which is water soluble. The sulfite process has been predominantly replaced by the sulfate process, most importantly the Kraft process, which accounts for more than 50% of all the pulping and contributes to most of the isolated lignin (Kraft lignin) in the world.[53, 91] An unconventional method of pulping is the organsolv technique, using an organic solvent.[91] The by-product of this technique is termed organosolv lignin, which is soluble in organic solvents.[92]

### 2. 6. 2 Near Native Lignins

The chemically invasive pulping processes cause drastic changes to the molecular structure, chemical functionality and molecular weight distribution of isolated lignins from their native state in wood.[92] Some of the methods developed to minimize chemical alterations to lignin through less invasive extraction processes are described below.

#### *2. 6. 2. 1 Milled Wood Lignin (MWL)*

MWL is obtained by ball milling the wood to a fine powder followed by extraction of the lignin fraction by a neutral solvent. The technique was developed by Björkman (1954),[93] wherein the finely ball-milled wood meal is extracted with an azeotropic mixture of dioxane:water (96:4 v/v %). This crude lignin preparation is further separated from the lignin-carbohydrate complex (LCC) by treating with aqueous acetic acid (acetic acid/water; 9:1 v/v) followed by precipitation in water. The precipitated lignin is filtered and dissolved in 1,2 dichloroethane/ethanol (2:1 v/v) and precipitated into ether.[94-98]

### *2. 6. 2. 2 Cellulolytic Enzyme Lignin (CEL)*

CEL is obtained by enzyme hydrolysis of ball milled/vibratory milled wood followed by extraction of the lignin fraction by a neutral solvent.[99] The finely milled wood meal is digested with a cellulase enzyme in an acetate buffer (pH 4.8 - 4.9). The process is repeated twice, after which the resulting undigested residue is freeze dried and further extracted with a mixture of dioxane:water (96:4 v/v %). The resulting CEL is purified following the procedure for MWL.[97-99]

### *2. 6. 2. 3 Enzymatic Mild Acidolysis Lignin (EMAL)*

A combined technique was developed by Wu and Argyropoulos[100] in which vibratory/ball milled wood meal was subjected to enzymatic hydrolysis followed by a mild acidolysis step. The first step removes most of the carbohydrates while the latter step cleaves the remaining lignin-carbohydrate bonds enabling the removal of lignin in high yield and purity. In detail, a 5% consistency wood meal is treated with a cellulase enzyme (40 FPU/g wood) in a 50 mM citrate buffer (pH 4.5) at 40° C for 48 hrs. The remaining insoluble material is centrifuged and washed twice with pH 2.0 deionized water and then freeze-dried. This crude lignin preparation is then subjected to extraction along with mild acidolysis in aqueous dioxane (dioxane/water 85:15, v/v containing 0.01 mol $L^{-1}$ HCl) in an inert atmosphere. The suspension is centrifuged and the supernatant is collected, neutralized with sodium bicarbonate and precipitated by drop wise addition into pH 2.0 water.[100-102]

## 2. 7 Model Studies: Cellulose-Hemicellulose Interactions

Cellulose fibers have potential as reinforcement in polymer composite material owing to the high modulus of the cellulose crystallites.[6] However, the poor miscibility and interaction of the hydrophilic cellulose in a hydrophobic matrix is highly undesirable.[8] Brummer et al.[66] have used a biomimetic approach of using a cell wall matrix polysaccharide to modify the cellulose surface rather than modifying cellulose itself to enhance cellulose matrix compatibility. For this purpose, they employed a chemo-enzymatic technique to substitute xyloglucan polymer with chemically modified xyloglucan oligosaccharides (XGO). Xyloglucan is hemicellulosic polysaccharide confined to the plant primary cell wall and is composed of $\beta(1\rightarrow4)$ linked glucan backbone substituted with xylosyl, galactosyl, and sometimes $\alpha$-fucosyl residues. The substitution of XGO's to xyloglucan polymer was carried out using the enzyme xyloglucan endotransglycosylases (XET), which aids in temporarily loosening the xyloglucan network in primary cell walls during cell growth and division. In this particular study, the XGO was substituted with amino groups, which are intrinsically more reactive than hydroxyl groups. In another study, the adsorption of xyloglucan with the aid of XET on chemical and mechanical pulps was observed.[103] They found that higher amounts of lignin and extractives on the fiber surface of thermo-mechanical and chemi-thermo-mechanical pulps lead to decreased adsorption of xyloglucan compared to the bleached Kraft pulps. In a study by Gradwell et al.,[104] the adsorption of lignin-hemicellulose complex on cellulose was modeled using pullulan abietate. Pullulan, a water-soluble polysaccharide represents the hemicellulose part, and abietic acid represents the lignin part. The model compound could be irreversibly adsorbed onto

Langmuir-Blodgett films of regenerated cellulose, as monitored by surface plasmon resonance spectroscopy. A similar study conducted with pullulan cinnamate also showed irreversible adsorption of the material onto a regenerated cellulose substrate.[105]

## 2. 8 Blends of Cellulose and Cellulose Composites

Svagan et al.[106] prepared an all polysaccharide nanocomposite by solution casting, inspired by the mechanical stiffness and strength with toughness of cell wall, even under plasticized conditions with water. To this end, the authors prepared a composite made of microfibrillated cellulose (MFC) and amylopectin starch. The amylopectin served as the matrix and was plasticized in a 50/50 mixture with glycerol to mimic the viscous nature of the matrix in the plant primary cell wall. The resulting composite showed very high toughness, and very good compatibility of the amylopectin matrix with MFC. Microscopic observations showed that the composite had a layered and nano-scale networked structure of MFC.[106] Poly(caprolactone) (PCL) and poly(L-lactic acid) (PLLA), which are biodegradable polymers, were grafted on a cellulose substrate using ring opening polymerization.[107] The idea behind this technique was to create the closest possible association between the hydrophilic cellulose fibers and the hydrophobic matrix material, which is the greatest challenge in creating cellulose based nanocomposites with hydrophobic matrix materials. The grafting experiments were carried out on unmodified cellulose (Whatman I filter paper) and cellulose pre-modified with 2,2-bis(methylol)propionic acid (bis-MPA) or xyloglucan oligosaccharide-bis-MPA (XGO-bis-MPA). The highest grafting efficiency and compatibility was found when the cellulose substrate was pretreated with bis-MPA. The resulting grafted cellulose was found to be significantly more hydrophobic in nature compared to the unmodified

substrate. The modified cellulose was also found to be very resistant to digestion by cellulases.[107]

## 2. 9 Layered Organization

### 2. 9. 1 Layer-by-Layer Build-up of Multilayers

Self-assembly has been used to build multilayered films by means of electrostatic attraction, stereo-complex formation, host-guest interactions, and hydrogen and covalent bonds.[108-112] This technique has allowed different types of materials to be assembled into thin films with a relatively precise control of architecture by adjusting process conditions such as nature and concentration of materials, pH, ionic strength, immersion time, dopant counter-ion, and number of layers. Furthermore self-assembly offers several advantages over other techniques used for thin film formation as the substrate can take any form and size, the deposition time is independent of the substrate surface area, and there are no requirements for additional equipment and/or clean rooms. Multilayer films of organic compounds on solid surfaces have been studied for more than 70 years. Such films allow fabrication of multicomposite molecular assemblies of tailored architecture. Langmuir-Blodgett (LB) and chemisorption techniques can be used with limited classes of molecules. Another approach is the fabrication of multilayers by consecutive adsorption of polyanions and polycations. In the past the molecularly controlled fabrication of nano-scale films were dominated by the LB-technique, in which monolayers are formed on water surface and transferred to a solid substrate.[113, 114] Pioneering work on synthetic nano-scale heterogeneous structures of organic molecules were carried out by Kuhn and coworkers using the LB-technique.[115] However, the LB-technique requires special instrumentation and is limited by substrate size, topology, film quality and stability. It is

desirable to have a simple system that would yield nano-architecture with tight control over positioning of layers that would also be independent of nature, size and topology of the substrate. Electrostatic attraction is a very good candidate to drive the layer build-up process, because it is the least sterically constrained of all the bond types. This simple process allows for charge reversal of a substrate, which can lead to repulsion of equally charged molecules, thus self-regulating and restricting adsorption of oppositely charged molecules on top of the first layer to a single added layer (Figure 2. 15).[116]

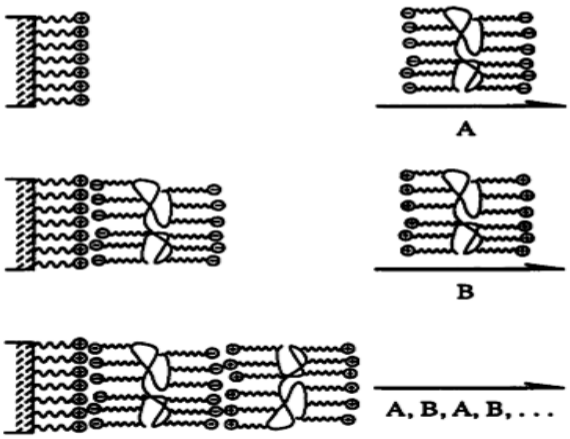


**Figure 2. 15** Schematic of the sequential deposition of polyelectrolytes in LbL assembly of multilayers (Decher, G.; Hong, J. D.; Schmitt, J., *Thin Solid Films* 1992, 210, 831-835, used under the fair use guidelines, 2011).

Polymer molecules can assume different conformations depending on factors such as pH, backbone rigidity, concentration, and polymer-solvent interaction.[112] At low pH values, polycations assume an extended or rod-like conformation as a consequence of the electrostatic repulsion forces between doped sites within the same polymer backbone, whereas at higher pH, they can assume a coiled conformation as a result of lesser electrostatic repulsive forces. When a polymer adsorbs on a surface of opposite charge sites, it may neutralize the charges on the surface or even overcompensate for them. The

number of charged sites on a molecule which can interact with oppositely charged layer is dependent on pH and chain flexibility. The driving forces for deposition are entropy of counterion release and a balance of attractive forces, specifically between the charged molecules and the oppositely charged substrate, repulsive forces between polymer chains of the same charge, and the pH dependent chain conformation and flexibility. Rather than a linear trend of increasing thickness with pH, there is a small range of pH in which the thickness reaches the maximum value. This happens when the surface charge density experienced by an adsorbing, fully charged polyelectrolyte falls below the critical value needed to overcome entropic chain coiling effects.[111]

LbL multilayers of alternating polystyrene sulfonate as polyanion and poly-4-vinylbenzene-(N,N-diethyl-N-methyl-)-ammonium iodide as polycation were obtained on single silicon crystals. A linear build-up of alternate layers up to 39 layers, measuring 43.5 nm was monitored and up to 100 layers were deposited.[117] X-ray and scattering studies of the LbL assembled polyelectrolyte films showed that they were composed of individual molecular layers. The length scale of the interdigitation of the polyelectrolyte chains was found to be ~ 12 Å. The initial layers that formed closer to the substrate were lower in thickness compared to the equilibrium thickness far from the substrate.[118, 119] The interdigitation/interpenetration causes the layers to have a “fuzzy”, yet layered structure. There is no communication between the polyelectrolyte deposited at the $i^{th}$ step and the polyelectrolytes deposited at the $i+p^{th}$ step, where p is typically larger than 2 to 3. However, p is largely dependent on the nature of the polyelectrolytes. The thickness of a single layer is known to vary between 1 and 10 nm depending on various parameters such

as ionic strength, pH, and to an extent, the molecular weight of the polyelectrolyte.[120-123] Mederios and Mattosso[112] were able to build multilayers of poly(o-ethoxyaniline) (POEA) and cellulose nano-fibrils on a glass substrate by the LbL deposition process. They found that by alternate layering of POEA and cellulose nano-fibrils at pH 2, a four-fold increase in the amount of material deposited was noted as opposed to multiple dipping in POEA. Ding et al.[124] were able to deposit multilayers of polyelectrolytes on electrospun cellulose acetate nanofibers. The oppositely charged polyelectrolytes in their study were poly(allylamine hydrochloride) (PAH; cationic polymer) and poly(acrylic acid) (PAA; anionic polymer). They found that the pH of the solution had a significant impact on the thickness of the film.

### 2. 9. 2 Layer-by-Layer Assembly with Cellulosics

LbL multilayers of cationic polymer poly(diallyldimethylammonium chloride) (PDDA) and negatively charged CNCs obtained by sulfuric acid hydrolysis were prepared by Podsiadlo et al.[125] The multilayers were deposited on piranha etched (3:1 $H_2SO_4$:$H_2O_2$) glass substrate. UV absorption studies at 360 nm showed a linear build-up as a function of the bilayer number, and a uniform distribution of the CNCs in the multilayer build-up. A high optical density value of 0.35 was reached after just 10 bilayers which points to high cellulose nanocrystal loading. Ellipsometry studies showed that each bilayer was approximately 11 nm thick.[125] Morphological and optical characterization were carried out on multilayers formed by LbL deposition of cationic poly(allylamine hydrochloride) (PAH) and CNCs prepared by sulfuric acid hydrolysis technique.[72] Two deposition techniques were used to create the mutilayers on silicon wafers, a) spin coating and b) solution dipping. Both techniques yielded multilayer build-up and showed similar surface

morphologies and roughness, but differed markedly in film thickness. Complete coverage of the substrate surface was noted with the first bilayer with the spin-coating technique, whereas it took 2.5 bilayers with solution dipping to achieve the same. Although both techniques yielded smooth films (RMS roughness less than 10 nm), the spin coated films were smoother, showing a constant roughness value with increasing layer build-up. The solution dipping technique showed a slight but linear increase in roughness with layer build-up. The relative smoothness of the spin-coated films was attributed to the increased surface coverage and the downward force exerted on the substrate as a result of the rapid expulsion of liquid in the spinning process. Moreover, a radial alignment of the nanocrystals was observed with spin-coating due to the viscous shear on the cellulose nanocrystal suspension as it flows outwards during the spinning process. This order was detected by polarized light microscopy due to the birefringence of the nanocrystals.[72] LbL build-up of multilayers with cationic PAH and CNCs were carried out in a magnetic field, in an attempt to orient the CNCs along the magnetic field, by virtue of their diamagnetic anisotropy.[126] To apply the magnetic field, the substrate was introduced into a chiral nematic suspension of cellulose nanocrystal within a 7 T magnetic field of an NMR spectrometer. No specific orientation was found after 30 min of deposition of the substrate in the chiral nematic suspension within the magnetic field. However, after a 24 hr deposition time, AFM study revealed a substantial degree of orientation. The long time required for the orientation of the nanocrystals have been hypothesized to be a result of the time dependence to overcome the twist elastic energy barrier to orientation.[126] The structural details of LbL multilayer build-up of CNCs and PAH were studied by Bruno, et al. using neutron reflectivity and AFM.[127] They confirmed the earlier results that smooth

films were formed with high loading of CNCs. Furthermore they found evidence of the existence of the cellulose component as a double layer. They concluded that the layer build up was entropy driven and the smooth and linear build-up of layers was due to the flexibility of PAH.[127] LbL assembled films of PEI and cellulose nanowires obtained from marine animal tunicates were shown to have very strong antireflective properties.[128] The cellulose nanowires from marine tunicin were extracted following a detailed purification step followed by sulfuric acid hydrolysis. The cellulose nanowires were shown to assemble in a highly porous architecture resembling a "flattened matchstick pile", which was attributed to the strong anti-reflective property.[128] Multilayer build-up of carboxymethylated-MFC was studied with three different cationic polyelectrolytes: polyethyleneimine (PEI), PDDA and PAH.[129] The multilayering was carried out either by solution dipping or by spraying. Of the three polyelectrolytes used, PEI was shown to adsorb the largest amount of carboxymethylated-MFC, followed by PDDA and PAH. Addition of an electrolyte (NaCl) increased the MFC adsorption up to a certain concentration, after which the adsorption decreased. This study points out the fact that adsorption and conformation of polyelectrolytes have a significant impact on multilayer build-up. Multilayer films of PEI and MFC exhibited different interference colors with each bilayer indicating a smooth and well-defined increase in thickness.[129] Multilayer build-up of PEI and carboxymethylated-MFC was studied as a function of electrolyte and polyelectrolyte/colloid concentration, and the pH of the solutions.[130] The layer build-up was monitored using two techniques, dual-polarization interferometry (DPI) and quartz crystal microbalance with dissipation (QCM-D). It was noted that an increase in the electrolyte concentration and pH of PEI solutions led to an increase in the adsorption of

MFC. In contrast, an increase of electrolyte concentration and pH of the MFC solution decreased its adsorption onto PEI. The combination of DPI and QCM-D data showed that the water content of hydrated films composed of 5 bi-layers of PEI and MFC was ca. 41%. The high water content was attributed to the entrapment of water in the porous structure of MFC within the multilayers and also due to the hydration of the heavily carboxymethylated microfibrils.[130] Thin films were prepared by layer-by-layer assembly of CNCs and xyloglucan aided by the strong non-electrostatic interactions.[131] The layers were deposited on a primer layer of PEI/$(PSS/PAH)_n$ so as to reduce the impact of the silicon substrate on cellulose nanocrystal – xyloglucan layer build-up. Neutron reflectivity and AFM data showed that a well-ordered film was formed with repeat units assembled to give a well-defined architecture. This architecture was shown to be different from those of cellulose nanocrystal/polycation multilayers.

### 2. 9. 3 Layer-by-Layer Nanocomposites

LbL deposition processes have been utilized to prepare a wide range of composite materials. Polymer/single walled carbon nanotubes (SWNT) composites of nanometer scale homogeneity prepared by LbL assembly were shown to have a tensile strength in the range of hard ceramics. A SWNT loading of up to 50% was obtained and the problem of phase separation between the polymer matrix and SWNT was overcome with this technique.[132] An artificial analog of the biocomposite nacre was prepared by the LbL deposition of poly(diallyldimethylammonium chloride) (PDDA) and montmorillonite (MTM) clay.[133] The strength and toughness of nacre, which is attributed to the brick and mortar type of arrangement of the organic and inorganic phase, was mimicked using the LbL process. The resulting composite films had a tensile strength of 100 ± 10 MPa,

similar to nacre, and an ultimate Young's modulus of 11 ± 2 GPa, similar to that of lamellar bones.[133] Following the same methodology, when PDDA was replaced with polyvinyl alcohol (PVA) the resulting composite showed a tensile strength of 150 ± 40 MPa and modulus of 13 ± 2 GPa.[134] Simultaneous to the build-up, crosslinking of the composite films led to further increase in mechanical properties.[134, 135] For instance, when crosslinking was carried out with gluteraldehyde, the tensile strength and modulus increased to 400 ± 40 MPa and 106 ± 11 MPa respectively.[134] When crosslinking was carried out with metal ions, the tensile stresses and moduli increased to 250 ± 50 MPa and 42 ± 5 GPa, and 320 ± 40 MPa and 58 ± 6 GPa for $Al^{3+}$ and $Cu^{2+}$, respectively.[135]

## 2. 10 Thin Film Characterization

### 2. 10. 1 Quartz Crystal Microbalance

A quartz crystal microbalance (QCM) is composed of a thin disc of quartz crystal, placed between two electrodes which supply an AC voltage across the disc. The applied alternating current induces vibrational motion of the crystal, by virtue of its piezoelectric property at its resonant frequency.[136]

#### *2. 10. 1. 1 Concept of Piezoelectricity*

The piezoelectric phenomenon was first observed by Pierre and Jacques Curie in 1880.[137] Piezoelectricity is observed in materials that crystallize in non-centrosymmetric space groups, or in other words, in crystals that lack a center of symmetry.[136] Non-centrosymmetric crystals possess a polar axis due to the dipoles arising from the distribution of the atoms in the crystal lattice. When a stress is applied in an appropriate direction, the displacement of the atoms in the non-centrosymmetric crystal lattice leads

to a change in the net dipole moment, producing a net charge on the faces of the crystal (Figure 2. 16).[136] If electrodes are placed on the opposite ends of such materials, and an external current sensing unit is attached, a current is detected to flow on applying an external stress. Conversely, when an alternating voltage is applied, mechanical oscillations can be induced within the crystal lattice.[138]

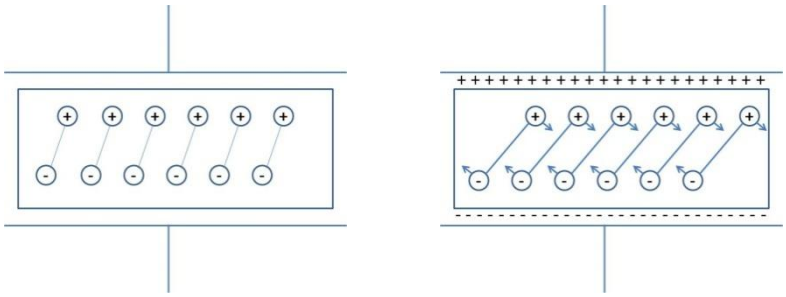

**Figure 2. 16** Schematic representing the shear deformation caused in a quartz crystal due the lattice strain caused by reorientation of dipoles, when an external electric field is applied (Buttry, D. A.; Ward, M. D., *Chem. Rev.* 1992, 92, 1355-1379, used under the fair use guidelines, 2011).

### *2. 10. 1. 2 Fundamentals of QCM*

Commercially used quartz crystals are manufactured from plates cut from single quartz crystals at specific angles to the primary optical axis of the crystal (Figure 2. 17-a). The earliest oscillators were prepared by making y-z plane cuts, and applied voltage in the x direction. In the early stages, frequency was thickness controlled and this resulted in a major drawback due to interferences from overtones and harmonics. This problem was overcome with Y cut crystals, which vibrate in the shear mode. However, the Y cut crystals were sensitive to temperature variations. The temperature coefficients and frequency constants of the crystals were found to be dependent on the angle of rotation. Two particular cut angles, +35° 15′ (AT; Figures. 2. 17-b, 2. 17-d) and - 49° 00′(BT; Figure 2. 17-c) were found to have a temperature coefficient of zero.[138]

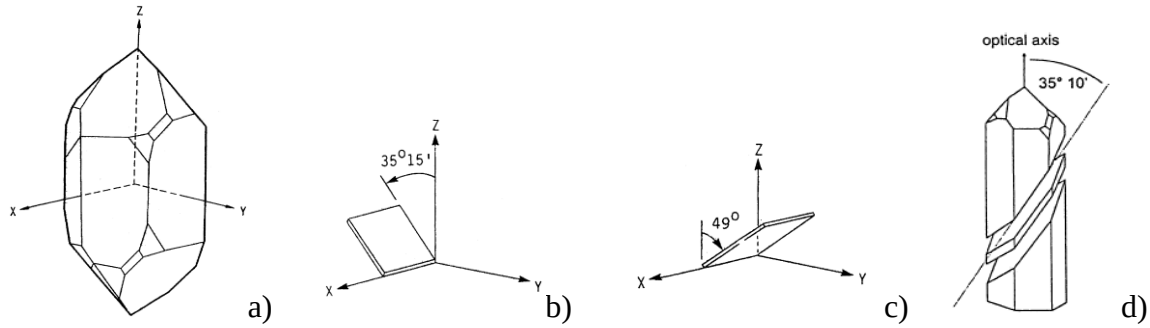


**Figure 2. 17** a) Assignment of axis to an uncut quartz crystal b) AT cut quartz crystals c) BT cut quartz crystals (O'Sullivan, C. K.; Guilbault, G. G., *Biosens. Bioelectron.* 1999, 14, 663-670, used under the fair use guidelines, 2011), and d) orientation of AT cut crystal with respect to the optical axis of an uncut quartz crystal (Chang, P. S.; Robyt, J. F., *J. Carbohydr. Chem.* 1996, 15, 819-830, used under the fair use guidelines, 2011).

If a voltage is applied across the quartz crystal through electrodes attached on the opposite faces, the piezoelectric nature coupled with the crystalline orientation of quartz generates a shear deformation within the crystal. For a given excitation frequency of the applied AC voltage, provided the thickness of the crystal is an odd multiple of half the wavelength of the acoustic wave generated, the crystal can be electrically excited to resonance. Such excitation frequencies cause shear deformations within the crystals generating standing waves in the fundamental and odd numbered harmonic frequency resonances (Figure 2. 18).[141]


**Figure 2. 18** Shear displacement profiles across the quartz crystal thickness for the fundamental and third overtone (Martin, S. J.; Granstaff, V. E.; Frye, G. C., Anal. Chem. 1991, 63, 2272-228, used under the fair use guidelines, 2011).

The frequency of the acoustic waves in resonance state is given by eqn. 2. 1.

$$f_o = \frac{v_{tr}}{2t_q} = \left(\mu_q^{1/2}/\rho_q^{1/2}\right) 2t_q \quad \text{---------- eqn. 2. 1}$$

where $v_{tr}$ is the transverse velocity of sound in AT cut quartz (3.34 x $10^4$ $ms^{-1}$), $t_q$ is the thickness of the quartz crystal, $\mu_q$ is the shear modulus, and $\rho_q$ the density of the quartz crystal. When a uniform layer of material is deposited/adsorbed on the quartz surface, the acoustic wave will travel across the interface and propagate into the material. Assuming a rigid layer, where the acoustic properties of the deposited material are essentially identical to that of the quartz, the whole system can be considered a "composite resonator". This implies that the change in thickness due to the foreign material can be considered as the change in the total thickness of the quartz. With this assumption, a fractional change in the thickness ($\Delta t$) of the quartz will cause a directly proportional fractional change in frequency ($\Delta f$; eqn. 2. 2).

$$\frac{\Delta f}{f_o} = -\frac{\Delta t}{t_q} = -2f_o \Delta t / v_{tr} \quad \text{-------- eqn. 2. 2}$$

Appropriate substitutions in eqns. 1 and 2 will lead to the commonly used Sauerbrey relationship (eqn. 2. 3).

$$\Delta f = -2f_o^2 \Delta m / A\left(\mu_q \rho_q\right)^{1/2} \quad \text{---------- eqn. 2. 3}$$

However, this relation assumes the crystal to be vibrating in air, and an elastic response of the adsorbed mass on the substrate. A modification over the Sauerbrey eqn. for crystals vibrating in a liquid medium was given by Kanazawa and Gordon (eqn. 2. 4):[142]

$$\Delta f = \frac{\sqrt{f_o \rho_l \eta_{lm}}}{\rho_q t_q \sqrt{2\pi}} \sin\left[\frac{\pi}{4} - \frac{\phi_l}{2}\right] \quad \text{-------- eqn. 2. 4}$$

where $\rho_l$, $\eta_{lm}$ and $\phi_l$ are the density, magnitude of complex viscosity and relative phase angle of the liquid medium. The complex viscosity is given by $\eta^* = \eta' - i\eta'' = \eta_m e^{-i\phi}$, where $\eta'$ describes energy dissipation and $\eta''$ describes energy storage.

Apart from the frequency data QCM can also provide information regarding the dissipation (D) of the adsorbed material, which is the reciprocal of the Q-factor, given by:

$$D = \frac{1}{Q} = \frac{E_{dissipated}}{2\pi E_{stored}} \quad \text{------- eqn. 2. 5}$$

where $E_{dissipated}$ is the energy dissipated during one period of oscillation and $E_{stored}$ is the energy stored in the oscillating system.[143]

QCM and QCM-D (QCM with dissipation monitoring) techniques have been extensively utilized to study the formation of thin layers[144, 145] and the build-up of LbL multilayers.[130, 146, 147] Aulin et al.[130] studied the layer-by-layer build-up of alternating layers of polyethyleneimine and MFC using QCM-D and were able to calculate the mass of adsorbed material at each step. Garg et al.[147] have also used the QCM-D technique to study the adsorption kinetics of the LbL build-up of poly(allylamine hydrochloride) and poly[1-[*p*-(3′-carboxy-4′-hydroxyphenylazo)benzene-sulfonamido]-1,2-ethandiyl].

### 2. 10. 2 Atomic Force Microscopy

Atomic force microscope (AFM) systems have a micromachined cantilever probe with a sharp tip (~5 to 20 nm radius) coupled with a photodetector (Figure 2. 19). A laser beam is reflected off the end of the cantilever to the photodetector, which precisely measures the deflection of the cantilever.[148] In AFM, the tip interacts with the surface to be probed through a number of possible interactions, like van der Waals, electric, magnetic, short range, capillary or other electromagnetic forces.[149]

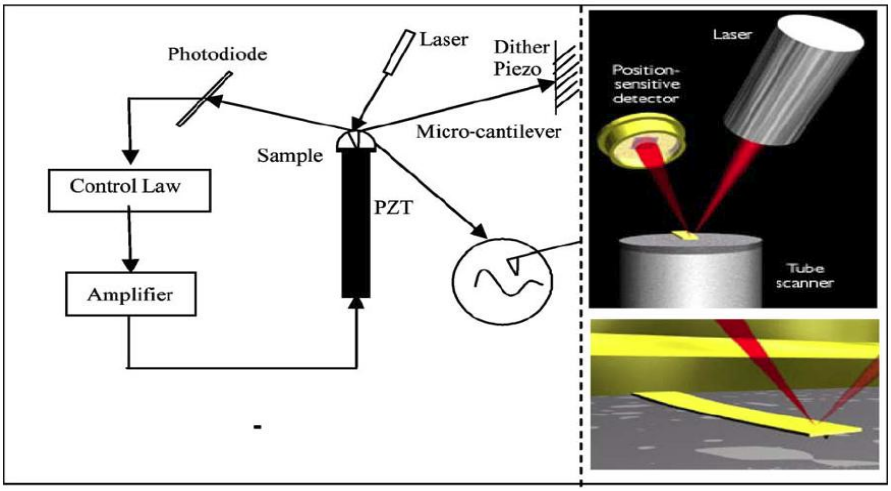


**Figure 2. 19** Schematic of basic laser detection AFM operation technique (Jalili, N.; Laxminarayana, K., *Mechatronics* 2004, 14, 907-945, used under the fair use guidelines, 2011).

The AFM functions by scanning the tip over the sample surface using feedback signals. This allows the piezoelectric scanner to maintain the tip at a constant height or force above the sample. The feedback mechanism is achieved by measuring the difference in intensity of the laser light on the photodetectors.[148] The photodetector is composed of a two or four quadrant detector. A vertical deflection of the cantilever produced through the interaction of the tip and the surface causes the laser beam to be reflected higher or lower on the detector (Figure 2. 20). The difference in the amount of current produced between the top and bottom of the photodetector is proportional to the vertical motion of the cantilever.[149] The difference in photo-signal enables the AFM to maintain a constant height or force above the sample. In constant force mode, the piezoelectric transducer monitors the tip to sample distance, whereas in the constant height mode, the deflection of the cantilever is measured.[148]

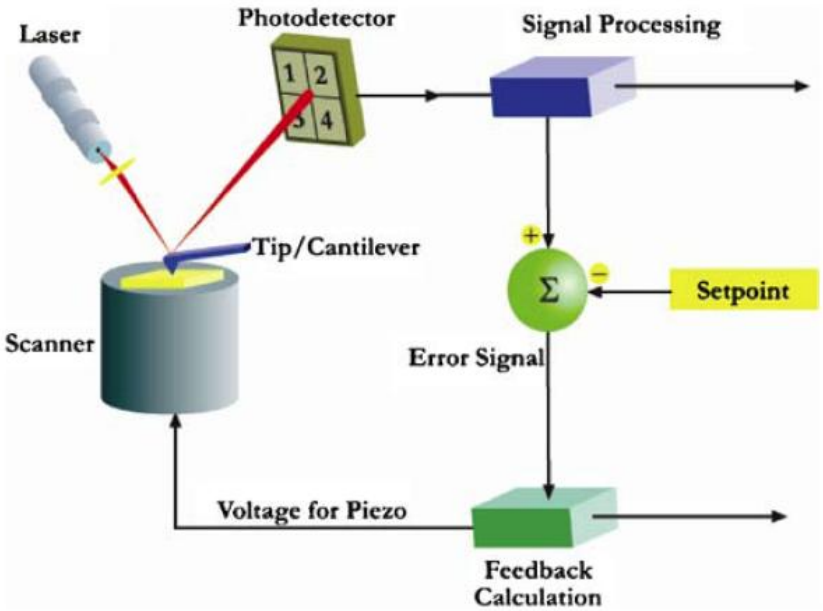


**Figure 2. 20** Laser detection and photodetector feedback mechanism in AFM (Zavala, G., *Colloid. Polym. Sci.* 2008, 286, 85-95, used under the fair use guidelines, 2011).

There are three basic operational modes in AFM: a) contact, b) non-contact, and c) tapping mode (Figure 2. 21). The contact mode acquires information on the attributes of the sample surface by measuring the interaction forces while the tip is in contact with sample at all times. The non-contact mode functions by keeping the tip slightly away from the sample surface while oscillating the cantilever at or near its natural resonant frequency. This technique helps probe the electric, magnetic, and/or atomic forces of the sample. The tapping mode can be described as a hybrid of the contact and non-contact modes. In tapping mode the cantilever is allowed to vibrate at or near its resonant frequency while[125] gleaning the sample surface and touching the sample for a very minimal amount of time.[148]

AFM is a very effective surface probing technique and has been widely used for imaging the layer build-up process in LbL multilayer studies.[72, 125-128, 130] The AFM technique,

complemented with SEM has been used to demonstrate dense coverage of cellulose nanowires on PEI in the LbL adsorption process.[128] Similar AFM results were seen when CNCs were adsorbed in LbL fashion with polycations, showing dense, homogenous, and uniform coverage.[127] The effect of a strong magnetic field on LbL deposited CNCs was studied using AFM.[126] The random vs. specific directional orientation in the presence of the magnetic field was clearly demonstrated using this technique.

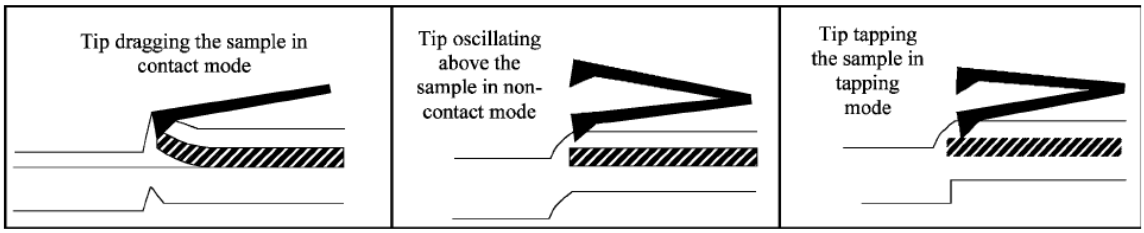


**Figure 2. 21** Schematic of the three different AFM operational modes: a) contact, b) non-contact, and c) Tapping mode (Zavala, G., *Colloid. Polym. Sci.* 2008, 286, 85-95, used under the fair use guidelines, 2011).

## 2. 11 References


1. Dietz, A. G. H., *Composite Materials. 1965 Edgar Marburg Lecture*. American Society for Testing and Materials: Philadelphia, 1965.

2. Åström, B. T., *Manufacturing of Polymer Composites*. Chapman & Hall: London, 1997.

3. Berthelot, J.-M., *Composite Materials*. Springer-Verlag: New York, 1999.

4. Capadona, J. R.; Van Den Berg, O.; Capadona, L. A.; Schroeter, M.; Rowan, S. J.; Tyler, D. J.; Weder, C., *Nat. Nanotechnol.* **2007,** 2, 765-769.

5. Cerruti, P.; Ambrogi, V.; Postiglione, A.; Rychlý, J.; Matisová-Rychlá, L.; Carfagna, C., *Biomacromolecules* **2008,** 9, 3004-3013.

6. Rusli, R.; Eichhorn, S. J., *Appl. Phys. Lett.* **2008,** 93, 033111-3.

7. Dufresne, A., *Can. J. Chem.* **2008,** 86, 484-494.

8. Samir, M. A. S. A.; Alloin, F.; Dufresne, A., *Biomacromolecules* **2005,** 6, 612-626.

9. Cao, X.; Dong, H.; Li, C. M., *Biomacromolecules* **2007,** 8, 899-904.

10. Favier, V.; Canova, G. R.; Cavaillé, J. Y.; Chanzy, H.; Dufresne, A.; Gauthier, C., *Polym. Adv. Technol.* **1995,** 6, 351-355.

11. Favier, V.; Chanzy, H.; Cavaillé, J. Y., *Macromolecules* **1995,** 28, 6365-6367.

12. Helbert, W.; Cavaillé, J. Y.; Dufresne, A., *Polym. Compos.* **1996,** 17, 604-611.

13. Chazeau, L.; Cavaillé, J. Y.; Canova, G.; Dendievel, R.; Boutherin, B., *J. Appl. Polym. Sci.* **1999,** 71, 1797-1808.

14. Ruiz, M. M.; Cavaillé, J. Y.; Dufresne, A.; Graillat, C.; Gérard, J.-F., *Macromolecular Symposia* **2001,** 169, 211-222.

15. Dubief, D.; Samain, E.; Dufresne, A., *Macromolecules* **1999,** 32, 5765-5771.

16. Dufresne, A.; Kellerhals, M. B.; Witholt, B., *Macromolecules* **1999,** 32, 7396-7401.

17. Angles, M. N.; Dufresne, A., *Macromolecules* **2000,** 33, 8344-8353.

18. Noishiki, Y.; Nishiyama, Y.; Wada, M.; Kuga, S.; Magoshi, J., *J. Appl. Polym. Sci.* **2002,** 86, 3425-3429.

19. Grunert, M.; Winter, W. T., *J. Polym. Environ.* **2002,** 10, 27-30.

20. Science, N. A. o., *Heirarchical structures in biology as a guide for new materials technology*. National Academy Press: Washington DC, 1994.

21. Campbell, N. A., *Biology*. The Benjamin/Cummings Publishing Company: Redwood City, 1993.

22. Baer, E.; Hiltner, A., *Phys. Today* **1992,** 45, 60-67.

23. Rho, J.-Y.; Kuhn-Spearing, L.; Zioupos, P., *Med. Eng. Phys.* **1998,** 20, 92-102.

24. Weiner, S.; Traub, W., *Federation of American Societies for Experimental Biology Journal* **1992,** 6, 879-885.

25. Viney, C., *Mat. Sci. Eng. R.* **1993,** 10, 187-236.

26. Bowyer, J. L.; Shmulsky, R.; Haygreen, J. G., *Forest Products and Wood Science*. Iowa State Press: Iowa, 2003.

27. Savidge, R. A., *IAWA Journal* **1996,** 17, 269-310.

28. Savidge, R. A., *Can. J. Botany* **1989,** 67, 2663–2668.

29. Donaldson, L. A., *Phytochemistry* **2001,** 839–873.

30. Fengel, D.; Wegener, G., *Wood-Chemistry, Ultrastructure, Reactions*. Walter de Gruyter: New York, 1989.

31. Samuels, A. L.; Rensing, K. H.; Douglas, C. J.; Mansfield, S. D.; Dharmawardhana, D. P.; Ellis, B. E., *Planta* **2001,** 216, 72-82.

32. Kerr, T.; Bailey, I. W., *Journal of Arnold Arboretum* **1934,** 15, 327-349.

33. Brändström, J. Morphology of norway spruce tracheids with emphasis on wall Organisation. Swedish University of Agricultural Science, Uppsala, 2001.

34. Fengel, D.; Stoll, M., *Holzforschung* **1973,** 27, 1-7.

35. Barrett, J. D.; Scniewind, A. P.; Taylor, R. L., *Wood Sci.* **1972,** 4, 178-192.

36. Page, D. H.; El Hosseiny, F.; Winkler, K.; Bain, R., *Pulp Paper Mag. Can.* **1972,** 73, 72-77.

37. Bergander, A., Salmen, L., *Holzforschung* **2000,** 54, 654-660.

38. Meier, H.; Wilkie, K. C. B., *Holzforschung* **1959,** 13, 177-180.

39. Meier, H., General chemistry of cell walls and distribution of the chemical constituents across the walls. In *The formation of wood in forest trees*, Zimmermann, M. H., Ed. Academic press: New York, London, 1964.

40. Raven, P. H.; Evert, R. F.; Eichorn, S. E., *The Biology of Plants*. 6th ed.; W.H. Freeman Worth Publishers: New York, 1999.

41. O'Neill, M. A.; York, W. S., The composition and structure of primary cell walls. In *The Plant Cell Wall: Annual Plant Reviews*, Rose, J. K. C., Ed. 2003; Vol. 8, pp 1-54

42. Roberts, K., *Curr. Opin. Cell Biol.* **1989,** 1, 1020-1027.

43. Wyatt, S. E.; Carpita, N. C., *Trends Cell Biol.* **1993,** 3, 413-417.

44. Carpita, N. C.; Gibeaut, D. M., *Plant J.* **1993,** 3, 1-30.

45. Carpita, N. C., *Annu. Rev. Plant Physiol. Plant Mol. Biol.* **1996,** 47, 445-471.

46. Brown Jr., R. M., *J. Polym. Sci., Part A: Polym. Chem.* **2004,** 42, 487-495.

47. Saxena, I. M.; Brown Jr, R. M., *Annals of Botany* **2005,** 96, 9-21.

48. Jarvis, M., *Nature* **2003,** 426, 611-612.

49. Attala, R. H.; VanderHart, D. L., *Science* **1984,** 223, 283-285.

50. Nishiyama, Y.; Sugiyama, J.; Chanzy, H.; Langan, P., *J. Am. Chem. Soc.* **2003,** 125, 14300–14306.

51. Kuga, S.; Takagi, S.; Brown Jr, R. M., *Polymer* **1993,** 34, 3293-3297.

52. Mueller, S. C.; Brown Jr, R. M., *J. Cell Biol.* **1980,** 84, 315–326.

53. Sjöstrom, E., *Wood chemistry: fundamentals and applications 2nd ed.* Academic Press: London, 1993.

54. Zhang, J. G. Biochemical Study and Structural Applications of Fungal Pectinases. . Universitatis Upsaliensis, Uppsala, 2006.

55. Lau, J. M.; McNeil, M.; Darvill, A. G.; Albersheim, P., *Carbohydr. Res.* **1985,** 137, 111-125.

56. Willats, W. G. T.; McCartney, L.; Mackie, W.; Knox, J. P., *Plant Mol. Biol.* **2001,** 47, 9-27.

57. McNeil, M.; Darvill, A. G.; Albersheim, P., *Plant Physiol.* **1982,** 70, 1586-1591.

58. Ishii, T.; Thomas, J.; Darvill, A.; Albersheim, P., *Plant Physiol.* **1989,** 89, 421-428.

59. Lau, J. M.; McNeil, M.; Darvill, A. G.; Albersheim, P., *Carbohydr. Res.* **1987,** 168, 245-274.

60. Stevenson, T. T.; Darvill, A. G.; Albersheim, P., *Carbohydr. Res.* **1988,** 182, 207-226.

61. Whitcombe, A. J.; O'Neill, M. A.; Steffan, W.; Albersheim, P.; Darvill, A. G., *Carbohydr. Res.* **1995,** 271, 15-29.

62. Buchanan, B.; Gruissem, W.; Jones, R., *Biochemistry and molecular biology of plants*. American Society of Plant Biologists: Rockville, 2000.

63. Reis, D.; Vian, B., *C. R. Biol.* **2004,** 327, 785-790.

64. Saka, S.; Goring, D. A. I., Localisation of of lignins in wood cell walls. In *Biosynthesis and biodegradation of wood components*, Higuchi, T., Ed. Academic Press: Orlando, 1985; pp 51-62.

65. Teeri, T. T.; Brumer III, H.; Daniel, G.; Gatenholm, P., *Trends Biotechnol.* **2007,** 25, 299-306.

66. Brummer III, H.; Zhou, Q.; Baumann, J. M.; Carlsson, K.; Teeri, T. T., *J. Am. Chem. Soc.* **2004,** 126, 5715-5721

67. Herrick, F. W.; Casebier, R. L.; Hamilton, J. K.; Sandberg, K. R., *J. Poly. Sc.* **1983,** 37, 797-813.

68. Turbak, A. F.; Snyder, F. W.; Sandberg, K. R., *J. Poly. Sc.* **1983,** 37, 815-27.

69. Lu, J.; Askeland, P.; Drzal, L. T., *Polymer* **2008,** 49, 1285-1296.

70. Ranby, B. G., *Discuss. Faraday Soc.* **1951,** 11, 158-64.

71. Battista, O. A.; Coppick, S.; Howsmon, J. A.; Morehead, F. F.; Sisson, W. A., *Ind. Eng. Chem.* **1956,** 48, 333-335.

72. Cranston, E. D.; Gray, D. G., *Biomacromolecules* **2006,** 7, 2522-2530.

73. Maurer, K.; Drefahl, G., *Ber. Dtsch. Chem. Ges.* **1942,** 75, 1489-1491.

74. Yackel, E. C.; Kenyon, W. O., *Journal of the American Chemical Society* **1942,** 64, 121-127.

75. de Nooy, A. E. J.; Besemer, A. C.; van Bekkum, H., *Carbohydr. Res.* **1995,** 269, 89-98.

76. Isogai, A.; Kato, Y., *Cellulose* **1998,** 5, 153-164.

77. Semmelhack, M. F.; Chou, C. S.; Cortes, D. A., *J. Am. Chem. Soc.* **1983,** 105, 4492-4494.

78. Chang, P. S.; Robyt, J. F., *J. Carbohydr. Chem.* **1996,** 15, 819-830.

79. Kato, Y.; Habu, N.; Yamaguchi, J.; Kobayashi, Y.; Shibata, I.; Isogai, A.; Samejima, M., *Cellulose* **2002,** 9, 75-81.

80. Shibata, I.; Isogai, A., *Cellulose* **2003,** 10, 151-158.

81. Shibata, I.; Isogai, A., *Cellulose* **2003,** 10, 335-341.

82. Saito, T.; Isogai, A., *Biomacromolecules* **2004,** 5, 1983-1989.

83. Saito, T.; Isogai, A., *Carbohydr. Polym.* **2005,** 61, 183-190.

84. Saito, T.; Shibata, I.; Isogai, A.; Suguri, N.; Sumikawa, N., *Carbohydr. Polym.* **2005,** 61, 414-419.

85. Saito, T.; Yanagisawa, M.; Isogai, A., *Cellulose* **2005,** 12, 305-315.

86. Saito, T.; Isogai, A., *Colloids Surf. Physicochem. Eng. Aspects* **2006,** 289, 219-225.

87. Saito, T.; Okita, Y.; Nge, T. T.; Sugiyama, J.; Isogai, A., *Carbohydr. Polym.* **2006,** 65, 435-440.

88. Saito, T.; Nishiyama, Y.; Putaux, J.-L.; Vignon, M.; Isogai, A., *Biomacromolecules* **2006,** 7, 1687-1691.

89. Saito, T.; Isogai, A., *Ind. Eng. Chem. Res.* **2007,** 46, 773-780.

90. Saito, T.; Kimura, S.; Nishiyama, Y.; Isogai, A., *Biomacromolecules* **2007,** 8, 2485-2491.

91. Fengel, D.; Wegener, G., *Wood: Chemistry, Ultrastructure, Reactions*. Walter de Gruyter: Berlin, New York, 1984.

92. Liu, Y.; Carriero, S.; Pye, K.; Argyropolos, D. S., A comparison of the structural changes occuring in lignin during alcell and kraft pulping in hardwoods and softwoods. In *Lignin: Historical, Biological and Materials Perspectives (ACS Symposium Series 742)*, Glasser, W. G., Northey, R. A. and Schultz, T. P., Ed. American Chemical Society: Washington, DC, 1999; pp 447-464.

93. Bjorkman, A., *Nature* **1954,** 174, 1057-1058.

94. Björkman, A., *Sven. Papperstidn.* **1956,** 59, 477-485.

95. Björkman, A., *Sven. Papperstidn.* **1957,** 60, 243.

96. Björkman, A., *Ind. Eng. Chem. Res.* **1957,** 49, 1395-1398.

97. Hu, Z.; Yeh, T.-F.; Chang, H.-m.; Matsumoto, Y.; Kadla, J. F., *Holzforschung* **2006,** 60, 389-397.

98. Ikeda, T.; Holtman, K.; Kadla, J. F.; Chang, H.-m.; Jameel, H., *J. Agric. Food. Chem.* **2002,** 50, 129-135.

99. Chang, H. M.; Cowling, E. B.; Brown, W.; Adler, E.; Miksche, G., *Holzforschung* **1975,** 29, 153-159.

100. Wu, S.; Argyropoulos, D., *J. Pulp Pap. Sci.* **2003,** 29, 235-240.

101. Guerra, A.; Filpponen, I.; Lucia, L. A.; Saquing, C.; Baumberger, S.; Argyropoulos, D. S., *J. Agric. Food. Chem.* **2006,** 54, 5939-5947.

102. Guerra, A.; Filpponen, I.; Lucia, L. A.; Argyropoulos, D. S., *J. Agric. Food. Chem.* **2006,** 54, 9696-9705.

103. Zhou, Q.; Baumann, J. M.; Brumer, H.; Teeri, T. T., *Carbohydr. Polym.* **2006,** 63, 449-458.

104. Gradwell, S. E.; Renneckar, S.; Esker, A. R.; Heinze, T.; Gatenholm, P.; Vaca-Garcia, C.; Glasser, W., *C. R. Biol.* **2004,** 327, 945-953.

105. Kaya, A.; Du, X.; Liu, Z.; Lu, J. W.; Morris, J. R.; Glasser, W. G.; Heinze, T.; Esker, A. R., *Biomacromolecules* **2009**.

106. Svagan, A. J.; Samir, A. S. A.; Berglund, L. A., *Biomacromolecules* **2007,** 8, 2556-2563.

107. Lönberg, H.; Zhou, Q.; Brummer III, H.; Teeri, T. T.; Malmström, E.; Hult, A., *Biomacromolecules* **2006,** 7, 2178-2185.

108. Decher, G.; Maclennan, J.; Reibel, J.; Sohling, U., *Adv. Mater.* **1991,** 3, 617-619.

109. Decher, G.; Schmitt, J., *Prog. Coll. Pol. Sci. S.* **1992,** 89, 160-164-340.

110. Decher, G.; Hong, J. D.; Schmitt, J., *Thin Solid Films* **1992,** 210, 831-835.

111. Decher, G., Polyelectrolyte multilayers, an overview. In *Multilayer Thin Films*, Decher, G., Sclenoff, G. B., Ed. Wiley-VCH: Weinheim, 2003; pp 1-46.

112. Medeiros, E. S.; Mattoso, L. H. C.; Bernardes-Filho, R.; Wood, D. F.; Orts, W. J., *Colloid. Polym. Sci.* **2008,** 286, 1265-1272.

113. Blodgett, K. B., *J. Am. Chem. Soc.* **1935,** 57, 1007-22.

114. Blodgett, K. B.; Langmuir, I., *Phys. Rev.* **1937,** 51, 964-82.

115. Kuhn, H.; Mobius, D., *Angew. Chem. Int. Ed. Engl.* **1971,** 10, 620-637.

116. Decher, G., *Science* **1997,** 277, 1232.

117. Decher, G.; Maclennan, J.; Sohling, U.; Reibel, J., *Thin Solid Films* **1992,** 210, 504-507.

118. Schmitt, J.; Gruenewald, T.; Decher, G.; Pershan, P. S.; Kjaer, K.; Loesche, M., *Macromolecules* **1993,** 26, 7058-7063.

119. Lvov, Y.; Decher, G.; Moehwald, H., *Langmuir* **1993,** 9, 481-486.

120. Lösche, M.; Schmitt, J.; Decher, G.; Bouwman, W. G.; Kjaer, K., *Macromolecules* **1998,** 31, 8893-8906.

121. Ladam, G.; Gergely, C.; Senger, B.; Decher, G.; Voegel, J.-C.; Schaaf, P.; Cuisinier, F. J. G., *Biomacromolecules* **2000,** 1, 674-687.

122. Schlenoff, J. B.; Ly, H.; Li, M., *J. Am. Chem. Soc.* **1998,** 120, 7626-7634.

123. Hübsch, E.; Fleith, G.; Fatisson, J.; Labbé; P.; Voegel, J. C.; Schaaf, P.; Ball, V., *Langmuir* **2005,** 21, 3664-3669.

124. Ding, B.; Fujimoto, K.; Shiratori, S., *Thin Solid Films* **2005,** 491, 23-28.

125. Podsiadlo, P.; Choi, S.-Y.; Shim, B.; Lee, J.; Cuddihy, M.; Kotov, N. A., *Biomacromolecules* **2005,** 6, 2914-2918.

126. Cranston, E. D.; Gray, D. G., *Sci. Technol. Adv. Mat.* **2006,** 7, 319-321.

127. Jean, B.; Dubreuil, F.; Heux, L.; Cousin, F., *Langmuir* **2008,** 24, 3452-3458.

128. Podsiadlo, P.; Sui, L.; Elkasabi, Y.; Burgardt, P.; Lee, J.; Miryala, A.; Kusumaatmaja, W.; Carman, M. R.; Shtein, M.; Kieffer, J.; Lahann, J.; Kotov, N. A., *Langmuir* **2007,** 23, 7901-7906.

129. Wågberg, L.; Decher, G.; Norgren, M.; Lindstrom, T.; Ankerfors, M.; Axnas, K., *Langmuir* **2008,** 24, 784-795.

130. Aulin, C.; Varga, I.; Claesson, P. M.; Wagberg, L.; Lindstrom, T., *Langmuir* **2008,** 24, 2509-2518.

131. Jean, B.; Heux, L.; Dubreuil, F. d. r.; Chambat, G. r.; Cousin, F., *Langmuir* **2008,** 25, 3920-3923.

132. Mamedov, A. A.; Kotov, N. A.; Prato, M.; Guldi, D. M.; Wicksted, J. P.; Hirsch, A., *Nat Mater* **2002,** 1, 257-257.

133. Tang, Z.; Kotov, N. A.; Magonov, S.; Ozturk, B., *Nat Mater* **2003,** 2, 413-418.

134. Podsiadlo, P.; Kaushik, A. K.; Arruda, E. M.; Waas, A. M.; Shim, B. S.; Xu, J.; Nandivada, H.; Pumplin, B. G.; Lahann, J.; Ramamoorthy, A.; Kotov, N. A., *Science* **2007,** 318, 80-83.

135. Podsiadlo, P.; Kaushik, A. K.; Shim, B. S.; Agarwal, A.; Tang, Z.; Waas, A. M.; Arruda, E. M.; Kotov, N. A., *J. Phys. Chem. B* **2008,** 112, 14359-14363.

136. Buttry, D. A.; Ward, M. D., *Chem. Rev.* **1992,** 92, 1355-1379.

137. Curie, P.; Curie, J., *C. R. Acad. Sci* **1880,** 91, 294.

138. Alder, J. F.; McCallum, J. J., *The Analyst* **1983,** 108, 1169-1189.

139. O'Sullivan, C. K.; Guilbault, G. G., *Biosens. Bioelectron.* **1999,** 14, 663-670.

140. Janshoff, A.; Galla, H.-J.; Steinem, C., *Angew. Chem.* **2000,** 39, 4004-4032.

141. Martin, S. J.; Granstaff, V. E.; Frye, G. C., *Anal. Chem.* **1991,** 63, 2272-2281.

142. Kanazawa, K. K.; Gordon, J. G., *Anal. Chim. Acta* **1985,** 175, 99-105.

143. Rodahl, M.; Hook, F.; Krozer, A.; Brzezinski, P.; Kasemo, B., *Rev. Sci. Instrum.* **1995,** 66, 3924-3930.

144. Norgren, M.; Gärdlund, L.; Notley, S. M.; Htun, M.; Wågberg, L., *Langmuir* **2007,** 23, 3737-3743.

145. Pillai, K. V.; Renneckar, S., *Biomacromolecules* **2009,** 10, 798-804.

146. Richert, L.; Lavalle, P.; Payan, E.; Shu, X. Z.; Prestwich, G. D.; Stoltz, J.-F.; Schaaf, P.; Voegel, J.-C.; Picart, C., *Langmuir* **2004,** 20, 448-458.

147. Garg, A.; Heflin, J. R.; Gibson, H. W.; Davis, R. M., *Langmuir* **2008,** 24, 10887-10894.

148. Jalili, N.; Laxminarayana, K., *Mechatronics* **2004,** 14, 907-945.

149. Zavala, G., *Colloid. Polym. Sci.* **2008,** 286, 85-95.

# Chapter 3. Materials

## 3 .1 Cationic polymer: Poly(diallyldimethylammonium chloride) (PDDA)

PDDA used in this study was obtained from Sigma Aldrich Inc. Molecular weight distribution analyzed in 0.5 M NaCl solution had an $M_n$ of $7.2\times10^4$ and $M_w$ of $2.4\times10^5$ $g.mol^{-1}$ (PDI =3.4) based on size exclusion chromatography (SEC) measurements (Figure 3. 1).

a)

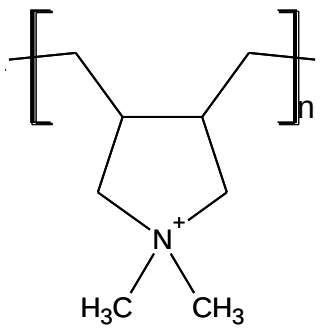


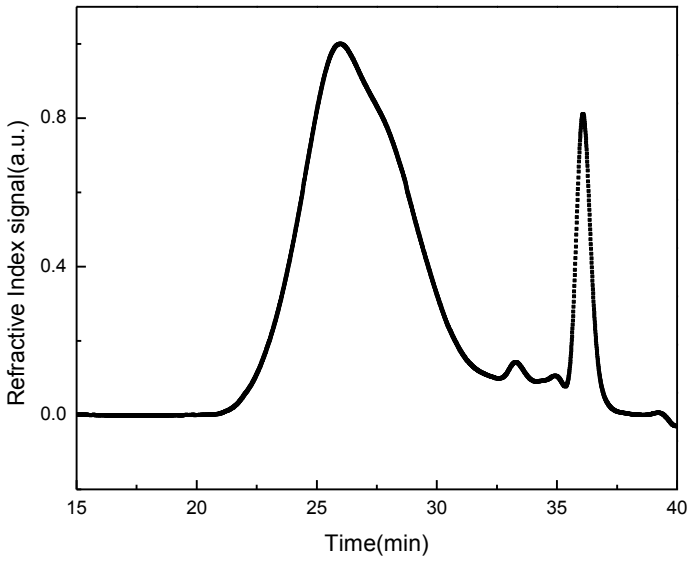


b)

**Figure 3. 1** Structure (a) and refractive index chromatogram versus retention time (b) for PDDA sample used in the study.

## 3. 2 Alkali Lignin

Alkali lignin used in this study was kraft lignin obtained from Sigma-Aldrich Inc. with a molecular weight dispersion of $M_n$ = 1700 and $M_w$ = 14,200 g.mol$^{-1}$ (PDI = 5.4).

## 3. 3 Oraganosolv Lignin

Organosolv Lignin (OL) used in this study was obtained from Sigma Aldrich Inc. GPC analysis of acetylated OL in chloroform gave a molecular weight distribution of Mn = 1300 and Mw = 3800 g.mol$^{-1}$ (PDI = 2.9) (Figure 3. 2).

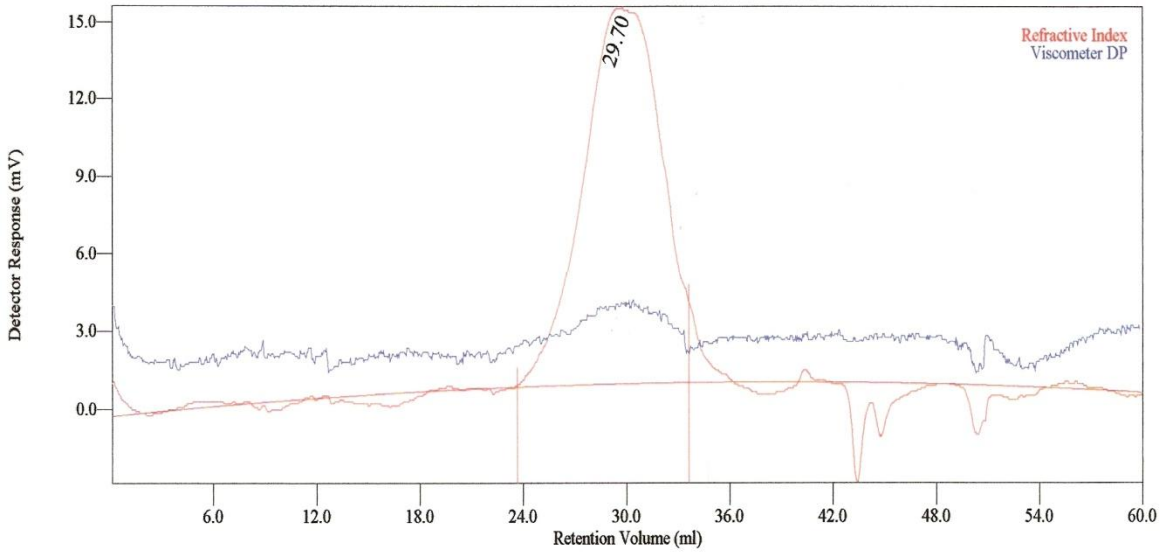


**Figure 3. 2** Refractive index and viscometer versus retention volume chromatogram of OL

## 3. 4 Organosolv 2 Hydroxyethyl Ether Lignin

Hydroxyethyl ether lignin used in this study was obtained from Sigma-Aldrich Inc. with a molecular weight dispersion of $M_n$ = 1600 and $M_w$ = 5500 g.mol$^{-1}$ (PDI = 3.4). The lignin derivative is devoid of nearly all phenolic groups.

## 3. 5 Organosolv Propionate Lignin

Propionate lignin used in this study was obtained from Sigma-Aldrich Inc. with a molecular weight dispersion of $M_n$ = 2000 and $M_w$ = 5000 g.mol$^{-1}$ (PDI = 3.1). There is almost equal amounts of aromatic and aliphatic propionate groups in this lignin derivative.

## 3. 6 Hardwood Milled Wood Lignin

Hardwood milled wood lignin (HMWL) used in this study was extracted from red oak. GPC analysis of acetylated HMWL in chloroform gave a molecular weight distribution of Mn = 5300, Mw = 31,900 g.mol$^{-1}$ (PDI = 6.0) (Figure 3. 3).

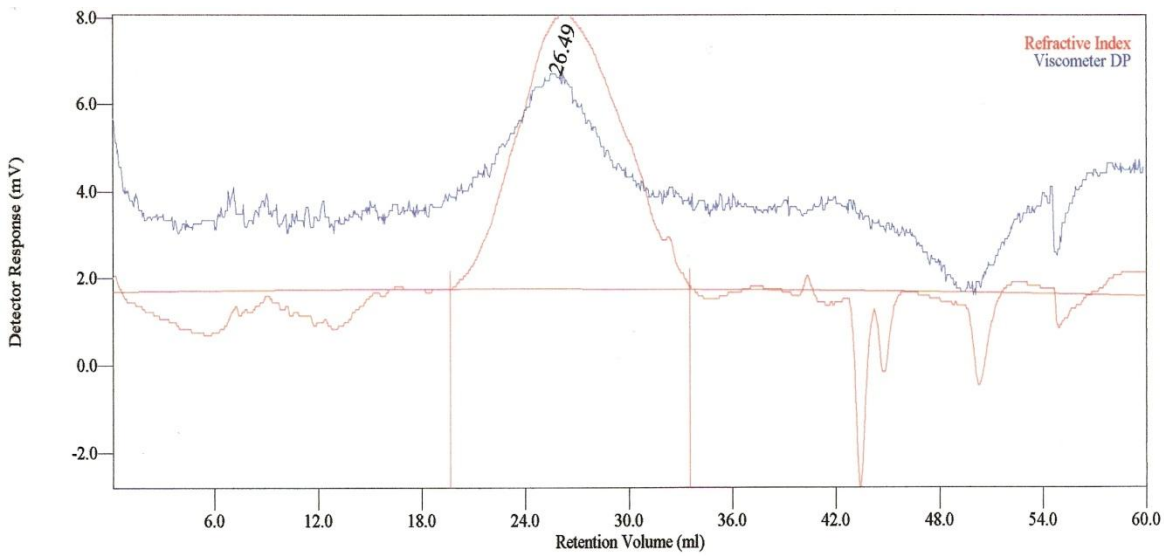


**Figure 3. 3** Refractive index and viscometer versus retention volume chromatogram of HMWL

## 3. 7 Nanocellulose

The steps for preparing nanocellulose (NC) from never dried pulp used in this studies as follows. Never dried pulp (20 g, 1% w/v, dry weight basis), graciously supplied by Weyerhaeuser Inc., was mixed with TEMPO (0.313 g, 0.1 mmol) and NaBr (2.0 g, 1 mmol) in a 3 L three-neck flask until the fibers were well dispersed in 2.0 L of water (Milli-Q, 18.5 MΩ.cm). The oxidation was initiated by slowly adding a 12% solution of NaOCl (64.7 ml, 5 mmol/g of cellulose) to the reaction mixture, while maintaining the pH of the mixture at 10 by adding 0.5 M NaOH. The reaction was stopped when no further addition of NaOH was required to maintain the pH. The oxidized fibers were thoroughly washed with Milli-Q water to remove the reagents and stored at 4 °C for further use. The carboxyl content of the oxidized pulp was determined by conductometric titration. A 3 % (w/v, dry weight basis) slurry of the TEMPO oxidized pulp was beaten in a Warring blender until the slurry became viscous and the blades started spinning in

air. The blended slurry was diluted to 0.1% (w/v) and nanofibrillated by ultrasonication with a Sonics® (Model GE 505) ultrasonic processor for 15 min. The ultrasonicated samples were centrifuged at 5000 rpm for 5 min and the transparent supernatant containing the fibrillated nanocellulose (Figure 3. 4) fraction was decanted, freeze-dried and stored for further use.

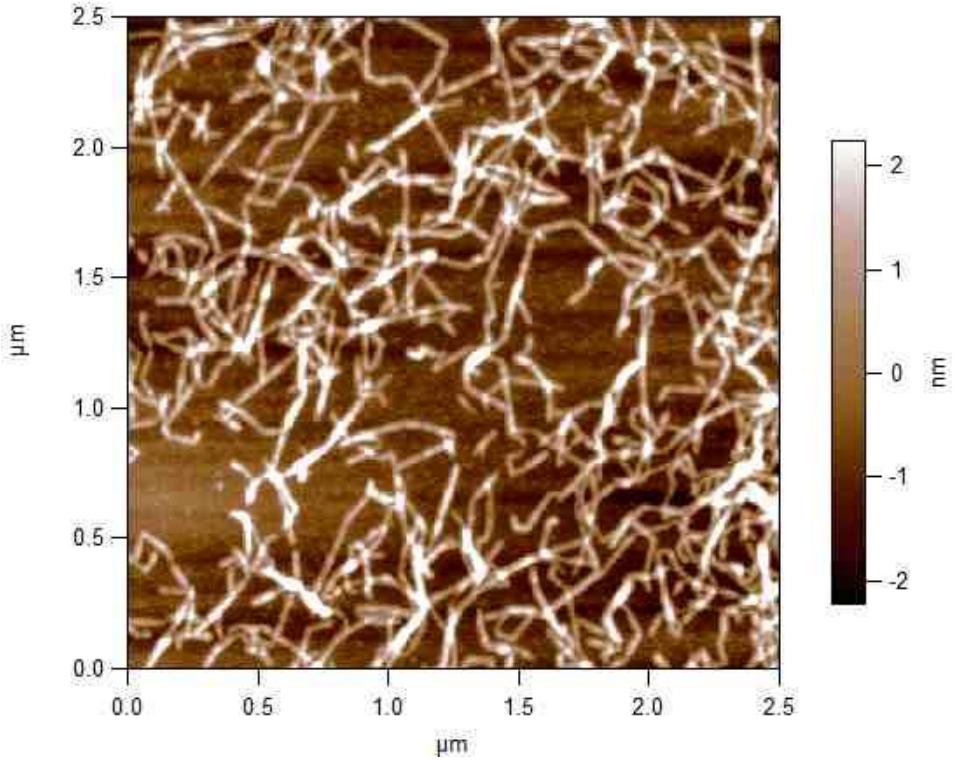


**Figure 3. 4** AFM height image of NC deposited on freshly cleaved mica surface.

# Chapter 4. Cation-$\pi$ Interactions as a Mechanism in Technical Lignin Adsorption to Cationic Surfaces

Paper published originally in Biomacromolecules under the following reference:
**Karthik V. Pillai and Scott Renneckar, *Biomacromolecules* 2009, 10, 798-804.**
Reprinted with permission, 2009, American Chemical Society.

## 4. 1 Abstract

The assembly of dissolved technical lignins in aqueous and organic medium has been studied at the solid-liquid interface. Adsorption of alkali lignin onto gold coated crystals treated with a cationic polymer was determined using a quartz crystal microbalance with dissipation monitoring. Complete coverage of the cationic surface with alkali lignin occurred at low solution concentration, revealing a high affinity coefficient under both alkali and neutral conditions. With additional adsorption studies from organosolv lignin in organic solvent and spectroscopic analysis of mixtures of cationic polymer and alkali lignin, a noncovalent interaction between lignin's aromatic rings and the cation of the quaternary ammonium group was shown to exist. The work underscores how polyphenolic biopolymers can strongly interact with cations through noncovalent interactions to control molecular architecture.

## 4. 2 Introduction

One-tenth to one-third of lignocellulosic biomass is composed of lignin[1-3] that can be isolated in high yield during the conversion process.[4] As a co product from a biorefinery, isolated lignin possesses significant potential for value addition without degrading to monomeric products or incinerating for cogeneration of electricity.[5,6] Currently,

lignosulfonates are the most widely utilized isolated lignin product, used as dispersants and binders in aqueous systems.[7] Other technologies have emerged for isolated lignin based on its natural functions as a high modulus and heat resistance polymer; facile chemical modification routes were created to convert isolated lignin into heat moldable engineering plastics.[8] Based on the current body of knowledge, value added applications of isolated lignin arise from its ability to serve as a surface active agent (self-assembling) or as mechanical reinforcement (structure enhancing). In trees, which can grow to be the largest organisms on the planet, lignin has been the polymer that has enabled vertical ascent of plants. Lignification occurs at cell wall maturation when the polysaccharide and protein structures are present, limiting the structures that lignin can adopt. Lignification occurs in an aqueous solution environment and it has been suggested that the pathway of polymerization and organization are dictated by noncovalent interactions between monomers[9] and dirigent proteins.[10] Utilization of isolated lignin has exploited these noncovalent interactions by aging solutions in aqueous conditions to alter its molecular weight profile and resulting mechanical performance of lignin thermoplastics.[11] Lignin isolated from industrial processes is soluble in aqueous solutions of elevated pH because of the ionization of the phenolic hydroxyl groups. A number of models for the colloidal behavior of isolated lignin macromolecules have been refined demonstrating the aggregation behavior in varying solution conditions.[12-16] The balance of electrostatic repulsion and van der Waals attraction (Derjaguin-Landau-Verwey-Overbeektheory) predicts the solution behavior of isolated lignin.[15] Ionization of phenolic hydroxyls (and hence electrostatic repulsion) is influenced by pH[12,15] and temperature,[17,18] which controls its hydrodynamic radius and aggregation.[19] After isolated lignin is dissolved in alkali

solutions, the pH can be lowered to neutrality without precipitating the lignins; however, the associative nature of lignins is pH sensitive.[19-22] Light scattering measurements revealed association occurs for kraft lignin below pH 11.5,[22] while diffusion coefficients from pulse field gradient NMR indicate association is evident when the pH is below 9.0.[19] The difference in association is attributed to a hysteresis in the protonation of the phenol, dependent upon if the lignin is first dissolved in strong alkali or if the pH is increased during dissolution.[19] Association of isolated lignin in solution is suggested to occur through $\pi$-$\pi$ interactions of lignin's aromatic units[23]. Argyropoulos and co-workers found that the association behavior of enzymatic mild acidolysis lignin (EMAL), highly representative of the overall lignin present in the wood cell wall, is time sensitive and reversible.[24,25] A marked species effect was determined with softwoods having a greater propensity to associate and dissociate. Furthermore, intermolecular $\pi$-$\pi$ interactions were interrupted by introduction of molecular iodine, which decreased the apparent molecular weight and dramatically increased the rate of disassociation of EMAL.[24] Strong attraction has been recorded between model lignin macromolecules probed by modified AFM tips[26] while $\pi$-$\pi$ interactions have been exploited in the separation of lignin-carbohydrate complexes by hydrophobic-interaction chromatography.[27] In addition to $\pi$-$\pi$ interactions, isolated lignin is known to adsorb onto cationic surfaces, presumably through ion-ion interactions in the partially ionized state. Isolated lignin adsorption at solid surfaces was studied with cellulose, pretreated cellulose, and mica surfaces along with a graphite surface.[28-30] Lignin does not remain irreversibly adsorbed on the cellulose fiber surfaces after washing with water.[28] However, pretreating the surface with a cationic polymer does cause irreversible adsorption. Atomic force microscopy measurements of adsorbed lignin

on pretreated cationic polymer surfaces revealed spherical or disk-like clusters with thicknesses between 2-4 nm.[29] These studies were performed with alkali lignin near neutral pH, where the carboxylic acid fraction would be disassociated providing a small charge density[31] for ion-ion interactions. In other fields, recent studies have pointed to cation-$\pi$ interactions to be a powerful intermolecular force for noncovalent interactions in biological structures.[32,33] These cation-$\pi$ noncovalent interactions are predictable by electrostatic potential maps of the aromatic moieties,[34] however, these interactions operate over van der Waals distances (instead of typical ion-dipole distances) that prohibit modeling as a simple ion-quadrupole interaction. The interaction is directional where the ion binds on the planar face. Moreover, while the degree of polarizability cannot be used to predict interactions, this mechanism has been suggested to play a role with molecules that have large effective radii, such as ammonium ions.[34] Furthermore, these interactions are of the strongest noncovalent interactions, indicated by computational studies where the quaternary ammonium ion binds to phenol at 40 kJ/mol.[35] The unique nature of the interaction is highlighted where typically hydrophobic receptors can immobilize water soluble ions; cations can have greater interaction energy with benzene than with water, as revealed by the ability of solvated quaternary ammonium ions to preferentially bind benzene[36]. Based on isolated lignin's structure of ionizable phenolic and carbonyl groups, aliphatic hydroxyls, methoxy groups, combined with the aromatic backbones, there are a number of modes for interactions that have been documented and may be relevant for organizing lignin at solid-liquid interfaces. Further understanding of these modes may lead to the creation of novel biobased products by exploiting both the structure-forming and mechanical-enhancing abilities of lignin. The

present work deals with the elucidation of cation- $\pi$ interaction mechanism as the major driving force behind technical lignin adsorption to cationic surfaces. It is expected that understanding such intermolecular interactions will be a critical step in the design and formulation of highly structured films.

## 4. 3 Experimental Section

### 4. 3. 1 Materials

The technical lignins used in this study were alkali lignin (Sigma Aldrich, *M*n 1750), organosolv lignin (Sigma Aldrich, *M*n 800), organosolv 2 hydroxyethyl ether lignin (Sigma Aldrich, *M*n 1600), and organosolv propionate lignin (Sigma Aldrich, *M*n 2000). The cationic polymer used in this study was poly(diallyldimethylammonium chloride) (Sigma Aldrich; *M*w 200000-350000). Alkali lignins were dissolved in aqueous alkali (0.05% w/v; 0.1 N NaOH) with ultra pure water (Milli-Q Direct3 UV) to make stock solutions. The 0.05% (w/v) stock solutions were diluted to 0.0125% (w/v) with ultrapure water followed by the addition of HCl (1 N and 0.1 N) to adjust the pH to 10.5, 9.0, and 7.0, respectively. Separately, ultrapure water was then adjusted to 7, 9, and 10.5 using 0.1 N NaOH. The pH adjusted ultrapure water (termed as buffer in this study) was used to make dilutions of the pH adjusted lignin stock solutions (0.25-10 mg/L) and PDDA (5000 mg/L). For studies in organic solvent, organosolv lignin and its derivatives were dissolved in 95% ethanol (0.001% w/v)) with mild heating below the reflux temperature.

### 4. 3. 2 Quartz Crystal Microbalance

Quartz crystal microbalance with dissipation monitoring (QCM-D; E4 system, Q-Sense Inc.) was used to monitor the adsorption process. QCM-D measures the fundamental frequency of 5 MHz and monitors odd numbered overtones/harmonics from 3 to 13. Gold-coated piezoelectric quartz crystals were used for all the experiments. The crystals were cleaned in a base piranha solution (3 parts concentrated NH4OH to 1 part H2O2 at 60 °C) for 10 min. The temperature in the flow cells were maintained at 25 ( 2 °C and a flow rate of 0.30 mL/min was used in all experiments. Real time monitoring and data analysis were done with Q-Soft and Q-Tools software, respectively (Q-Sense, Inc.). The mass or thickness (conversion with effective density) of the adsorbed layer could be determined using the Sauerbrey equation,[37] provided a rigid layer is formed

$$\Delta f_m = -\frac{2\times f_0^2\times\Delta m}{A\times\sqrt{\rho_q\mu_q}} \tag{4. 1}$$

where $\Delta f_m$ = change in frequency, $f_0$ = fundamental frequency, $\Delta m$= change in mass, $A$ = piezo-electrically active area, $\rho_q$ = density of quartz (2.648 g/cm$^2$), and $\mu_q$ = shear modulus of quartz (2.947 × 10-11 dynes/cm$^2$). Though all the overtones were in good agreement, the ninth overtone showed the optimal signal-to-noise ratio and, hence, was used for all Sauerbrey calculations. QCM-D also gives the dissipation information (no units), given by the relation

$$D = \frac{1}{\pi f \tau} \tag{4. 2}$$

where $D$ = dissipation, $f$= frequency, and $\tau$ = decay time. The Q-tools software was used for the viscoelastic modeling of the layers using either a Voigt or Maxwell representation

of the film.[38] For all viscoelastic modeling the seventh and ninth overtones were used to fit the data.

### 4. 3. 3 Experiments with Alkali Lignin

A typical adsorption experiment involved introducing the buffer into the cell and waiting for a stable baseline (five minutes). After that point, the pump was stopped and the solution switched to polymer solution (PDDA or lignin), where adsorption was monitored in real time until equilibrium was reached, typically less than 20 min. The solutions were switched back to buffer and desorption was monitored. All experiments followed this protocol of introducing into the flow cell the buffer (baseline), polymer solution (adsorption), and reintroduction of buffer (rinse) to compare the baseline before and after adsorption to separate out influences of viscosity changes and reversible adsorption from the irreversibly adsorbed material. Alkali lignin adsorption on PDDA treated surfaces were carried out in series: the PDDA layer was formed in situ by introducing PDDA solution (5000 mg/L) followed by introduction of lignin solutions in the order of increasing concentrations (0.25-10 mg/L; note that buffer was used between each adsorption step). Change in frequency was always recorded as the difference between the frequency of the baseline and the frequency after the polymer layer (PDDA or lignin) was rinsed with buffer. Frequency changes were converted to mass and then fit to the Langmuir equation[39] using a nonlinear curve fitting program (OriginV. 8) to determine surface excess

$$\Gamma = \frac{n_s bC}{1+bC} \tag{4. 3}$$

where $\Gamma$ is the amount of material adsorbed per area, $n_s$ is the saturation value of the surface, $b$ is the Langmuir affinity coefficient, and $C$ is the concentration. Studies were done in triplicate with new solutions made for the repetitions.

### 4. 3. 4 Experiments with Organosolv Lignin and its Derivatives

Adsorption experiments of organosolv lignin and its derivatives dissolved in 95% ethanol were carried out on PDDA or bare gold. For adsorption experiments carried out on PDDA surface, the PDDA layer was formed in situ on the gold surface by introducing an aqueous PDDA solution (5000 mg/L; pH 7 buffer). Once the PDDA layer was deposited, the lignin layers were deposited in the same manner as followed for alkali lignin, except that the buffer was replaced by 95% ethanol for establishing the baseline and rinse steps.

### 4. 3. 5 Fourier Transform Infrared Spectroscopy (FTIR)

KBr pellets of alkali lignin, PDDA and alkali lignin-PDDA complex were prepared (150 mg KBr: 1-2 mg sample) with pressure. The FTIR spectra were collected in transmission mode with a Thermo-Electron Nicolet 8700 spectrometer. The spectra were recorded in duplicate at a resolution of 2 $cm^{-1}$ and 32 scans were taken per spectra.

## 4.4 Results

With the quartz crystal microbalance, PDDA adsorption to gold coated quartz crystals was monitored as a function of time (Figure 4. 1). As PDDA is introduced into the cell, there is an immediate decrease in frequency, which is a combination of a change in fluid viscosity, reversibly adsorbed PDDA, and irreversibly adsorbed PDDA. After a plateau is reached, the buffer solution is reintroduced causing the frequency to shift. There is a spike in the frequency and then a gradual decrease until the signal stabilizes. The change

in frequency from the original baseline is related to the effective mass of the PDDA adsorbed onto the surface of the gold crystal and water closely associated with the PDDA. Both pH 7 and 9 show similar responses to the PDDA adsorption with a final shift in frequency of -5 to -6 Hz. PDDA adsorption with the buffer of 10.5 consistently showed a greater change in frequency - 9.4 ± 1 Hz. The dissipation response (Figure 4. 1) indicates that after rearrangement of the polymer on the gold surface during the buffer rinse, total dissipation is $1 \times 10^{-6}$. The low dissipation value, in relation to the frequency shift, suggests a flat conformation; still, under all three conditions, PDDA could be modeled as a Maxwell layer. The Maxwell model of PDDA indicated a thickness between 1 and 1.6 nm, and accounting for the effective density (1000 kg/m$^3$ for water to 1060 kg/m$^3$ for PDDA), mirrored the Sauerbrey mass (Table 4. 1). The small effective thickness is attributed to the high charge density of PDDA causing a flat conformation of the polyelectrolyte at the surface. This thickness is smaller for a comparable study where PDDA film of approximately 20 Å assembled directly onto gold[40] but does agree with the thickness of films formed on surfaces modified with terminal carboxylic acid groups.[41]

**Table 4. 1** Final Change in Frequency and Related Mass for Adsorption Experiments

| | PDDA on gold | | alkali lignin on gold | | alkali lignin on PDDA | |
|---|---|---|---|---|---|---|
| **pH** | **$\Delta f$ (Hz)** | **mass$^a$(mg/m$^2$)** | **$\Delta f$ (Hz)** | **mass$^b$(mg/m$^2$)** | **$\Delta f$ (Hz)** | **mass$^b$(mg/m$^2$)** |
| **7.0** | **-4.9 ± 0.6** | **1.0 ± 0.2** | **-9.4 ± 0.8** | **1.7 ± 0.1** | **-21.0 ± 2.0** | **3.6 ± 0.4** |
| **9.0** | **-6.0 ± 0.1** | **1.1 ± 0.1** | **-8.2 ± 1.7** | **1.4 ± 0.3** | **-12.7 ± 1.7** | **2.3 ± 0.3** |
| **10.5** | **-9.4 ± 1.0** | **1.6 ± 0.2** | **-6.2 ± 0.2** | **1.1 ± 0.0** | **-13.8 ± 0.8** | **2.2 ± 0.2** |

[a] Sauerbrey mass, which approximates mass derived from Maxwell model. [b] Sauerbrey mass, dissipation $<<1 \times 10^{-6}$.

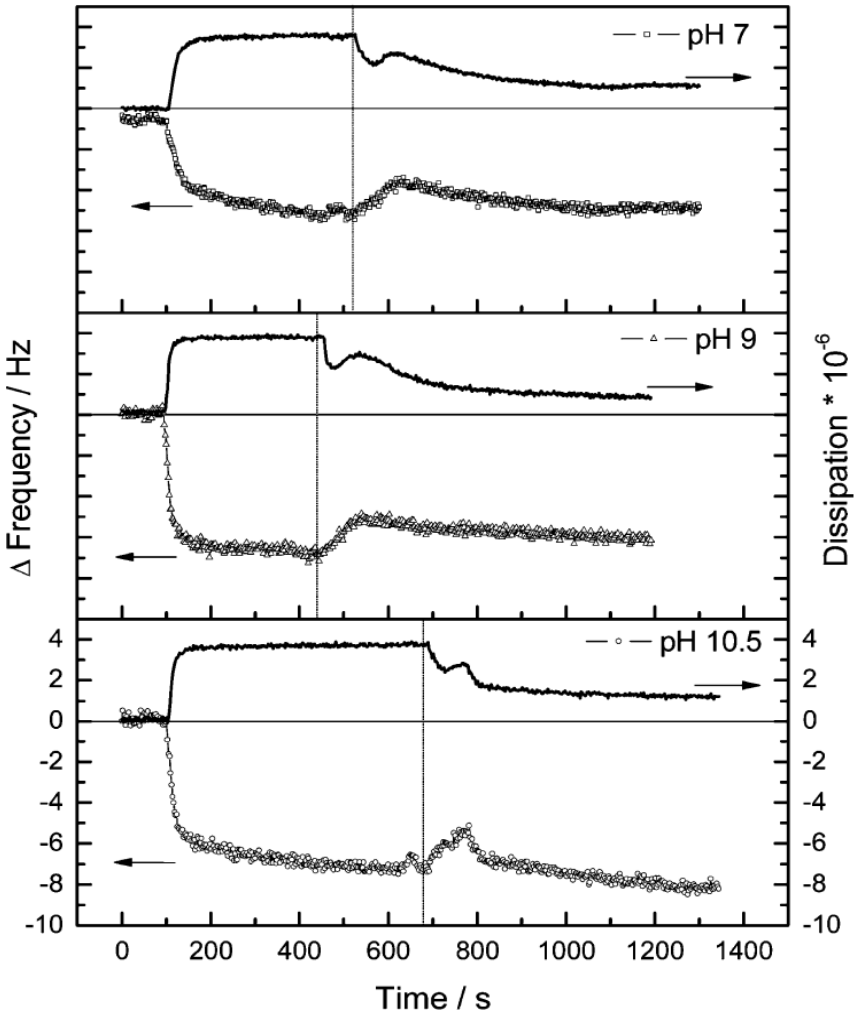


**Figure 4. 1** PDDA adsorption onto gold coated quartz crystal at different solution pH. Note that all axes are the same scale. Vertical lines indicate rinse solution.

From the data (Figure 4. 1), it is concluded that the gold coated surfaces become irreversibly modified with PDDA. Adsorption of alkali lignin onto the gold coated surfaces was also monitored as a function of time and solution pH (Figure 4. 2). Changes in frequency are less than 11 Hz with alkali lignin, adsorbing from a solution pH 7, causing a greater change in magnitude relative to pH 9 and 10.5. Furthermore, frequency change increases at a decreasing rate indicating the association of alkali lignin is finite. In other words, lignin adsorption does not increase under these solution conditions, highlighting the probability that association occurs within the solution and not at the

surface. Hence, differences in frequency change are attributed to the propensity of isolated lignin to associate under neutral conditions. Dissipation does not increase with alkali lignin adsorption, indicating the rigidity of the lignin layer on the crystal. This lignin layer is irreversibly attached as there is minor disassociation of lignin from the gold treated surface when the buffer is reintroduced. Association of the alkali on the gold surface may be promoted with the sulfur groups (2 wt %), but as indicated below, organosolv lignin free of sulfur also adsorbs to gold surfaces. Total mass, from the Sauerbrey relationship shows that alkali lignin adsorbed at pH 7 is approximately twice the mass of pH 10.5 (Table 4. 1). Interestingly, the radius of gyration increases for alkali lignin (MW 4400) from ~ 2 nm above pH 9.5 to 38 nm at pH 6.5, which is related to a 25000× increase in volume.[19] The current data does not reflect the change in volume as reported via diffusion coefficients with no changes in dissipation response at the lower pH. Alkali lignin solutions were adsorbed onto PDDA treated surfaces at increasing concentrations as a function of solution pH (Figure 4. 3). For all three solutions there is an immediate decline in frequency that has decreasing rate of change. When buffer is introduced there is minimal change in frequency at low lignin concentrations (Figure 4. 3, concentrations A-D). Alkali lignin adsorbs irreversibly as a plateau value is reached at concentration of 0.75 mg/L. Final changes in frequency for the lignin films on PDDA are between 12 and 21 Hz dependent upon the pH of the solution. The corresponding masses of the alkali lignin, indicated in Table 4. 1, are 2.2-3.6 mg/m$^2$. The change in mass, above and below the ionization level, follows other weak polyelectrolyte systems where adsorption increases for polymers as segment charge density is decreased. The data

indicates that approximately twice as much alkali lignin is adsorbed onto the charged surface relative to the gold surface for each pH condition.

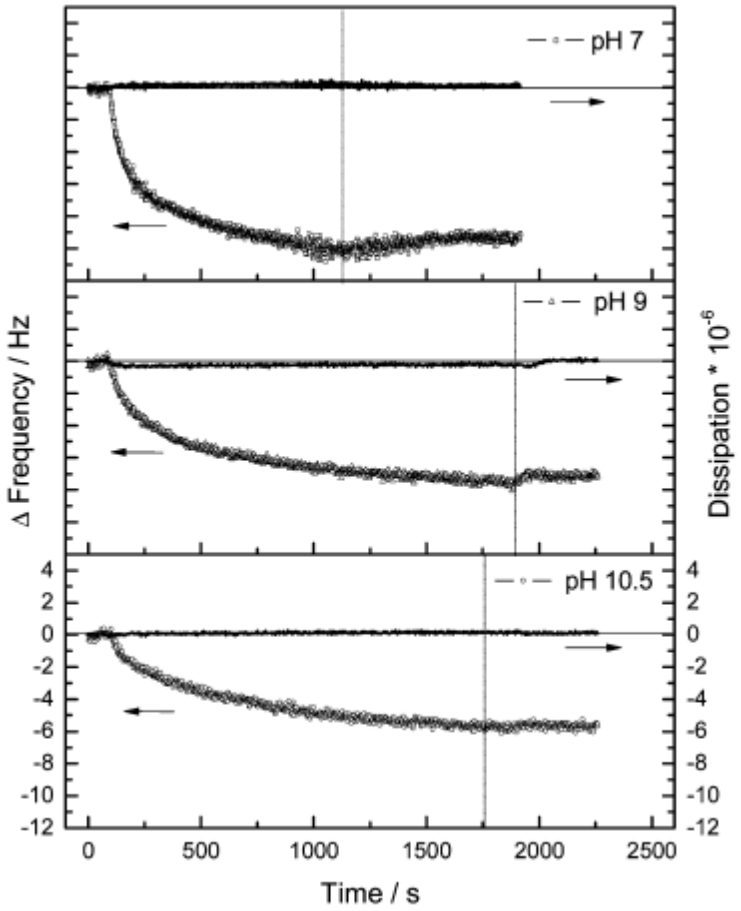


**Figure 4. 2** Alkali lignin adsorption onto gold coated quartz crystal at different solution pH. Note that all axes are the same scale. Vertical lines indicate rinse solution.

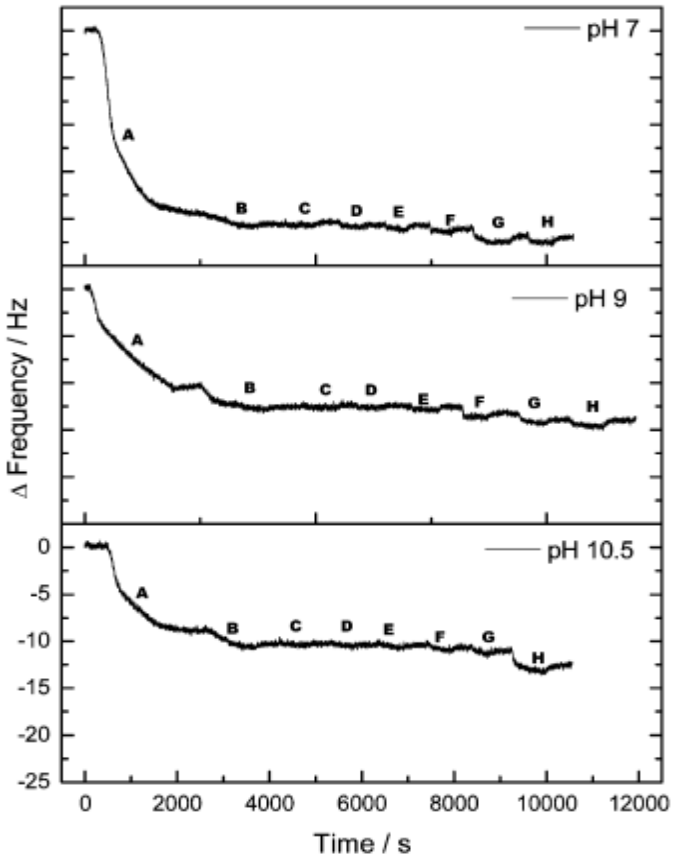


**Figure 4. 3** Alkali lignin adsorption onto PDDA treated surface at different solution pH with increasing concentrations (A: 0.25 mg/L;B: 0.38 mg/L; C: 0.50 mg/L; D: 0.75 mg/L; E: 1.00 mg/L; F: 2.50 mg/ L; G: 5.00 mg/L; H: 10.00 mg/L). Each adsorption step was followed with a buffer rinse. Note that all axes are the same scale.

The data sets were fit to a Langmuir equation, and the Langmuir affinity constants were calculated, with resulting large values (pH 7, 16.46 ± 2.37; pH 9, 17.61 ± 2.63; pH 10.5, 12.51 ± 2.77; Figure 4. 4). Such high affinity constants mean that alkali lignin will saturate the surface at extremely low concentrations. While the saturation values differ, there is not a statistical difference between affinity constants at different pH values (i.e., different levels of ionization). A difference in lignin packing, arising from lignin-lignin macromolecule interactions, is implicated for the difference in total number of sites lignin occupies on the cationic surfaces rather than a change in lignin-surface interactions at

different degrees of ionization. At pH 7.0 the mass of the adsorbed alkali lignin layer on PDDA was 3.6 ± 0.4 mg/m$^2$ compared to 2.3 ± 0.3 and 2.2 ± 0.2 mg/m2 at pH 9.0 and 10.5, respectively. The higher thickness at pH 7.0 cannot be explained on the basis of ion-ion interaction alone, because the total number of charged sites on alkali lignin would be lower at pH 7.0, with contributions from carboxylic acid groups. However, below a pH of 9.0, alkali lignin is known to aggregate,[19] which could explain the greater mass change.

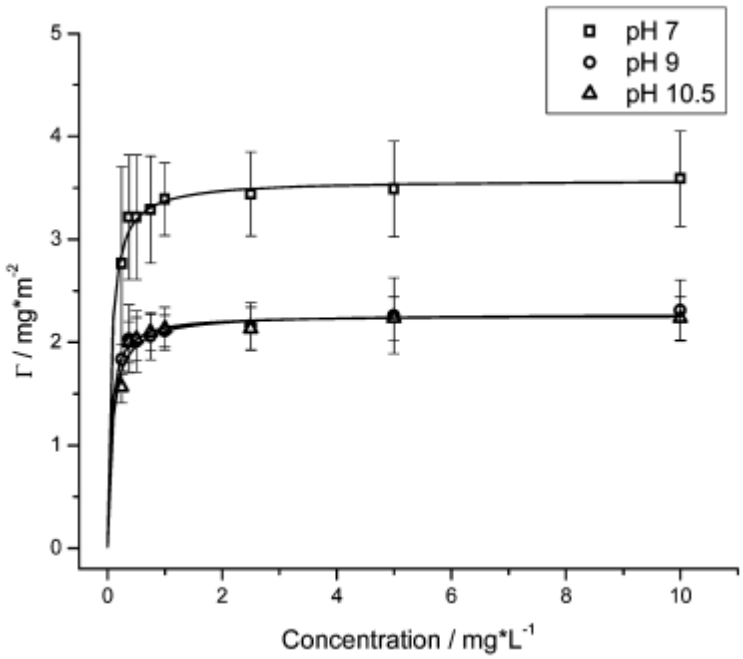


**Figure 4. 4** Surface excess related to frequency change by Sauerbrey relationship as a function of alkali lignin concentration. Each data set was fit with Langmuir equation.

Further studies of the adsorption of alkali lignin on PDDA treated surfaces involved layer-by-layer (LbL) adsorption of alternating layers of PDDA and alkali lignin at pH 7.0 (Figure 4. 5). The result was a linear build up of total film thickness proportional to the number of layers deposited. The initial PDDA layer on gold had a thickness of approximately 1-1.6 nm. The subsequent layers of PDDA on alkali lignin had a smaller

thickness of 5 Å. The thickness of the lignin layers remained constant throughout the adsorption process. This data provides insight that while the conformation of PDDA on the two surfaces (gold and alkali lignin) must be different (see discussion section), each polymer saturates the surface allowing further build-up of multilayers through noncovalent mechanisms.

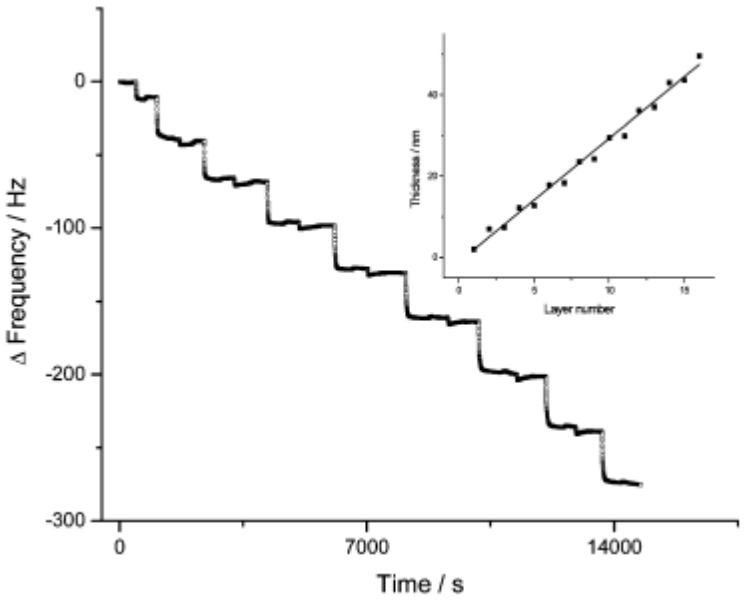


**Figure 4. 5** Layer-by-layer assembly of PDDA and alkali lignin at pH 7. Inset: Linear relationship between thickness, as computed with Sauerbrey mass and layer number.

As a result of the pulping process, kraft lignin possesses a significant number of carboxyl groups. At 90% delignification of softwood pulp, the amounts of carboxylic and phenolic OH groups are approximately 0.5 and 3.6 mmol/g, respectively.[42] At neutral and acidic pH, the phenolic OH groups on alkali lignin are not ionized; however, alkali lignin has negative charge at neutral pH that can be attributed to the ionized carboxyl groups. These ionized carboxylic acid groups could interact with the cationic polyelectrolyte. To further probe the interactions between cationic surfaces and isolated lignin, an organosolv lignin with a lower carboxylic acid content[42] that is soluble in ethanol was adsorbed to both

gold and PDDA treated surfaces. The organosolv lignin adsorbed onto the bare gold surface, but partial desorption occurred after the buffer was introduced (Figure 4. 6). Frequency changed from its plateau value of -5 to -3 Hz after 40 min of rinsing with the buffer. Organosolv lignin that was adsorbed onto PDDA from ethanol had a frequency change of -11.5 Hz and did not desorb when ethanol was introduced. With a dielectric constant of ethanol smaller than water, ionization of the carboxylic acid component is greatly reduced (2 orders of magnitude), providing a way to separate out the Coulombic contribution of the adsorption of lignin to PDDA, while still maintaining solubility of the lignin. It is clear that adsorption to a charged surface occurs when there is, at most, a minor Coulombic component. If the phenol group is modified with a hydrophobic ester group (lignin propionate, LP), adsorption is not significantly impacted indicating that the phenol is not central in docking the lignin on the charged surface (Figure 4. 6). From the same data, increasing hydrophobicity does not promote adsorption, which negates the potential contribution of van der Waals interactions between the methyl groups of the PDDA and the propionate methyl dominating the interaction. In contrast, if the phenol is modified with hydrophilic substituent of equal length (hydroxyl ethyl, HE), adsorption is increased by a factor of 2 (Figure 4. 6). Differences in HE lignin and unmodified lignin are that the HE lignin can associate with itself (different H-bonding patterns) and has the ability to undergo additional ion-dipole interactions, which are also facilitated with low dielectric constant solvents. In summary, organosolv lignin is strongly attracted to cationic surfaces without the contribution of Coulombic interactions and the phenolic group does not have a dominant role in adsorption interaction with cationic surfaces.

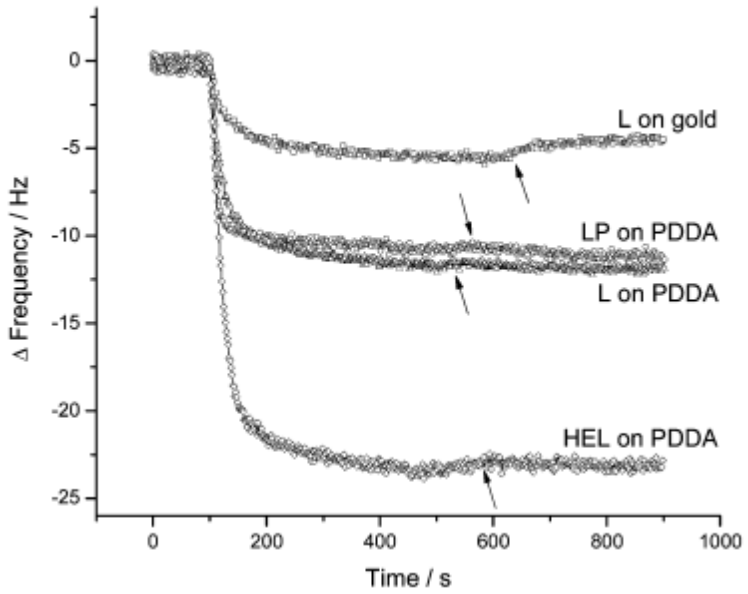


**Figure 4. 6** Organosolv lignin and derivatives adsorption to gold and PDDA treated surfaces from ethanol. Organosolv lignin (L), lignin propionate (LP), and hydroxyethyl lignin (HEL). Arrows indicate rinse solution.

The FTIR spectrum for a dried mixture of alkali lignin and PDDA is compared to the spectra of the individual components, and the main aromatic peak of alkali lignin at 1513.7 $cm^{-1}$ shifts to 1515.6 $cm^{-1}$ for the mixture (Figure 4. 7). The change in peak position is identical to the positive 1.9 $cm^{-1}$ peak shift, previously reported for the adsorption of a quaternary ammonium surfactant onto the aromatic face of a polyphenol.[43] In Figure 4.7, PDDA does not adsorb radiation in this region, allowing the shift to be attributed to the aromatic residues of lignin being in a different environment (i.e., bound to the cation). The other peaks related to the aromatic units of lignin 1600 $cm^{-1}$ and the phenolic groups of lignin 1210 $cm^{-1}$ are found in regions where there is also adsorption of radiation from PDDA making it difficult to judge the influence of the cation, outside of broadening effects. A shift in the main aromatic peak position in

vibrational spectroscopy provides direct evidence for specific cation-$\pi$ interactions, based on previous computational and experimental studies.[43]

## 4. 5 Discussion

Identification of interactions in this system is challenging because modification of the macromolecule or the solution influences solubility and hydrophobicity. Based on the direct evidence of the vibrational shift for the aromatic ring and indirect evidence of adsorption occurring to cationic surfaces in organic solvent and under strongly and weakly ionized conditions in aqueous solvents, we suggest that cation-$\pi$ interactions may assist technical lignin assembly onto cationic surfaces. One clue for this interaction is that cation-$\pi$ interactions occur over van der Waals distances and only involve a partial electrostatic component.[34] A short-range distance would require the polymer to minimize its loops and tails. Notley and Norgren demonstrated that PDDA adsorption to lignin model surfaces have a very small effective thickness and mass when conditions are below the ionized phenolic groups (pH 3-7).[44] When pH increases, where ion-ion interactions can contribute, the effective thickness moves toward 10 nm. While additional adsorption will occur with increased charged density of the surface, this distance also corresponds with the limit of the Debye screening length (decay length of the electrostatic field) under similar solution conditions.[45] In other words, interactions are long ranged for ion-ion interactions and the longer separation distance allows conformational entropy to be increased (even if adsorption of oppositely charged polymers to surfaces is inherently flat).[46] In the same study, adsorption was shown to decrease with addition of salt. While this trend would indicate that ion-ion interactions are the dominant force, competitive adsorption may also be implicated.[45] Adsorption energy of a phenol-sodium ion pair (112

kJ/mol) is greater than the adsorption energy of phenolammonium ion pair.[35] These findings are consistent, that cation-$\pi$ interactions may be operative in this system. In our work we have looked into the layer-by-layer adsorption of alkali lignin and PDDA under neutral pH (Figure 4. 5). While the initial PDDA layer has an effective thickness greater than 1 nm as shown earlier, subsequent layers of PDDA have a thickness of 5 Å (calculated from an effective density). For the PDDA layer on the gold surface, the film can be modeled as a Maxwell viscoelastic layer where the elastic and viscous components are in series. This model requires some of the film to behave like it is extended out into the solution. However, PDDA adsorbed onto the alkali lignin layers fails this model suggesting that the conformation is different, as seen with the small change in frequency of 3 Hz (Figure 4. 5). Complete saturation of the surface (monolayer formation) is assumed by the ability to continue to build sequential layers in a linear manner (Figure 4. 5 inset). By reintroducing the same alkali lignin solution without PDDA, no additional lignin mass can be deposited (Figure 4. 3). Also, we have observed the addition of electrolyte to the PDDA solution negatively impacts the ability to build layer-by-layer films. These findings support that PDDA will strongly adsorb to a weakly charged surface with an effective thickness that would require operating across van der Waals interaction distances (i.e., cation-$\pi$ interactions). PDDA and kraft lignin polyelectrolyte complexes have been studied as function of pH.[31] The authors report charge neutralization as only part of the mechanism of precipitate formation. Under some conditions, 75% of the available charges on the kraft lignin are not neutralized in the precipitated complex. This fact would point to non-Coulombic interactions dominating complex formation by bridging lignin macromolecules together with the energy

minimum being found by complexing the phenyl ring, in contrast to the ionized charged groups of the lignin. In theory, a weakly ionizable polyelectrolyte should form ion pairs with the strong polyelectrolyte when the quantity of ionizable groups is smaller than the DP of the strong polyelectrolyte,[47] however this system does not show ion pairing. In another study, ion pair formation between a variety of isolated lignins and Aliquat 336, an ammonium surfactant, was exploited to form soluble complexes in organic solvents.[48] However, considering stoichiometry of the system, there is no clear ion pairing relationship, and solubility only occurred after 1000× the critical micelle content of the surfactant. Both of these systems indicate that Coulombic interactions may not dominate the system and other noncovalent interactions are implicated. In the current work, technical lignins, isolated in industrial operations, are used that are not model native lignins (such as the enzymatic mild acidolysis lignin[24]). Differences between the lignins are found based on molecular weight, chemical linkages, and chemical functionality such as phenolic content per phenylpropane unit.[5] When comparing the associative nature of native lignins, there is a substantial species effect.[24] Similarly, there should be inherent differences in the amount of lignin adsorbed at cationic surfaces based on the source of lignin and how it was isolated. However, like technical lignins, model native lignins and lignin precursors have aromaticity that would give rise to the ability of lignin to interact with cationic surfaces with the cation-$\pi$ mechanism. There are biological implications for lignin aromatic groups having an affinity for cationic groups, as the plant cell wall is rich in cationic ions such as $Ca^{2+}$ [49] and dirigent proteins are shown to control the lignification process.[10] While claims from this particular study cannot be made in regard to phenylpropane substituents being patterned within the cell wall by divalent cations or

cationic side chain amino acids (such as arginine, histidine, and lysine), specific mechanisms that can shed light on the nonrandom order of lignin within the cell wall are worth considering in future studies. Whether or not we can trace complex biological events to specific noncovalent interactions that govern molecular architecture, we certainly can exploit the noncovalent interactions in the utilization of these biopolymers. If we consider that a plant can use lignin to change its hydrophilicity, a similar strategy can be used to exploit isolated lignin's great propensity to assembly onto cationic surfaces. From this work, new strategies can be developed to link aromatic polymers to positively charged substrates that can displace the hydration shell from the charged surface.

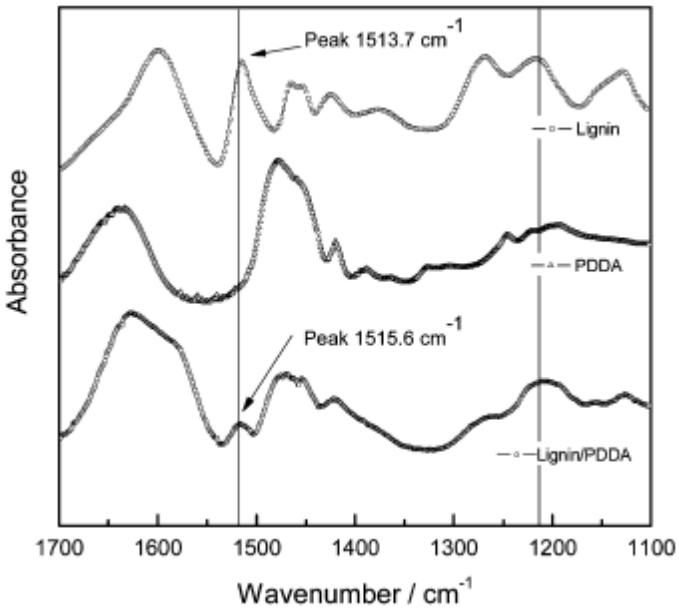


**Figure 4. 7** FTIR transmission spectra of alkali lignin, PDDA, and dried complex. Note the shift related to aromatic skeletal vibration at 1515 $cm^{-1}$.

## 4. 6 Conclusions

Adsorption occurs for technical lignin at all solution conditions (ionized and only partially ionized) onto gold surfaces and approximately doubles in magnitude for positively charged surfaces. Affinity coefficients are equal for alkali lignins at all solution pHs, which indicates that adsorption potential is similar for these conditions. Partially ionized lignin has greater thickness at the solid solution interface, which may result from aggregation within solution. In ethanol, where dissociation of the phenolic and carboxylic acid components are low, organosolv lignin adsorption occurs covering the surface. Even after chemical modification of organosolv lignin, by substituting the phenolic hydroxyl group with a hydrophobic methyl, lignin adsorption to a charged surface of PDDA is unchanged. Another mechanism is proposed outside of ion-ion interactions because lignin adsorption behavior is either increased by lower ionization (similar to other weak polyelectrolytes) or remains unchanged. Evidence for interaction between the aromatic groups of alkali lignin and the cationic groups of PDDA was found with infrared spectroscopy. This work implicates the cation-$\pi$ interaction as a mechanism in assisting the adsorption of technical lignin to charged surfaces.

## 4. 7 References


1. Sjöstrom, E. *Wood Chemistry: Fundamentals and Applications*, *2nd* ed.; Academic Press: San Diego, CA, 1993; p 293.

2. Bals, B.; Teachworth, L.; Dale, B.; Balan, V. *Appl. Biochem. Biotechnol.* **2007**, *143*, 187–198.

3. Francis, R. C.; Hanna, R. B.; Shin, S. J.; Brown, A. F.; Riemenschneider, D. E. *Biomass Bioenergy* **2006**, *30*, 803–808.

4. Pan, X.; Gilkes, N.; Kadla, J.; Pye, K.; Saka, S.; Gregg, D.; Ehara, K.; Xie, D.; Lam, D.; Saddler, J. *Biotechnol. Bioeng.* **2006**, *94*, 851–861.

5. Glasser, W. G.; Barnett, C. A.; Muller, P. C.; Sarkanen, K. V. *J. Agric. Food Chem.* **1983**, *31*, 921–30.

6. Zhang, Y.-H. P.; Ding, S.-Y.; Mielenz, J. R.; Cui, J.-B.; Elander, R. T.; Laser, M.; Himmel, M. E.; McMillan, J. R.; Lynd, L. R. *Biotechnol. Bioeng.* **2007**, *97*, 214–223.

7. Gargulak, J. D.; Lebo, S. E. In *Lignin: Historical, Biological, and Materials Perspectives*; Glasser, W. G., Northey, R., Schultz, T. Eds.; American Chemical Society: Washington, DC, 2000; pp 304-320.

8. Lora, J. H.; Glasser, W. G. *J. Polym. Environ.* **2002**, *10*, 39–48.

9. Chen, Y.-R.; Sarkanen, S. *Phytochem. Rev.* **2004**, *2*, 235–255.

10. Gang, D. R.; Costa, M. A.; Fujita, M.; Dinkova-Kostova, A. T.; Wang, H.-B.; Burlat, V.; Martin, W.; Sarkanen, S.; Davin, L. B.; Lewis, N. G. *Chem. Biol.* **1999**, *6*, 143–151.

11. Li, Y.; Mlynar, J.; Sarkanen, S. *J. Polym. Sci., Part B: Polym. Phys.* **1997**, *35*, 1899–1910.

12. Lindstrom, T. *Colloid Polym. Sci.* **1979**, *257*, 277–285.

13. Lindstrom, T. *Colloid Polym. Sci.* **1980**, *258*, 168–173.
14. Norgren, M.; Edlund, H.; Wagberg, L. *Langmuir* **2002**, *18*, 2859–2865.

15. Norgren, M.; Edlund, H.; Wagberg, L.; Lindstrom, B.; Annergren, G.*Colloid Surf., A* **2001**, *194*, 85–96.

16. Nyman, V.; Rose, G. *Colloids Surf.* **1986**, *21*, 125–147.

17. Mafe, S.; Manzanares, J.; Kontturi, A.-K.; Kontturi, K. *Bioelectrochem. Bioenerg.* **1995**, *38*, 367–375.

18. Norgren, M.; Lindstrom, B. *Holzforschung* **2000**, *54*, 528–534.

19. Garver, T. M.; Callaghan, P. T. *Macromolecules* **1991**, *24*, 420–430.

20. Sarkanen, S.; Teller, D. C.; Hall, J.; McCarthy, J. L. *Macromolecules* **1981**, *14*, 426–434.

21. Sarkanen, S.; Teller, D. C.; Stevens, C. R.; McCarthy, J. L. *Macromolecules* **1984**, *17*, 2588–2597.

22. Woerner, D. L.; McCarthy, J. L. *Macromolecules* **1988**, *21*, 2160–2166.

23. Dutta, S.; Garver, T. M.; Sarkanen, S. In *Lignin: Properties and Materials*; Glasser, W. G., Sarkanen, S., Eds.; American Chemical Society: Washington, DC, 1989; pp 155-176.

24. Guerra, A.; Gaspar, A. R.; Contreras, S.; Lucia, L. A.; Crestini, C.; Argyropoulos, D. S. *Phytochemistry* **2007**, *68*, 2570–2583.

25. Contreras, S.; Gaspar, A. R.; Guerra, A.; Lucia, L. A.; Argyropoulos, D. S. *Biomacromolecules* **2008**, *9*, 3362–3369.

26. Micic, M.; Benitez, I.; Ruano, M.; Mavers, M.; Jeremic, M.; Radotic, K.; Moy, V.; Leblanc, R. M. *Chem. Phys. Lett.* **2001**, *347*, 41–45.

27. Takahashi, N.; Azuma, J.; Koshijima, T. *Carbohydr. Res.* **1982**, *107*, 161–168.

28. Maximova, N.; Osterberg, M.; Koljonen, K.; Stenius, P. *Cellulose* **2001**, *8*, 113–125.

29. Maximova, N.; Osterberg, M.; Laine, J.; Stenius, P. *Colloid Surf., A* **2004**, *239*, 65–75.

30. Paterno, L. G.; Mattoso, L. H. C. *Polymer* **2001**, *42*, 5239–5245.

31. Lappan, R. E.; Pelton, R.; McLennan, I.; Patry, J.; Hrymak, A. N. *Ind. Eng. Chem. Res.* **1997**, *36*, 1171–1175.

32. Dougherty, D. A. *Science* **1996**, *271*, 163–8.

33. Gallivan, J. P.; Dougherty, D. A. *Proc. Natl. Acad. Sci. U.S.A.* **1999**, *96*, 9459–64.

34. Mecozzi, S.; West, A. P., Jr.; Dougherty, D. A. *Proc. Natl. Acad. Sci. U.S.A.* **1996**, *93*, 10566–10571.

35. Ma, J. C.; Dougherty, D. A. *Chem. Re*V. **1997**, *97*, 1303–1324.

36. Kim, K. S.; Lee, J. Y.; Lee, S. J.; Ha, T.-K.; Kim, D. H. *J. Am. Chem. Soc.* **1994**, *116*, 7399 400.

37. Sauerbrey, G. Z. *Z. Phys.* **1959**, *155*, 206–222.

38. Voinova, M. V.; Rodahl, M.; Jonson, M.; Kasemo, B. *Phys. Scr.* **1999**, *59*, 391–396.

39. Adamson, A. W.; Gast, A. P. *Physical Chemistry of Surfaces*; Wiley: New York, 1997; p 784.

40. Kotov, N. A.; Dekany, I.; Fendler, J. H. *J. Phys. Chem.* **1995**, *99*, 13065–9.

41. Zhang, L.; Longo, M. L.; Stroeve, P. *Langmuir* **2000**, *16*, 5093–5099.

42. Liu, Y.; Carreiro, S.; Pye, K.; Argyropoulos, D. S. In *Lignin: Historical, Biological, and Materials Perspectives*; Glasser, W. G., Northey, R. A., Schultz, T. P., Eds.; American Chemical Society: Washington, DC, 2000; pp 447-464.

43. Xu, L.; Yokoyama, E.; Watando, H.; Okuda-Fukui, R.; Kawauchi, S.; Satoh, M. *Langmuir* **2004**, *18*, 7064–7069.

44. Notley, S. M.; Norgren, M. *Biomacromolecules* **2008**, *9*, 2081–2086.

45. Israelachvili, J. *Intermolecular and surface forces*; Academic Press: Amsterdam, 1991; p 450.

46. Van de Steeg, H. G. M.; Cohen Stuart, M. A.; De Keizer, A.; Bijsterbosch, B. H. *Langmuir* **1992**, *8*, 2538–46.

47. Kabanov, V. In *Multilayer Thin Films*; Decher, G., Sclenoff, G. B., Eds.; Wiley-VCH: Weinheim, 2003; pp 47-86.

48. Majcherczyk, A.; Huettermann, A. *J. Chromatogr., A* **1997**, *764*, 183–191.

49. Buchanan, B., Gruissem, W., Jones, R. *Biochemistry and Molecular Biology of Plants*; American Society of Plant Biologists: Rockville, MD, 2000; p 1367.

# Chapter 5. Bottom-up Lignocellulosic Composites: Study of Layer-by-Layer Assembly of Isolated Wood Polymers

## 5. 1 Abstract

Woody materials are comprised of plant cell walls that contain a layered secondary cell wall composed of polysaccharides and lignin. Layer-by-layer (LbL) assembly process was used to build a free standing composite film of a simplified architecture from isolated wood polymers, lignin and oxidized nanocellulose fibrils (NC). Two types of lignins, namely organosolv lignin (OL) and hardwood milled wood lignin (HMWL) were used in this study. To facilitate assembly of these polymers, a cationic polyelectrolyte poly(diallyldimethylammomium chloride) (PDDA), was used as linking layer to create this simplified version of the cell wall. The layered adsorption process was studied quantitatively using quartz crystal microbalance with dissipation monitoring (QCM-D) and ellipsometry. Adsorption response from QCM-D showed sequential adsorption of multilayers with the three different polymers. The two types of lignins used, HMWL and OL, were found not to significantly differ in adsorption, albeit their differences in molecular weight and chemical structure. Two viscoelastic models, namely Johannsmann and Voigt, were used to calculate the areal mass and the thickness of the adsorbed layers. The results showed that layer mass/thickness per adsorbed layer increased as a function of total number of layers. The surface coverage of the adsorbed layers was studied with atomic force microscopy (AFM). Complete coverage of the surface with lignin in all the deposition cycles was found for the system, however, surface coverage by NC was seen to increase with the number of layers. The adsorption process was carried out for 250

cycles (500 bilayers) on a cellulose acetate (CA) substrate. Transparent free-standing LBL assembled nanocomposite films were obtained when the CA substrate was later dissolved in acetone. Scanning electron microscopy (SEM) of the cryo-fractured cross-sections showed a lamellar structure, and the thickness per adsorption cycle (PDDA-Lignin-PDDA-NC) was estimated to be 17 nm for the two different lignin types. The data indicates an architecture where nanocellulose and lignin are associated intimately across a few nanometers, similar to what is observed in the native cell wall.

## 5. 2 Introduction

Natural materials like wood are polymer-polymer composites displaying a combination of high stiffness and toughness.[1] These properties are achieved by the controlled arrangement and organization of the constituent materials into hierarchically ordered structures.[2, 3] Wood is primarily made up of non-living xylem cells, the structural integrity and strength of which is derived from the exocellular lignified secondary cell wall.[4] A closer look at the ultrastructure of the secondary cell wall reveals that it is a nanocomposite composed of paracrystalline cellulose microfibrils embedded in an amorphous matrix of lignin and hemicelluloses.[5-7] The longitudinally oriented cellulose microfibrils are approximately 3-5 nm in diameter and are aggregated together to form larger units called cellulose fiber bundles.[8] The fiber bundles are embedded in a lignin-hemicellulose complex, which is composed of an amorphous polymer composed of phenyl-propanol units with some linkages to hetero-polysaccharides like glucoronoxylan.[7]

For synthetic composites, blending high aspect ratio and high moduli nanoparticles in a polymer matrix can lead to significant improvements in mechanical and thermal properties compared to the neat polymer.[9-11] Nanoparticles that have been used as reinforcements have moduli in the range of 148 GPa for cellulose nanocrystals (CNXs),[12] 138 – 400 GPa for clay particles,[13] and up to 1 TPa for carbon nanotubes[14, 15] One important advantage of using nano-reinforcement or nano-fillers is that only a small amount (1-5%) of the material is required for the desired property enhancement. This result is due to the dramatic increase in surface area of the nanoparticles compared to conventional reinforcements or fillers. However, incorporation of these particles into composites is not always accompanied by an improvement in properties due to poor dispersion and lack of interfacial attachment within the matrix.[15] An alternate route for the creation of nanocomposite materials is the LbL assembly technique, which is based on the sequential adsorption of polymers or nanoparticles with complementary charges or functional groups to form organized multilayered composite films.[16-19] Free-standing hybrid nanocomposites of high strength, made by LbL deposition of polymer and nanoparticles have been reported by Kotov et al.[20-24] Among many other applications, LbL films have also been investigated for their potential use in therapeutic delivery[25], fuel cell membranes,[26, 27] batteries,[28] and lignocellulosic fiber surface modification.[29-31]

The recent interest in nanoscale cellulose based composite materials have led to the preparation and characterization of LbL multilayers of CNXs prepared by sulfuric acid hydrolysis of cotton fibers, and positively charged polyelectrolytes.[32-36] Similar studies have also been conducted with cellulose nanowhiskers obtained from marine tunicin and

cationic polyelectrolytes,[37] CNX and xyloglucan,[38] and CNX and chitosan.[39] LbL multilayer formation of carboxylated microfibrillated celluloses (MFCs), obtained by high pressure homogenization of pulp fibers, with cationic polyelectrolytes has also been studied.[40-42] The preparation, properties, and application of CNXs and microfibrillated cellulose have been reviewed in detail.[43, 44]

The present study involves the examination of LbL technique as a potential way to assemble isolated lignocellulosic polymers in an ordered fashion, as a first step towards a biomimetic lignocellulosic 3-dimensional composite. The LbL technique was selected for its benign processing conditions, such as ambient temperature, pressure, and water as the solvent, which are conditions under which some of the remarkable natural composites are made.[45] In this study we report on the multilayer build-up of constitutive wood components. The LbL adsorption was studied with quartz crystal microbalance with dissipation monitoring (QCM-D), ellipsometry and atomic force microscopy (AFM). We also report for the first time the creation of free-standing lamellar films composed of these polymers, created by the LbL technique.

## 5. 3 Materials and Methods

The two types of lignins used in this study were organosolv lignin (OL; Sigma Aldrich, Inc) and hardwood milled wood lignin (HMWL).[46] Nanocellulose (NC) was produced from never dried sulfate pulp (brightness level of 88%), supplied by Weyerhaeuser Inc. The cationic polymer used in this study was PDDA (Sigma Aldrich: $M_n = 7.2\times10^4$, $M_w$ of $2.4\times10^5$).

### 5. 3. 1 TEMPO-mediated Oxidation and Fibrillation of Pulp Fibers

TEMPO (2,2,6,6-tetramethyl piperidine-1- oxyl) mediated oxidation of never dried kraft pulp was carried out using a method described by Saito et al.[47] with slight modification. Briefly, the pulp (20 g, 1% w/v, dry weight basis) was mixed with TEMPO (0.313 g, 0.1 mmol) and NaBr (2.0 g, 1 mmol) in a 3 L three-neck flask until the fibers were well dispersed in 2.0 L of water (Milli-Q, 18.5 MΩ.cm). The oxidation was initiated by slowly adding a 12% solution of NaOCl (64.7 ml, 5 mmol/g of cellulose) to the reaction mixture, while maintaining the pH of the mixture at 10 by adding 0.5 M NaOH. The reaction was stopped when no further addition of NaOH was required to maintain the pH. The oxidized fibers were thoroughly washed with Milli-Q water to remove the reagents and stored at 4 °C for further use. The carboxyl content of the oxidized pulp was determined by conductometric titration. A 3 % (w/v, dry weight basis) slurry of the TEMPO oxidized pulp was beaten in a Warring blender until the slurry became viscous and the blades started spinning in air. The blended slurry was diluted to 0.1% (w/v) and nanofibrillated by ultrasonication with a Sonics® (Model GE 505) ultrasonic processor for 15 min. The ultrasonicated samples were centrifuged at 5000 rpm for 5 min and the transparent supernatant containing the fibrillated nanocellulose fraction was decanted, freeze-dried and stored for further use. Past experiments have shown that these fibrils have lengths of 530 nm and thickness of 1.4 nm.[48]

### 5. 3. 2 Analysis of Lignin

#### *5. 3. 2. 1 Lignin Acetylation*

100 mg of the lignin samples were dissolved in 8.0 ml 1:1 mixture of acetic anhydride and anhydrous pyridine, and incubated at room temperature for 24 hrs. The acetylated

sample was precipitated by adding 80 ml 0.1 N HCl to the reaction mixture. The precipitate was filtered and washed 5 times with 0.1 N HCl to remove excess pyridine, followed by washing 5 times with Milli-Q water. The filtrate was vacuum-dried for 24 hrs and stored for further use.

#### *5. 3. 2. 2 Size Exclusion Chromatography*

Acetylated lignin samples were accurately weighed (5.8 – 6.2 mg) and dissolved in 1 ml of $CHCl_3$. Aliquots of 100 ml of the dissolved samples were analyzed with a Waters alliance 2690 separations module system equipped with Waters styragel HR 0.5, HR 2, HR 3 and HR 4 columns connected in series. The analysis was done at 30 °C and a flow rate of 1.0 ml/min using a universal calibration method. The instrument was attached to Viscotek laser refractometer, and Viscotek T60A dual detectors and calibrated using polystyrene standards in the molecular weight range of 575 – 70,950 g $mol^{-1}$.

#### *5. 3. 2. 3 $^{1}H$ NMR*

Approximately 10 mg of the acetylated lignin samples were dissolved in 0.75 ml $CDCl_3$. The solution was transferred to 5 mm NMR tubes and the spectra were collected in a Varian Inova 400 MHz spectrometer at 30 °C.

### 5. 3. 3 Quartz Crystal Microbalance

LbL adsorption process was measured using a QCM-D E4 system (Q-Sense Inc.) capable of measuring the fundamental frequency of the vibrating quartz crystal and its odd harmonics/overtones from 3 to 13. In addition to the frequency, the E4 system also measured the associated dissipation factors. In this study, gold coated piezoelectric quartz crystals (Q-sense Inc.) were used for all experiments. Prior to the experiments the crystals

were cleaned in a base piranha solution (3 parts concentrated $NH_4OH$ to 1 part $H_2O_2$ at 60 °C) for 10 min, rinsed with Milli-Q water and blown dry in a stream of $N_2$.

### 5. 3. 4 Ellipsometry

Ellipsometry measurements were carried out in multiple angle of incidence mode with a phase modulated ellipsometer (Beaglehole instruments) at a wavelength of 632.8 nm in air. The angles were varied between 85° and 65° at 1° intervals. LbL films for ellipsometry measurements were deposited on silicon wafers, which were first cleaned with acid piranha (3 parts $H_2SO_4$ to 1 part $H_2O_2$) for 20 minutes prior to layer deposition.

### 5. 3. 5 Atomic Force Microscopy (AFM)

Surface imaging of the deposited layers were carried out using an MFP3D Bio-AFM (Asylum Research). The images were collected in tapping mode with 10 nm radius silicon tips (spring constant 42 N/m). LbL films for AFM imaging were deposited on freshly cleaved mica substrate.

### 5. 3. 6 LbL Film Deposition

LbL adsorption was carried out for QCM-D, ellipsometry and AFM experiments according to the following steps (5 min each step) : 1) 0.5% (w/v) PDDA (pH 10.5), 2) buffer (pH 10.5 Milli-Q water), 3) 0.01% (w/v) lignin (pH 10.5), 4) buffer, 5) 0.5% (w/v) PDDA (pH 10.5), 6) buffer, 7) 0.1% (w/v) NC, pH 8) buffer. Steps 1 through 8 represents one deposition cycle with two bilayers (PDDA:MWL and PDDA:NC). The LbL deposition experiments for QCM-D and ellipsometry were carried out in triplicates.

### 5. 3. 7 Preparation of Free-Standing LbL Film

The steps described under LbL film deposition were carried out on a CA substrate using a custom made robot. Once the desired number of layers was deposited, the film was air-dried, the edges trimmed, and extracted by dissolving the CA substrate in acetone. The isolated LbL films (2 films per CA substrate) were soaked in acetone for 24 hours and further washed repeatedly at least 5 times to maximize the removal of residual CA. Note, during acetone washing, the solution remained transparent indicating that lignin was not removed in the process.

## 5. 4 Results and Discussion

### 5. 4. 1 Lignin Differences

GPC analysis of acetylated samples of HMWL showed an $M_n$ of 5300 and $M_w$ of 31,900 g/mol. The $M_n$ and $M_w$ of OL were determined to be 1300 and 3800 g/mol respectively. The fraction of aromatic: aliphatic acetate hydrogen determined from the $^1$H NMR analysis of the acetylated lignin samples were found to be 0.22 : 0.19, and 0.08 : 0.31 respectively for OL and HMWL (Appendix A 5-2). Thus, OL was found to have a significantly higher phenolic content, which would account for a greater number of ionizable phenolic groups at an elevated pH. The total acid number of the two lignins determined by conductometric titrations was 0.41 ± 0.02 and 0.34 ± 0.03 mmol/g, respectively, for OL and HMWL. The acid number determined by conductometric titration represents the contribution from both the phenolic and the carboxylic content present in lignins. Hence the slightly higher charged lignin, which has a lower molecular weight, forms a marginally smaller thickness in the initial frequency change. A difference in deposition is usually noteworthy for polyelectrolyte adsorption onto charged surfaces

as segment charge and MW change.[59] In the first two deposition cycles, organosolv lignin has an areal mass half of the value for the milled-wood lignin. This trend is also observed with the ellipsometry, as thickness of NC-PDDA-OL in the first and second cycle is lower than NC-PDDA-HMWL. However, this study shows that there is minimal change in the third and fourth cycles, as well as when the process is repeated 250 times. The sheer number of cycles should magnify small differences in adsorption. The data suggests that lignin with disparate structure and chemistry does not greatly impact the fabrication of free-standing films. Hence, either technical lignins, available from biomass conversion into paper, fuels, and chemicals, or model lignins carefully isolated can be used to form free standing films with nanocellulose. This fact is significant where lignins of different origins can be carefully selected to make model cell wall surfaces.

### 5. 4. 2 QCM-D

The LbL adsorption of lignin, NC and PDDA was monitored in real-time with QCM-D with two types of lignins. A detailed description of the QCM-D response in one deposition cycle, which involves two bilayers (PDDA:HMWL and PDDA:NC), is shown in Figure 5. 1, which represents the normalized change in frequency and dissipation of the $7^{th}$ overtone. The $7^{th}$ overtone was arbitrarily chosen, since all overtones except for the $1^{st}$ overtone, shows the same adsorption trend albeit their difference in absolute values. This phenomenon is discussed in more detail in the subsequent section on viscoelastic models. A baseline was first obtained with pH 10.5 Milli-Q water (termed as buffer), followed by introduction of the cationic polymer, PDDA. The introduction of the polymer (step 1) is associated with a decrease in $\Delta F$, and a corresponding increase in $\Delta D$. This response is attributed to a combination of adsorption of PDDA on the gold coated

quartz substrate, and the change in the bulk effects of the liquid in contact with the vibrating crystal. Step 1 was followed by a rinse step (step 2) with buffer to remove the excess/unbound polymer, and to negate the frequency and dissipation response due to the bulk effects of the polymer solution. Therefore, a rinse was performed after each polymer adsorption step. The net change in ΔF and ΔD from the baseline after step 2 is due to the irreversible adsorption of PDDA. In step 3, the lignin solution was introduced, which resulted in a decrease in ΔF and a corresponding increase in ΔD. Step 4, the rinse step caused a slight increase in ΔF, however the ΔD remained unchanged, which suggest that lignin is deposited as a rigid layer over the PDDA layer in contact with gold coated quartz substrate. To deposit the second bilayer, (PPDA:NC), the PDDA solution was reintroduced over the lignin layer (step 5). The introduction of PDDA solution was associated with a slight decrease in ΔF, and a significant increase in ΔD. However, after the initial drop, there was a gradual increase in ΔF followed by a plateau. The net change in ΔF and ΔD after the deposition of PDDA on the lignin layer (ΔF = - 31.6 Hz; ΔD = $1.3 \times 10^{-6}$ ) was found to be slightly lower than the previous layer (ΔF = - 33.2 Hz; ΔD = $1.7 \times 10^{-6}$). This change was associated to the strong interaction between PDDA and lignin,[49, 50] which may have caused partial desorption of loosely bound lignin deposited in step 3 (note in AFM section below, lignin remains in system) . In step 7, the NC solution was introduced on the PDDA layer, which resulted in an increase in ΔF and a corresponding decrease in ΔD. The change was found to be irreversible after the rinse step (step 8), which suggests that NC has been irreversibly deposited on PDDA. In the current study, only four deposition cycles (8 bilayers, 4 cycles) were carried out, because the ΔF and ΔD change beyond this number of cycles was found not to be reproducible.

Figure 5.2 shows the normalized change in ΔF and ΔD of the 7th overtone as a result of the sequential adsorption of polymers PDDA, HMWL and NC after four deposition cycles. It was noted that the adsorption of the polymers did not follow a linear change in ΔF and ΔD with the addition of each bilayer, which has also been noted with other LbL systems.[42, 51] The LbL adsorption of NC, PDDA and OL (NC-PDDA-OL), shown in Figure 5.3, was found to follow the sequential adsorption process observed with NC-PDDA-HMWL. Nonetheless, the systems were found to differ with respect to the exact amount of the polymers deposited in each layer. The difference between these two systems is in the type of the lignin used, as the cationic polymer and NC used were the same in both systems. Thus, any difference between the two systems should arise from the difference in the lignin type.

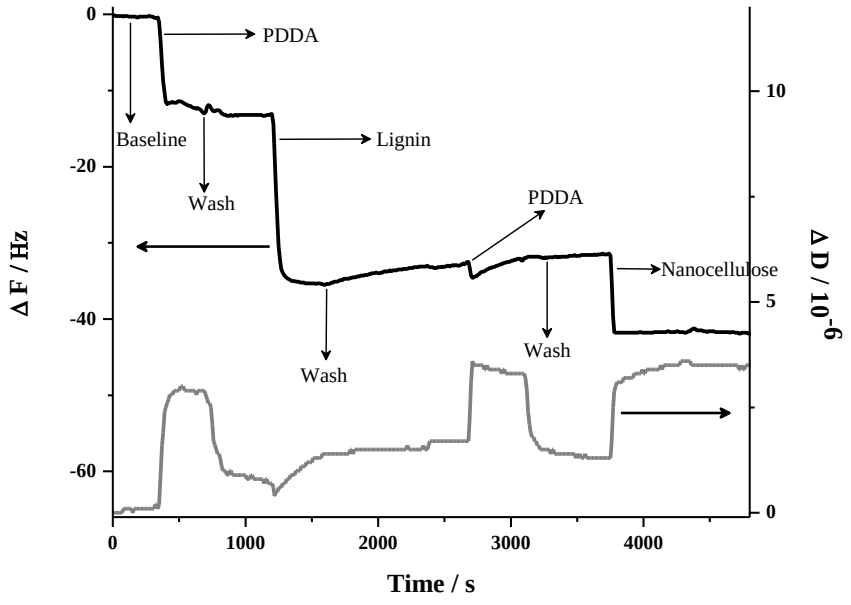


**Figure 5. 1** Description of the steps involved in the 1st deposition cycle of LbL adsorption of NC-PDDA-HMWL. The normalized change in ΔF and ΔD of the 7th harmonic is presented in figure.

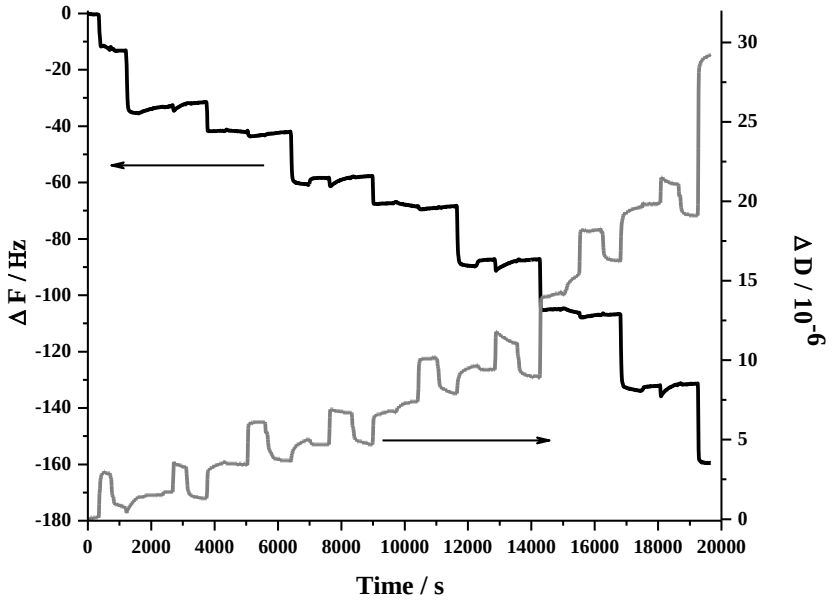


**Figure 5. 2** Frequency and dissipation response of the 7$^{th}$ harmonic as a result of the LbL adsorption of NC-PDDA-HMWL in four deposition cycles (8 bilayers).

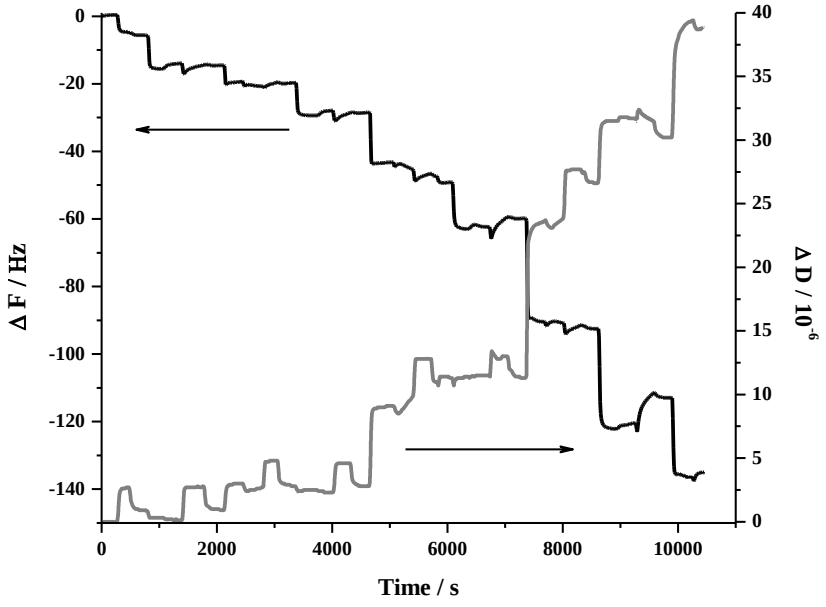


**Figure 5. 3** Frequency and dissipation response of the 7$^{th}$ harmonic as a result of the LbL adsorption of NC-PDDA-OL in four deposition cycles (8 bilayers).

### 5. 4. 3 QCM-D Viscoelastic Modeling

The mass/thickness of the adsorbed polymer layers can be determined by the Sauerbrey relationship. However, it is only valid under the assumption that the deposited layer is rigid, and the whole system performs as a composite resonator. This can be verified subjectively by noting the change in $\Delta D$ with respect to $\Delta F$. A higher $\Delta D$ change with respect to change in $\Delta F$ (>1 x $10^{-6}$ per 10 Hz) indicates a more dissipative and viscoelastic film[41], and a lower $\Delta D$ suggests a more rigid and elastic film. Another indication of a non-rigid viscoelastic film, which leads to deviation from the Sauerbrey relation, is the frequency dependence of the overtones ($\Delta F/n$). Figure 5.4 shows that with the increase in the number of layers, the overtones start to move farther apart, which suggests that as the thickness increases, the response of the films tend to be viscoelastic.[41] For a thicker or viscoelastic film, the nature of propagation of the shear acoustic wave into and through the film affects the estimation of the coupled mass.[52] Therefore, in such cases, $\Delta F$ is not directly proportional to change in mass ($\Delta m$). Also, the mass estimated with QCM-D may include coupled water due to hydration, viscous drag, and entrapment. The amount of coupled water varies depending on the nature of the adsorbed film, and can typically range between 1.5 to 4 times the molar mass of the adsorbed material.[52]

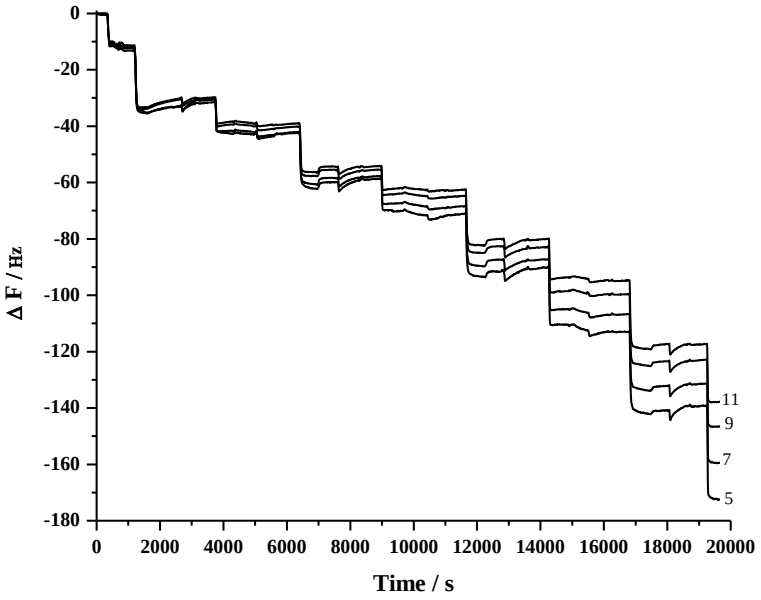


**Figure 5. 4** Frequency response of the odd harmonics 5 to 11 as a result of the LbL adsorption of PDDA, HMWL and NC, showing the frequency dependence of the harmonics as the number of layers increase.

### *5. 4. 3. 1 Areal Mass Estimate*

The Johannsmann model, which determines the sensed mass of a viscoelastic layer, has been used to study the adsorption characteristics of different systems like polyelectrolyte complexes on polystyrene substrates,[53] proteins on gold substrate,[54] and microfibrillated cellulose on polyelectrolytes.[41, 42] Figure 5.5 compares the areal mass estimated with Johannsmann model after four deposition cycles for NC-PDDA-HMWL and NC-PDDA-OL systems. The values of the mass adsorbed per cycle and the mass of NC and lignin per cycle are given in Table 5.1 and 5.2, respectively. From the comparison, it is seen that the total mass adsorbed after four adsorption cycles is similar for both NC-PDDA-HMWL and NC-PDDA-OL (29.38 ± 2.57 and 31.78 ± 2.44 $mg.m^{-2}$, respectively). From the four adsorption cycles studied, the mass of lignin adsorbed in the first two cycles was

seen to differ between the two systems. The mass of HMWL adsorbed in adsorption cycles 1 and 2 were almost twice that of OL (Table 5.2). However, the mass of the two different lignins adsorbed in cycles 3 and 4 were similar. The mass of NC adsorbed in both systems was similar except for the 2nd cycle, where the mass of NC adsorbed in NC-PDDA-OL was slightly higher than NC-PDDA-HMWL. This difference caused the beginning of the third cycle to have the same amount of total mass for the two systems. These results suggest that after the initial cycles there is little difference in assembly for the type of lignin in the composite films. The mass of PDDA adsorbed was not estimated in this study because of the negligible or negative change after the adsorption of PDDA (Figure 5.5). As discussed earlier, this could be attributed to a combination of adsorption of PDDA as well as the simultaneous desorption of lignin/NC in the underlying layer.

**Table 5. 1** Areal mass estimated from QCM-D data using Johannsmann model for four deposition cycles.

| Cycle # | Mass per cycle ($mg.m^{-2}$) | | Cumulative mass ($mg.m^{-2}$) | |
|---|---|---|---|---|
| | NC-PDDA-HMWL | NC-PDDA-OL | NC-PDDA-HMWL | NC-PDDA-OL |
| 1 | 6.72 ± 0.80 | 5.51 ± 0.63 | 6.72 ± 0.79 | 5.51 ± 0.63 |
| 2 | 5.03 ± 0.22 | 5.82 ± 0.50 | 11.76 ± 0.77 | 11.33 ± 0.45 |
| 3 | 7.37 ± 0.37 | 7.52 ± 0.66 | 19.14 ± 0.98 | 19.52 ± 0.73 |
| 4 | 10.23 ± 1.97 | 12.92 ± 1.93 | 29.38 ± 2.57 | 31.78 ± 2.44 |

**Table 5. 2** Areal mass estimate of lignin and NC using Johannsmann model for four deposition cycles.

| Cycle # | Lignin ($mg.m^{-2}$) | | Nanocellulose ($mg.m^{-2}$) | |
|---|---|---|---|---|
| | NC-PDDA-HMWL | NC-PDDA-OL | NC-PDDA-HMWL | NC-PDDA-OL |
| 1 | 3.16 ± 0.26 | 1.56 ± 0.57 | 1.11 ± 0.13 | 1.15 ± 0.09 |
| 2 | 2.91 ± 0.32 | 1.30 ± 0.13 | 2.08 ± 0.36 | 3.18 ± 0.66 |
| 3 | 3.31 ± 0.39 | 3.77 ± 0.14 | 4.00 ± 0.38 | 3.22 ± 1.51 |
| 4 | 4.72 ± 0.64 | 4.22 ± 1.34 | 5.44 ± 1.78 | 5.46 ± 1.79 |

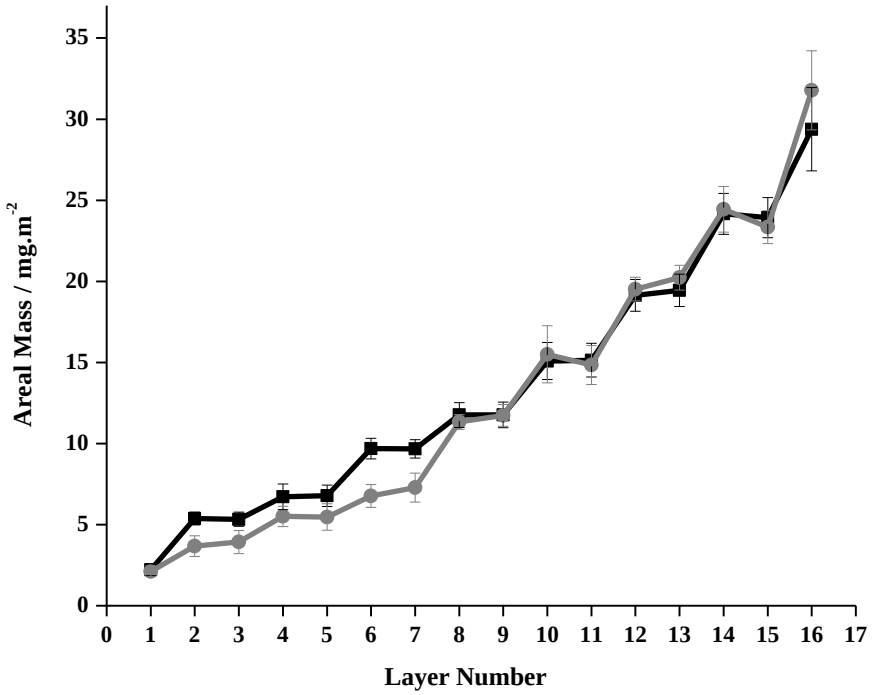


**Figure 5. 5** Areal mass estimated with Johannsmann model for NC-PDDA-HMWL (■) and NC-PDDA-OL (●) after four deposition cycles.

### *5. 4. 3. 2 Thickness Estimate*

The equations derived by Voinova et al., based on the Kelvin-Voigt model have been used in several studies to determine the viscoelastic properties, and thickness estimates.[52, 55-57] The ΔF from overtones n = 7, 9, and 11 were fit with the Q-tools software (Q-Sense Inc.) based on the equations of Voinova et al. (Figure 5.6). A comparison of the modeled data after four deposition cycles of NC-PDDA-HMWL and NC-PDDA-OL (Figure 5.7 and Table 5.3) revealed similar trends observed with the Johannsmann model. The first trend is the similarity of the final thicknesses between the films with two lignin types for a given film density boundary. The final thicknesses after four deposition cycles for NC-PDDA-HMWL and NC-PDDA-OL with an assumed density of 1000 $kg.m^{-2}$ were 31.5 ± 3.5 and 30.4 ± 5.1 nm respectively. The final thicknesses for the same, with an assumed

density of 1400 kg.m$^{-2}$, were 23.4 ± 2.8 and 22.1 ± 3.1 nm respectively. The second trend is revealed at the beginning of the third cycle where the change in thickness is the same for the two lignins, as found for the mass estimate. These changes suggest that a reduction of the effects of the surface occurs as film layers are deposited (as seen in the AFM images below). The thickness of the PDDA layer was not estimated because of negligible or negative changes in the thickness after the adsorption of PDDA. However, it was observed that significant sequential layer build-up was not possible without the adsorption of PDDA following the adsorption of NC or lignin.

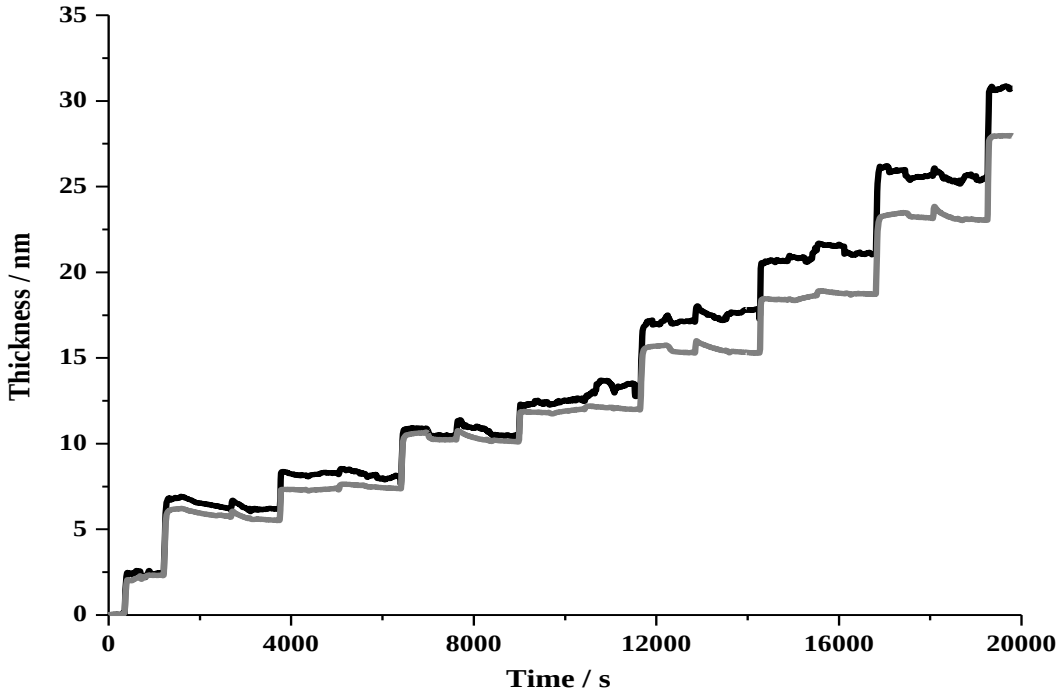


**Figure 5. 6** Thickness estimated with Voigt model (black) compared to the thickness estimated with Sauerbrey equation (7$^{th}$ harmonic; grey). The density of the film was assumed to be 1000 kg.m$^{-2}$.

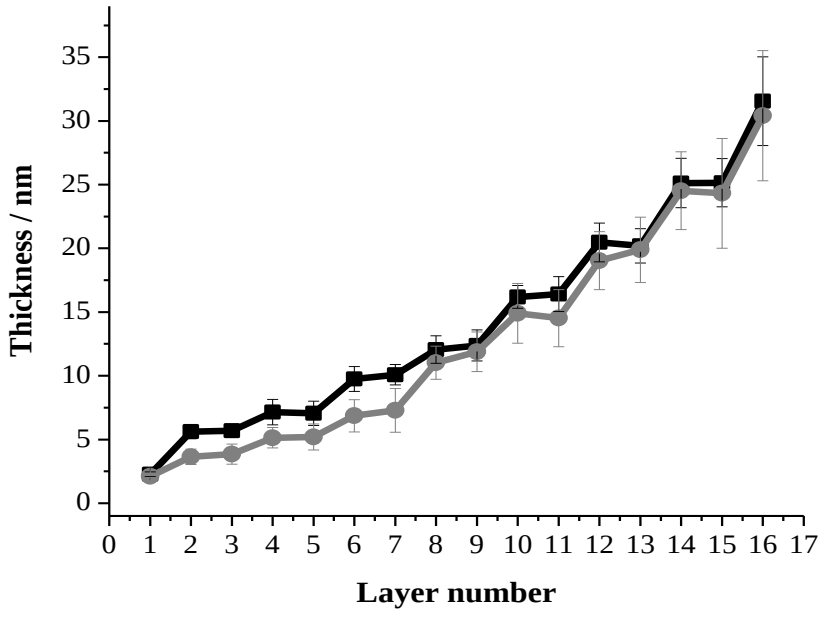


**Figure 5. 7** Comparison of thickness estimated with Voigt model for NC-PDDA-HMWL (■) and NC-PDDA-OL (●) after four deposition cycles with an assumed density of 1000 $kg.m^{-2}$.

### 5. 4. 4 Ellipsometry

The thickness of the nanocellulose and lignin films estimated using the viscoelastic model has been compared to ellipsometry thickness in Table 5.3. The ellipsometry thickness values from the first deposition cycle gave a close estimate to the Voigt model thickness, with an assumed density of 1000 $kg.m^{-2}$. The ellipsometry thickness value of the first cycle is almost 2-3 times larger than the $2^{nd}$, $3^{rd}$ and $4^{th}$ cycles. This phenomenon is related to the differences in PDDA deposition in the first cycle relative to the other cycles. From the QCM-D experiments, the initial PDDA layer on gold is found to be ~ 2 nm thick. However there was negligible or negative change in mass/thickness when PDDA was introduced over NC or lignin. A similar response was seen in a previous

study involving LbL adsorption of kraft lignin and PDDA, where a linear build up of film thickness was observed even though there was negligible PDDA adsorption.[50] The lower ellipsometry thickness values of the 2$^{nd}$ through 4$^{th}$ deposition cycles compared to the 1$^{st}$ cycle can be attributed to this thicker initial PDDA layer when deposited on gold, as PDDA has a different conformation in the subsequent steps. However, this relatively small adsorption of PDDA is seen to be sufficient to continue the LbL assembly process. There is significant difference between the ellipsometry and QCM-D thickness in the 3$^{rd}$ and 4$^{th}$ cycles, as the estimated Voigt thickness (based on a density of 1000 kg.m$^{-2}$). The thickness from the QCM-D data was found to be two times that of the ellipsometry thickness for both NC-PDDA-HMWL and NC-PDDA-OL systems. This result relative to the QCM-D data further implicates a hydrated nature of the films as the layer build-up proceeds. It is suggested that the topmost layers are more porous compared to the lower layers and hence hold more trapped water. Moreover, NC used in this study has carboxyl groups at the C6 position (carboxyl content of 1.0 mmol/g of cellulose), which makes the fibers more hydrophilic. The anionic groups attached to NC leads to the layer being viscous, hence the deviation from the Sauerbrey relation, which is applicable only for thin and elastic films. To verify the validity of the dry film thickness estimated by ellipsometry, an AFM scratch test was performed on both NC-PDDA-HMWL and NC-PDDA-OL after four deposition cycles on a Si wafer. The height profile (Appendix A 5-3) from the scratch test gave an average thickness of 15.1 ± 0.9 nm and 17.3 ± 3.0 nm respectively for NC-PDDA-HMWL and NC-PDDA-OL. These values are close to those estimated by ellipsometry (Table 5. 3).

**Table 5. 3** Cumulative thickness after each adsorption cycle estimated by Voigt model, with assumed densities of 1000 and 1400 kg.m$^{-3}$, and thickness estimated by ellipsometry for four deposition cycles.

| Cycle # | NC-PDDA-HMWL (nm) | | | NC-PDDA-OL (nm) | | |
|---|---|---|---|---|---|---|
| | Voigt (1000 kg.m$^{-2}$) | Voigt (1400 kg.m$^{-2}$) | Ellipsometry | Voigt (1000 kg.m$^{-2}$) | Voigt (1400 kg.m$^{-2}$) | Ellipsometry |
| 1 | 7.2 ± 1.0 | 5.0 ± 0.4 | 7.5 ± 0.3 | 5.1 ± 1.0 | 4.0 ± 0.5 | 6.1 ± 0.1 |
| 2 | 12.0 ± 1.1 | 8.8 ± 1.0 | 10.4 ± 0.6 | 11.0 ± 1.3 | 8.0 ± 0.7 | 8.1 ± 0.3 |
| 3 | 20.5 ± 1.5 | 14.4 ± 1.1 | 12.0 ± 0.3 | 19.0 ± 2.3 | 13.2 ± 1.3 | 11.7 ± 0.1 |
| 4 | 31.5 ± 3.5 | 23.4 ± 2.8 | 14.5 ± 0.3 | 30.4 ± 5.1 | 22.1 ± 3.1 | 13.8 ± 0.5 |

### 5. 4. 5 Atomic Force Microscopy

AFM images revealed complete coverage of the surface with lignin in the first PDDA-lignin bilayer (Figure 5. 8-a & 5. 8-b). The root mean square (rms) roughness values for HMWL and OL were 1.6 and 3.8 nm respectively. AFM images of the first PDDA-NC bilayer showed that the surface was not completely covered with NC fibrils, with minimum overlap of NC fibrils in the 2.5 x 2.5 μm images (Figure 5.9-a & 5.9-b, rms roughness 1.6 nm). However, as the layer build-up continued, more uniformity was found for the fibrils deposited, as seen in Figure 5.9-b (RMS roughness 5.3 nm). Similar results were seen with QCM-D data, as ΔF for NC changed greater in magnitude at higher cycle number. The adsorbed mass estimated using Johannsmann model for the 1$^{st}$ and 4$^{th}$ cycle of NC layer in NC-PDDA-HMWL system was 1.11 ± 0.13 mg.m$^{-2}$ and 5.44 ± 1.78 mg.m$^{-2}$ respectively. A similar trend was also observed with the NC-PDDA-OL system with an estimated NC mass of 1.15 ± 0.09 and 5.46 ± 1.79 mg.m$^{-2}$ for the 1$^{st}$ and 4$^{th}$ cycles respectively. These estimates suggest that the hydrated mass of NC layer deposited in the 4$^{th}$ deposition cycle is 4 times greater than that of the 1$^{st}$ deposition cycle. The increase in mass associated with NC adsorption can also be attributed to the water entrained in the porous structure created by the fibers. An increase in the amount of trapped water, with

the increase in layer thickness has been reported in systems involving MFC multilayers.[41, 58] AFM images revealed the lignin is deposited along the NC, as seen in the higher magnification images after 3 cycles (Figure 5. 10-a & 10-b).

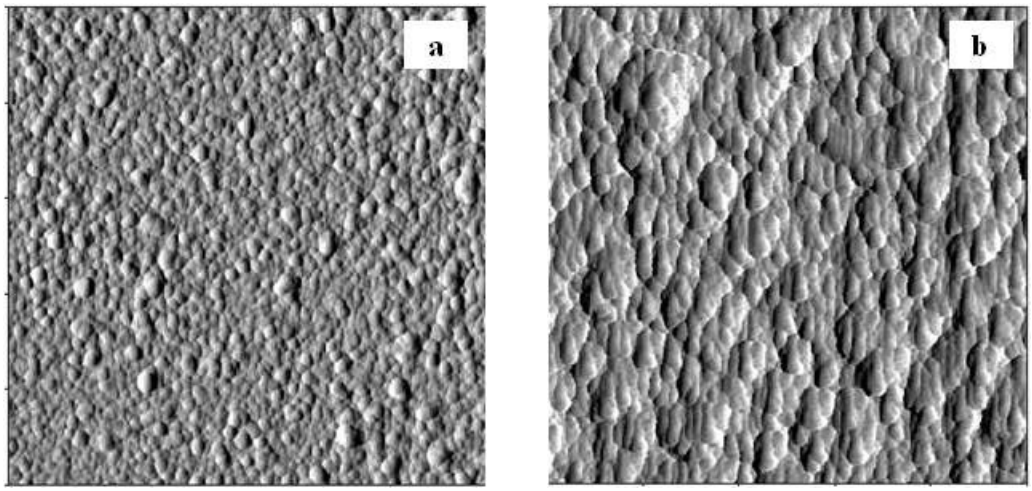


**Figure 5. 8 a&b**. AFM Amplitude images (2.5 x 2.5 µm) of MWL (a; z-scale = 2 nm) and OL (b; z-scale = 8 nm) after the deposition of the 1st bilayer (PDDA:Lignin).

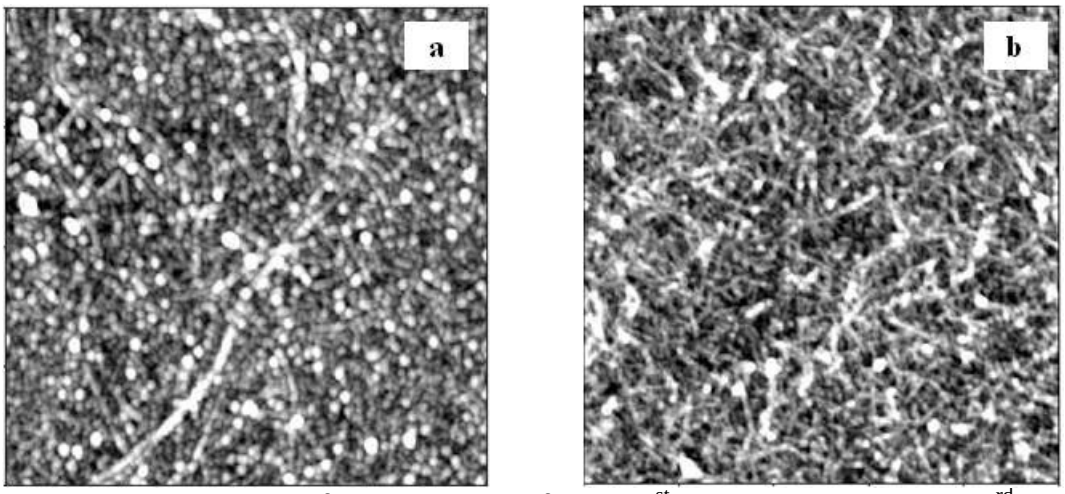


**Figure 5. 9** Height images of NC on PDDA after the 1st (a; z-scale = 3 nm) and 3rd (b; z-scale = 6 nm) deposition cycle (2.5 x 2.5 µm).

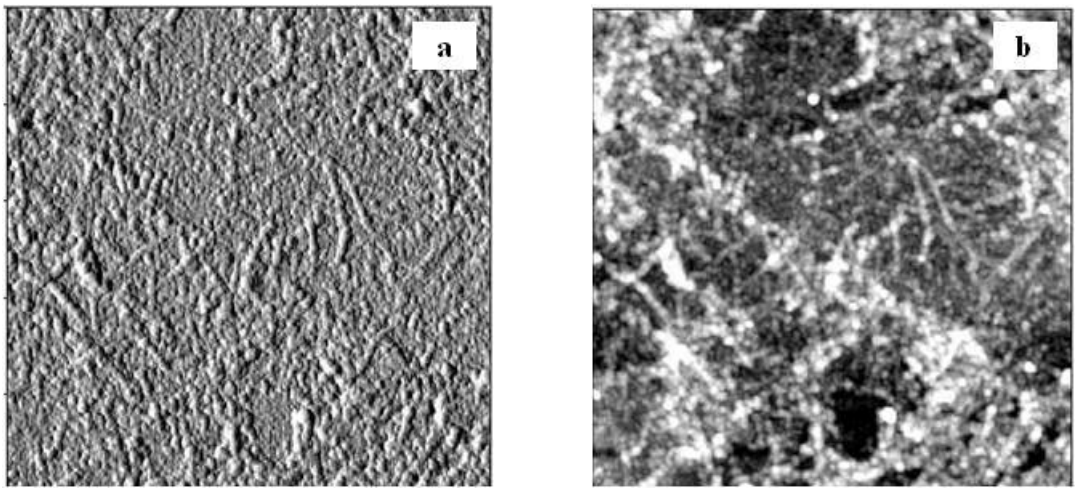


**Figure 5. 10** Amplitude (a; z-scale = 2 nm) and height images (b; z-scale = 6 nm) of HMWL after the 4th deposition cycle (2.5 x 2.5 µm). The images show lignin particles deposited on the NC fibrils from the 3rd deposition cycle.

### 5. 4. 6 Free-standing LbL Films

Free-standing LbL films were obtained after 250 deposition cycles, when the cellulose acetate substrate was dissolved in acetone (Figure 5. 11). Initial observation of the film was that it was translucent and bendable. These two properties are rarely associated with lignin-based composites that contained a significant lignin loading. SEM of the cryo-fractured cross-sections of LbL films displays a lamellar structure (Figure 5.12). The thickness of both NC-PDDA-HMWL and NC-PDDA-OL were found to be approximately 4.3 µm, which implies an average thickness of approximately 17 nm per deposition cycle. The SEM data indicates a significantly higher thickness compared to QCM-D and ellipsometry estimates. However, the QCM-D and ellipsometry measurements were carried out for only 4 deposition cycles (reaching the limits of the instrument due to the viscoelastic surface). From the QCM-D results, it was noted that the layer build-up was not linear for the four deposition cycles studied. Therefore it is

possible that it takes more than 4 deposition cycles for the thickness increase per cycle to plateau, and have a linear build-up of layers.

**Figure 5. 11** A free-standing film of NC-PDDA-HMWL obtained after 250 deposition cycles. The free-standing films were obtained after dissolving the cellulose acetate substrate in acetone.

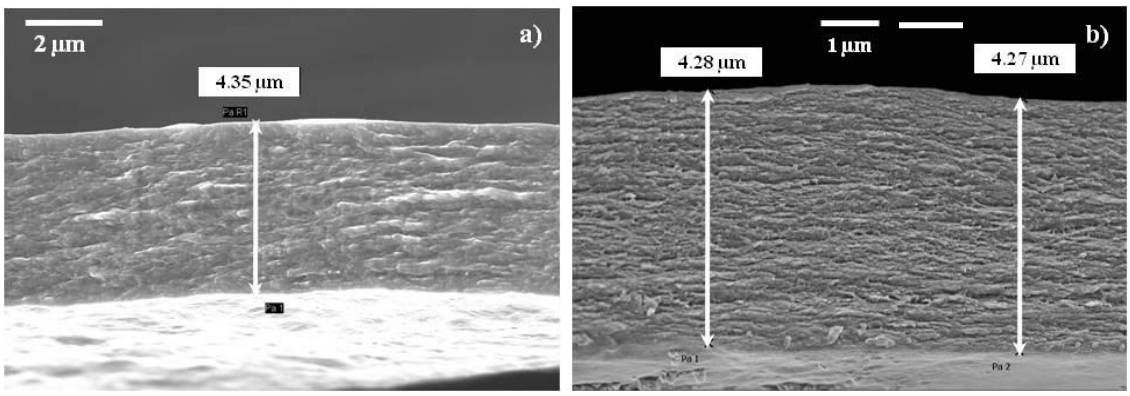


**Figure 5. 12** SEM images showing lamellar structure of the cross-sections of cryo-fractured LbL films after 250 deposition cycles. The free standing films of a) NC-PDDA-HMWL and b) NC-PPDA-OL were obtained after the cellulose acetate substrate was dissolved in acetone.

## 5. 5 Conclusions

QCM-D and ellipsometry studies showed that LbL technique can be used to sequentially deposit isolated wood polymers NC and lignin to build-up lignocellulosic multilayers, in combination with cationic PDDA. Two different types of lignins, OL and HMWL were

used in this study and found to show similar viscoelastic modeled mass and thickness after four deposition cycles; however, there were differences in the first two deposition cycles. The thickness estimated by ellipsometry was similar to the Voigt model thickness (with an assumed density of 1000 $kg.m^{-2}$) for the first deposition cycle. However, these values were found to significantly vary in the 3rd and 4th deposition cycles, which can be attributed to the increase in trapped water and viscoelastic nature of the films. AFM images showed complete coverage of the PDDA surface with lignin in all the deposition cycles. In contrast to lignin, only scattered fibrils of NC were observed in the first cycle. However, more fibers were deposited and uniform coverage was observed as layer build-up continued. A similar trend was observed with the QCM-D results, as the mass of NC adsorbed in the 4th deposition cycle was almost 4 times the mass in 1st cycle. Free-standing LbL films were obtained after 250 deposition cycles, when the cellulose acetate substrate on which the film was deposited was dissolved in acetone. Cryo-fractured cross-sectional images of the films display a lamellar structure, and based on the thickness, the average thickness per deposition cycle was estimated to be approximately 17 nm per cycle. Comparison of two dissimilar lignin types indicated that the lignin chemistry does not have a significant role in the build-up of free standing films.

## 5. 6 References


1. Fratzl, P.; Burgert, I.; Gupta, H. S. *Phys. Chem. Chem. Phys.* **2004**, *6*, 5575-5579.
2. Baer, E.; Hiltner, A.; Morgan, J. R. *Phys. Today* **1992**, *45*(10), 60-67.
3. NAS, *Heirarchical structures in biology as a guide for new materials technology*. National Academy Press: Washington DC, 1994.
4. Fengel, D., Wegener, G., *Wood: Chemistry, Ultrastructure, Reactions*. Walter de Gruyter: Berlin, New York, 1984.

5. Terashima, N.; Fukushima, K.; He, L. F.; Takabe, K. In *Forage cell wall structure and digestibity*, Jung, H. G.; Buxton, D. R.; Hatfield, R. D.; Ralph, J., Eds. American Society of Agronomy: Madison, USA, 1993; pp 247-270.

6. Himmel, M. E.; Ding, S.-Y.; Johnson, D. K.; Adney, W. S.; Nimlos, M. R.; Brady, J. W.; Foust, T. D. *Science* **2007**, *315*, 804-807.

7. Terashima, N.; Kitano, K.; Kojima, M.; Yoshida, M.; Yamamoto, H.; Westermark, U. *J. Wood Sci*. **2009**, *55*, 409-416.

8. Fahlén, J.; Salmén, L. *Biomacromolecules* **2005**, *6*, 433-438.

9. Kojima, Y.; Usuki, A.; Kawasumi, M.; Okada, A.; Fukushima, Y.; Kurauchi, T.; Kamigaito, O. *J. Mater. Res*. **1993**, *8*, 1185-1189.

10. Favier, V.; Canova, G. R.; Cavaillé, J. Y.; Chanzy, H.; Dufresne, A.; Gauthier, C. *Polym. Advan. Technol*. **1995**, *6*, 351-355.

11. Favier, V.; Chanzy, H.; Cavaillé, J. Y. *Macromolecules* **1995,** *28*, 6365-6367.

12. Sturcova, A.; Davies, G. R.; Eichhorn, S. J. *Biomacromolecules* **2005,** *6*, 1055-1061.

13. Sheng, N.; Boyce, M. C.; Parks, D. M.; Rutledge, G. C.; Abes, J. I.; Cohen, R. E. *Polymer* **2004**, *45*, 487-506.

14. Treacy, M. M. J.; Ebbesen, T. W.; Gibson, J. M., Exceptionally high Young's modulus observed for individual carbon nanotubes. *Nature* **1996**, *381*, 678-680.

15. Rusli, R.; Eichhorn, S. J. *Appl. Phys. Lett*. **2008**, *93*, 033111-3.

16. Decher, G.; Hong, J. D. *Berich. Bunsen. Phys. Chem*. **1991**, *95*, 1430-1434.

17. Decher, G. *Science* **1997**, *277*, 1232-1237.

18. Hammond, P. T. *Adv. Mater*. **2004**, *16*, 1271-1293.

19. Decher, G.; Schlenoff, J. B., *Multilayer thin films: sequential assembly of nanocomposite materials*. Wiley-VCH: Weinheim, 2002.

20. Mamedov, A. A.; Kotov, N. A. *Langmuir* **2000**, *16*, 5530-5533.

21. Mamedov, A. A.; Kotov, N. A.; Prato, M.; Guldi, D. M.; Wicksted, J. P.; Hirsch, A. *Nat. Mater*. **2002**, *1*, 257-257.

22. Podsiadlo, P.; Liu, Z.; Paterson, D.; Messersmith, P. B.; Kotov, N. A. *Adv. Mater*. **2007**, *19*, 949-955.

23. Podsiadlo, P.; Kaushik, A. K.; Arruda, E. M.; Waas, A. M.; Shim, B. S.; Xu, J.; Nandivada, H.; Pumplin, B. G.; Lahann, J.; Ramamoorthy, A.; Kotov, N. A. *Science* **2007**, *318*, 80-83.

24. Podsiadlo, P.; Kaushik, A. K.; Shim, B. S.; Agarwal, A.; Tang, Z.; Waas, A. M.; Arruda, E. M.; Kotov, N. A. *J. Phys. Chem. B* **2008**, *112*, 14359-14363.

25. Becker, A. L.; Johnston, A. P. R.; Caruso, F. *Small* **2010**, *6*,1836-1852.

26. Taylor, A. D.; Michel, M.; Sekol, R. C.; Kizuka, J. M.; Kotov, N. A.; Thompson, L. T. *Advan. Funct. Mater.* **2008**, *18*, 3003-3009.

27. Ashcraft, J. N.; Argun, A. A.; Hammond, P. T. *J. Mater. Chem.* **2010**, *20*, 6250-6257.

28. Lee, S. W.; Yabuuchi, N.; Gallant, B. M.; Chen, S.; Kim, B.-S.; Hammond, P. T.; Shao-Horn, Y. *Nat. Nano* **2010**, *5*, 531-537.

29. Eriksson, M.; Notley, S. M.; Wågberg, L., *J. Coll. Interf. Sci.* **2005**, *292*, 38-45.

30. Lvov, Y. M.; Grozdits, G. A.; Eadula, S.; Zheng, Z.; Lu, Z. *Nord. Pulp Pap. Res. J.* **2006**, *21*, 552-557.

31. Lin, Z.; Renneckar, S.; Hindman, D. *Cellulose* **2008**, *15*, 333-346.

32. Cranston, E. D.; Gray, D. G.; Barrett, C. J. In *Abstracts of 32nd Northeast Regional Meeting of the American Chemical Society* 2004; Rochester, NY, 2004.

33. Podsiadlo, P.; Choi, S.-Y.; Shim, B.; Lee, J.; Cuddihy, M.; Kotov, N. A. *Biomacromolecules* **2005**, *6*, 2914-2918.

34. Cranston, E. D.; Gray, D. G. *Sci. Technol. Adv. Mater.* **2006**, *7*, 319-321.

35. Cranston, E. D.; Gray, D. G. *Biomacromolecules* **2006**, *7*, 2522-2530.

36. Jean, B.; Dubreuil, F.; Heux, L.; Cousin, F., *Langmuir* **2008**, *24*, 3452-3458.

37. Podsiadlo, P.; Sui, L.; Elkasabi, Y.; Burgardt, P.; Lee, J.; Miryala, A.; Kusumaatmaja, W.; Carman, M. R.; Shtein, M.; Kieffer, J.; Lahann, J.; Kotov, N. A. *Langmuir* **2007**, 23, 7901-7906.

38. Jean, B.; Heux, L.; Dubreuil, F.; Chambat, G.; Cousin, F. *Langmuir* **2009**, *25*, 3920-3923.

39. de Mesquita, J. P.; Donnici, C. L.; Pereira, F. V. *Biomacromolecules* **2010**, *11*, 473-480.

40. Wågberg, L.; Decher, G.; Norgren, M.; Lindström, T.; Ankerfors, M.; Axnas, K. *Langmuir* **2008,** *24*, 784-795.

41. Aulin, C.; Varga, I.; Claesson, P. M.; Wågberg, L.; Lindström, T. *Langmuir* **2008**, *24*, 2509-2518.

42. Aulin, C.; Johansson, E.; Wågberg, L.; Lindström, T. *Biomacromolecules* **2010**, *11*, 872-882.

43. Samir, M. A. S. A.; Alloin, F.; Dufresne, A. *Biomacromolecules* **2005**, *6*, 612-626.

44. Siró, I.; Plackett, D. *Cellulose* **2010**, *17*, 459-494.

45. Teeri, T. T.; Brumer III, H.; Daniel, G.; Gatenholm, P. *Trends Biotechnol*. **2007**, *25*, 299-306.

46. Glasser, W. G.; Barnett, C. A.; Sano, Y. In *Proceedings of the ninth cellulose conference*; Sarko, A., Ed. John Wiley and Sons: Syracuse, NY, 1982; pp 441-460.

47. Saito, T.; Nishiyama, Y.; Putaux, J.-L.; Vignon, M.; Isogai, A. *Biomacromolecules* **2006**, *7*, 1687-1691.

48. Li, Q.; Renneckar, S. *Cellulose* **2009**, *16*, 1025-1032.

49. Notley, S. M.; Norgren, M. *Biomacromolecules* **2008**, *9*, 2081-2086.

50. Pillai, K. V.; Renneckar, S. *Biomacromolecules* **2009**, *10*, 798-804.

51. Aulin, C.; Varga, I.; Claesson, P. M.; Wagberg, L.; Lindstrom, T. *Langmuir* **2008**, *24*, 2509-2518.

52. Höök, F.; Kasemo, B.; Nylander, T.; Fant, C.; Sott, K.; Elwing, H. *Anal*. *Chem*. **2001**, *73*, 5796-5804.

53. Naderi, A.; Claesson, P. M. *Langmuir* **2006**, *22*, 7639-7645.

54. Kaufman, E. D.; Belyea, J.; Johnson, M. C.; Nicholson, Z. M.; Ricks, J. L.; Shah, P. K.; Bayless, M.; Pettersson, T.; Feldotö, Z.; Blomberg, E.; Claesson, P.; Franzen, S. *Langmuir* **2007,** *23*, 6053-6062.

55. Garg, A.; Heflin, J. R.; Gibson, H. W.; Davis, R. M., *Langmuir* **2008,** *24*, 10887-10894.

56. Gurdak, E.; Dupont-Gillain, C. C.; Booth, J.; Roberts, C. J.; Rouxhet, P. G. *Langmuir* **2005**, *21*, 10684-10692.

57. Vogt, B. D.; Lin, E. K.; Wu, W.-l.; White, C. C. *J. Phys*. *Chem*. *B* **2004**, *108*, 12685-12690.

58. Argun, A. A.; Ashcraft, N. J.; Hammond, P. T. *Advan*. *Mater*. **2008**, *20*, 1539-1543.

59. Van de Steeg, H. G. M.; Cohen Stuart, M. A.; De Keizer, A.; Bijsterbosch, B. H. *Langmuir* **1992**, *8*, 2538-2546.

# Chapter 6. Preparation and Characterization of Novel Lignocellulosic Nanocomposites

## 6. 1 Abstract

Natural composites like wood are scale integrated structures that range from molecular to the macroscopic scale. Inspired by this design, layer-by-layer (LbL) deposition technique was used to create lignocellulosic composites from isolated wood polymers with an ordered architecture. The objective of this study was to investigate the effect of the LbL ordering versus a cast film composed of a blended mixture of the same polymers using DMA. The composites were made from nanocellulose (NC) obtained by fibrillation of oxidized pulp fibers, organosolv lignin (OL), and a cationic polyelectrolyte poly(diallyldimethylammonium chloride) (PDDA). DMA was done on thin films that were saturated with ethylene glycol, utilizing a parallel-plate compression-torsion technique. In the temperature range that was studied (0 – 120 ºC), a single tan δ peak was observed in the 30 – 40 ºC region for both LbL and cast films. A neat NC cast film was tested under similar conditions that displayed a similar relaxation in this region. The peak was seen to disappear in case of LbL films in the second heat, whereas it was recurring in case of cast films of the blended mixture, and neat NC films. Heating of the samples under a compressive force produced an opposite effects in the two films, as the LbL films exhibited swelling, whereas the cast films showed densification. Also, the tan δ peak in the second heat of cast films was found to be frequency dependent. The apparent

activation energies calculated (65 – 80 kJ $mol^{-1}$) for these film based on the Arrhenius equation was found to be coincident to those reported for the $\beta$ transition of cellulose.

## 6. 2 Introduction

Natural materials like wood, bone, and nacre have very complex structures, and their building blocks are organized hierarchically over several length scales, which offers a synergistic effect compared to their individual properties, or properties of their simple mixtures.[1, 2] The secondary cell wall of plants is primarily composed of three different types of macromolecules namely cellulose, hemicelluloses and lignin, which exist as a complex, organized network that act cooperatively to external stresses.[3] The secondary cell wall can be considered a nanocomposite, wherein cellulose microfibrils acts as the reinforcement, and is embedded in a matrix of lignin and hemicelluloses.[4] However, it is also interesting to note that the properties of these polymers when isolated from these complex structures do not often reflect their native function. [5]

Synthetic nanocomposites are materials prepared by the addition of nano-fillers/nanoparticles in the polymer matrix, which results in significant improvements in the mechanical and thermal properties of the composite.[6,7] The use of cellulose based nanoparticles obtained by acid hydrolysis (cellulose whiskers), and high-pressure homogenization (microfibrillated cellulose) as nano-fillers in bio-based and synthetic polymer matrices has received much interest. [8, 98,9] Another method for preparing nanoscale celluloses with length scales similar to carbon nanotubes was developed, when TEMPO mediated oxidized pulp fibers were fibrillated by mechanical agitation or ultrasonication.[10-13] However, the use of these nanoparticles was not associated with

expected results, considering the exceptional mechanical properties of the individual nanoparticles.[14, 15] This result has largely been attributed to poor dispersion and inadequate interfacial interaction between the matrix and reinforcement.[16-18] In this context, the concept of layer-by-layer (LbL) adsorption offers a significant advantage in the ability to immobilize polymers/nanoparticles through electrostatic interactions in exact architectures[19]. The technique has been used to create free-standing films composed of polymers and nanoparticles, which were aimed at several potential applications.[20-24]

This study involves the preparation of nanocomposites from isolated wood polymers, namely nanocellulose and lignin, in combination with a positively charged polyelectrolyte PDDA that facilitates assembly. Composites were prepared using two strategies, one a LbL assembly for free-standing films, and the other, a cast film of the blended mixture. The study is motivated by the biomimetic approach to engineer the organization of the isolated polymers in a nanocomposite material, and to compare it with the composite made of the same material as a simple mixture. The prepared films were compared using a novel dynamic mechanical analysis technique, which enables the analysis of thin films in an organic solvent plasticized condition.

## 6. 3 Materials and Methods

The lignin used in this study was organosolv lignin (OL; Sigma Aldrich, Inc). Nanocellulose (NC) was produced from never dried sulfate pulp (brightness level of 88%), supplied by Weyerhaeuser Inc. The cationic polymer used in this study was PDDA (Sigma Aldrich: $M_n = 7.2\times10^4$, $M_w = 2.4\times10^5$ g/mol).

### 6. 3. 1 TEMPO-mediated Oxidation and Fibrillation of Pulp Fibers

TEMPO oxidation of never-dried kraft pulp was carried out using the method described by Saito et al.[10] with slight modification. Briefly, the pulp (20 g, 1% w/v, dry weight basis) was mixed with TEMPO (0.313 g, 0.1 mmol) and NaBr (2.0 g, 1 mmol) in a 3 L three-neck flask until the fibers were well dispersed in 2.0 L of water (milli-Q, 18.5 MΩ.cm). The oxidation was initiated by slowly adding a 12% solution of NaOCl (64.7 ml, 5 mmol/g of cellulose) to the reaction mixture, while maintaining the pH of the mixture at 10 by adding 0.5 M NaOH. The reaction was stopped when no further addition of NaOH was required to maintain the pH. The oxidized fibers were thoroughly washed with Milli-Q water to remove the reagents and stored at 4 °C for further use. The carboxyl content of the oxidized pulp was determined by conductometric titration. A 3 % (w/v, dry weight basis) slurry of the TEMPO oxidized pulp was beaten in a Warring blender until the slurry became viscous and the blades started spinning in the air. The blended slurry was diluted to 0.1% (w/v) and nanofibrillated by ultrasonication with a Sonics® ultrasonic processor (Model GE 505) for 15 min (100 % power). The ultrasonicated samples were centrifuged at 5000 rpm for 5 min and the transparent supernatant containing the fibrillated nanocellulose fraction was decanted, freeze dried and stored for further use. Past experiments have shown that these fibrils have lengths of 530 ± 330 nm and thickness of 1.4 ± 0.7 nm.[12]

### 6. 3. 2 Preparation of LbL Free-standing Films

Deposition of LbL films were carried out on a cellulose acetate substrate using a custom made spraying device.[25] The layers were deposited in the following sequence; 1) 0.2% (w/v) PDDA (pH 10.5), 2) DI water (10 s), 3) 0.01% (w/v) OL (pH 10.5), 4) DI water, 5)

0.5% (w/v) PDDA (pH 10.5), 6) DI water, 7) 0.1% (w/v) NC, 8) DI water. Steps 1 through 8 represents one deposition cycle with two bilayers (PDDA:OL and PDDA:NC). The spraying time was 4 s for polymer solutions and 10 s for rinse step with DI water. A dwell time of 20 s was used between each step. Therefore the total time required for one deposition cycle was 3 min 16 s. A total of 250 cycles/500 bilayers were deposited to obtain a free-standing film, which required a total spraying time of ~ 13.5 Hrs. Once the deposition was complete, the films were air-dried and extracted by dissolving the CA substrate in acetone. The extracted LbL films were soaked in acetone for 24 hours and further washed 5 times in fresh acetone bath to facilitate the maximum removal of residual CA. The extracted films were then air-dried and stored until further use.

### 6. 3. 3 Preparation of Solvent Cast Films

Batches of 0.2 % (w/v) NC suspension was prepared by re-dispersing 0.5 g freeze dried NC in 250 ml Mill-Q water aided by ultra-sonication (100 % power) for 15 min in a water bath (4 ºC). The sonicated suspension was centrifuged at 5000 rpm for 5 min, and the supernatant was collected. No residues were present after centrifugation, which suggests that the starting material was completely dispersed in water.

#### *6. 3. 3. 1 Preparation of Blended Films of NC, OL and PDDA*

2 gm of NaOH (0.2 N) was dissolved in 250 ml of NC suspension (0.2 % w/v), followed by the addition of 0.35 g OL. The suspension was allowed to mix for 24 hrs with continuous stirring. Following this step, 0.15 g of PDDA (10 ml of 1% w/v) was added slowly and was mixed with continuous stirring for 24 hrs. The relative proportions of NC, OL and PDDA in the mixture was thus 5 : 3.5 : 1.5. It was found during the preparation of blended films that PDDA is necessary to complex the three different materials (NC,

OL and PDDA). The absence of PDDA in preparation of blended films resulted in significant leaching of lignin to the solvent used for plasticizing the films. From our initial experiments, the minimum amount of PDDA required to prevent leaching of lignin from the film was found to be 15 % (w/w) of the total film. The mixture was dialyzed in a 12,000 – 14,000 g/mol molecular weight cut off dialysis tubes (Spectrum Labs) against Milli-Q water to remove the excess NaOH. The dialysis water was replaced every 12 hours until the conductivity of the Milli-Q water dropped to < 2.0 $\mu S.cm^{-1}$. The dialyzed mixture was concentrated with rotary evaporator (~ 1 % w/v), poured into poly-tetraflouroethylene (PTFE) dishes and dried at 50 ºC.

#### *6. 3. 3. 2 NC Cast Films*

To prepare cast films of NC, 250 ml of the 0.2% (w/w) NC suspension was prepared as described above. The suspension was concentrated in a rotovap (~ 0.5 % w/v), poured into PTFE dishes and dried in a hot air oven at 50 ºC.

### 6. 3. 4 SEM

Scanning electron micrographs of the cross-sections of the films were performed using a LEO (Zeiss) 1550 field emission scanning electron microscope. The cross-sections were prepared by cryo-fracturing of the films after dipping in liquid $N_2$.

### 6. 3. 5 DMA

All DMA experiments were carried out with a TA Instruments AR 2000 rheometer. The experiments were carried out in compression-torsion mode with an 8 mm diameter parallel plate attachment. The bottom plate was modified with a cup to enable experiments in solvent submersion mode.

#### *6. 3. 5. 1 DMA Sample Preparation*

Prior to DMA experiments, the samples were dried in a vacuum oven for 24 hrs at ambient temperature. The vacuum dried cast films of NC-OL-PDDA and NC were submerged in ethylene glycol (99.8 % grade) over anhydrous $P_2O_5$, over a period of 48 hrs. The solvent submersion method was chosen because the films had shown poor response in the dry state. The saturated films were placed between two PTFE sheets, and 8 mm discs were punched out. The use of PTFE sheets ensured uniformity, and prevented damage to the films. The 8mm diameter films were stacked (4-5 films) on the bottom plate and held in place by applying a normal compressive force (0.5 N) with the top plate. Owing to the low thickness and delicateness of the LbL films, these samples were punched out as 8 mm discs in the dry state by placing them between two PTFE sheets. Soaking of these films in ethylene glycol was carried out later during sample loading, as soaking them prior to sample loading made them difficult to handle. Before the first LbL film was placed, the bottom plate was wetted with a drop of ethylene glycol, which made it convenient to keep the thin film adhered to the plate. Only a visual estimate was done to see if the film was completely saturated. The procedure was repeated by placing one film on top of the other, wherein, between every couple of films a drop of ethylene glycol was added. The process was continued for 25-30 films when the thickness of the stack reached 200 - 250 µm after the application of a low normal compressive force (0.5 N). While running the tests, the cup attached to the bottom plate was filled with ethylene glycol, which kept the sample submerged at all times, and the assembly was covered with an Al lid to minimize evaporative losses during the experiment. The LbL film samples were equilibrated in the ethylene glycol bath for 1 hr at ambient temperature before the start of the experiment.

#### *6. 3. 5. 2 Determination of Linear Viscoelastic Limit*

Linear viscoelastic regions of the plasticized films were determined by carrying out stress sweep experiments at the lower and higher limit of the temperature range studied (0 – 120 ºC). All thermal scan experiments were carried out within the LVR limit. Measurements were carried out with separate samples dedicated for that purpose, and the lower temperature limit was always tested first. The LVR limit was determined from the linear stress vs. strain plot, when the least square fit of the plot gave an $r^2$ correlation coefficient ≥ 0.9995.

#### *6. 3. 5. 3 Normal Force Control – Frequency Sweep Experiments*

The stacked film samples were subject to a fixed compressive normal force of 5.0 ± 0.1 N throughout the experiment. To account for thickness change during the thermal scans, the gap change tolerance limit for the parallel plate assembly was set to be ± 500 µm in either direction. Temperature ramp – frequency sweeps were carried out as a heat-cool-heat experiment. Thermal scans were carried out in a range of 0 - 120 ºC at a rate of 1 $ºC.min^{-1}$ for both heating and cooling scans. It should be noted that the upper limit of 120 ºC, which is well below the boiling point of ethylene glycol (197.3 ºC), was chosen to avoid significant evaporation losses, and danger of flammability of the organic solvent upon contact with heating filaments of the furnace. For this reason, all experiments were carried out in an anhydrous $N_2$ atmosphere. Frequency sweeps were carried out in a range of 0.1 – 50.0 Hz, with a sampling of 3 points per decade in logarithmic scale. An oscillation stress of 5000 Pa was applied for all samples, as this value was found to be within the LVR limit for all three types of films. This stress value was also seen to produce smooth sine wave functions of the dynamic strain in response to the stress at

both the upper and lower temperature limits. The steps involved in the heat-cool-heat experiments are: 1) conditioning at 0 ºC for 1min, 2) heat from 0 – 120 ºC (1 ºC.min$^{-1}$), 3) conditioning at 120 ºC for 1min, 4) cool from 120 – 0 ºC (1 ºC.min$^{-1}$), 5) conditioning at 0 ºC for 1min, 6) heat from 0 – 120 ºC (1 ºC.min$^{-1}$).

## 6. 4 Results and Discussion

### 6. 4. 1 SEM

SEM cross-section images of cryo-fractured solvent cast film of NC-OL-PDDA (Figure 6.1) reveals a fractured surface that is relatively rough. Magnification of the cross section reveals a layered structure with some elements that appear as vertical joints between layers. The heterogeneous layered structure in the cast films arises as a result of the differential drying process, wherein the drying proceeds from the top to the bottom. In contrast to the solvent cast film, LbL (Figure 6.2) films show different morphology related to a smooth fractured surface and highly regular layered structures throughout the cross-section. This layered morphology arises from the sequential deposition of the layers and is consistent throughout the cross-section. It is interesting to note in the magnified view, there are discrete clusters decorating the elongated structures that run parallel to the surface. This motif is similar to AFM images shown previously (chapter 5) that had nanocellulose fibrils decorated with lignin aggregates. The thickness of the free-standing film after 250 deposition cycles was found to be approximately 4.3 µm, which suggests an average thickness per deposition cycle of 17 nm. The LbL films were found to be transparent and flexible, whereas the cast films of NC-OL-PDDA was found to be opaque and stiff.

a) b)

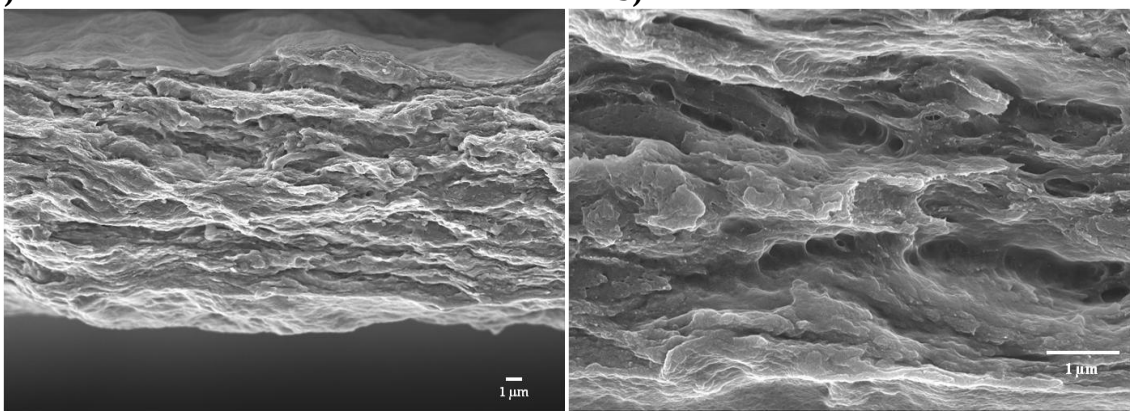


**Figure 6.1** SEM images of the cryo-fractured cross-sections of NC-OL-PDDA cast film. a) shows the complete cross-section, and b) shows a magnified image of the cross-section.

a) b)

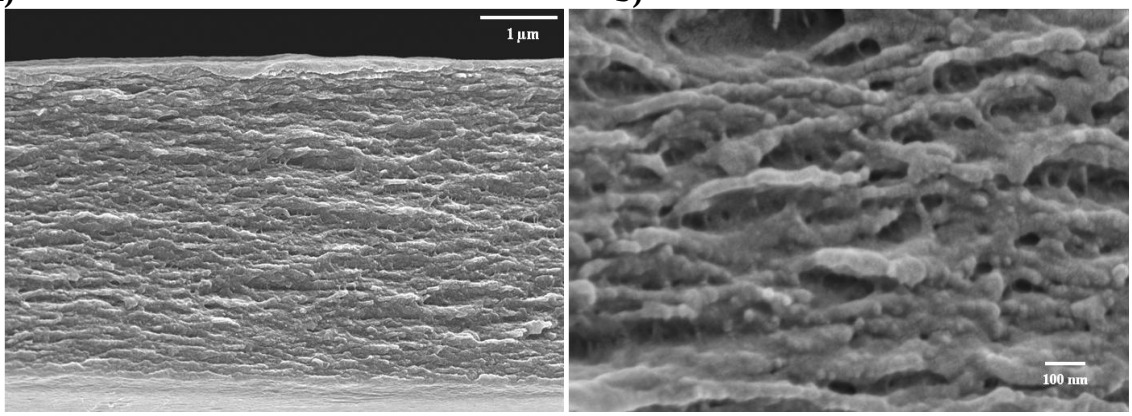


**Figure 6.2** SEM images of the cryo-fractured cross-sections of LbL. a) shows the complete cross-section, and b) shows a magnified image of the cross-section.

### 6. 4. 2 DMA

The storage modulus (G') of blended cast films NC-OL-PDDA (5 : 3.5 : 1.5) in normal force control, at 1 Hz is shown in Figure 6.3. The storage modulus of the ethylene glycol plasticized films was found to fall between $10^7$ – $10^8$ Pa. This relatively low storage modulus, compared to typical synthetic polymers and wood is due to the plasticization of the samples with ethylene glycol. The choice to use a solvent submersion technique was

prompted by the poor DMA response of these films in dry state. In this study, ethylene glycol (solubility parameter = 33.4 x $10^3$ $J^{1/2}.m^{-2/3}$) was chosen as the plasticizing solvent, because it is a higher boiling solvent and has similarities in its softening capabilities to water (solubility parameter = 48.0 x $10^3$ $J^{1/2}.m^{-2/3}$).

The storage modulus of NC-OL-PDDA film was seen to be significantly higher after the first cool at the lower temperature limit (0 ºC). However, the storage modulus returned to approximately similar values at the higher temperature limit (120 ºC) for all three heating steps (Figure 6.3). This increase in storage modulus is caused most likely due to the densification of the film. During the first heat, the increased mobility of the polymer chains, and the compressive force applied by the parallel plate results in a denser packing of polymers. A closer look at the storage modulus data in first heat shows an initial decrease up to 40 ºC, from which point the storage modulus was seen to increase slightly and then reach a plateau. It can be deduced that after 40 ºC, the effect of densification overshadows thermal expansion, which explains the slight increase in storage modulus. The value of thickness change during the heat-cool-heat experiments of the blended films gives a direct indication of the densification of the films. The average normalized thickness change value of the blended film (Figure 6. 4) shows a significant decrease in the thickness of the sample. The thickness value was found to decrease approximately by 20 %, which also implies a corresponding 20 % increase in density. A closer look at the thickness change during first heat corresponds well with the storage modulus data. The slope of the thickness change increases significantly at around 40 ºC, at which point the storage modulus value in first heat was seen to increase. The thickness was seen to

further decrease during the 1st cool, and reached a plateau at 30 ºC. The second heat showed an increase in thickness as the temperature increased, which can be attributed to thermal expansion. When compared to first heat, thickness value at the highest temperature of the second heat was seen to be very similar, and the storage modulus value was seen to be only slightly higher. This suggests that densification occurred mostly during first heat, which was followed by a thermal contraction and expansion in the first cool and second heat respectively. Additionally, it appears that there is hysteresis effect dependent upon if the sample is cooled or heated after the first heat

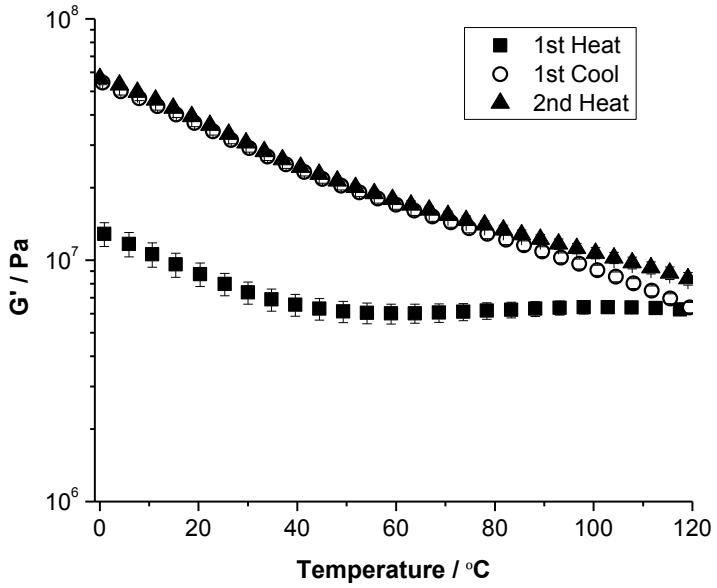


**Figure 6. 3** Average DMA storage modulus (G') curves of blended cast films of NC-OL-PDDA in heat-cool-heat experiment at 1.0 Hz (error bars represent ± 1standard deviation; n = 3).

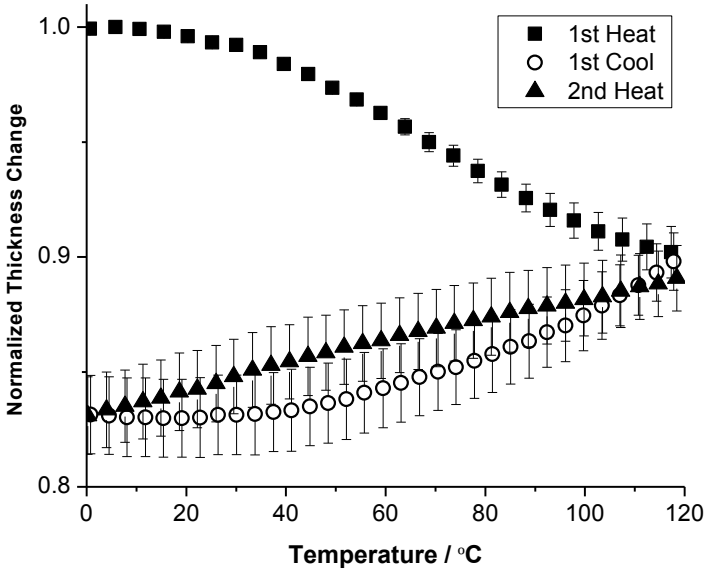


**Figure 6. 4** Average normalized thickness change curves of blended cast films of NC-OL-PDDA in heat-cool-heat experiment (error bars represent ± 1standard deviation; n = 3).

The tan δ response of NC-OL-PDDA showed a peak at 30 ºC, which was seen to recur in the first cool and 2$^{nd}$ heat (Figure 6. 5). The largest component in terms of weight in the blended cast film is NC (50 % by weight). Therefore, analysis of cast films of neat NC was done to delineate the differences between independent response of NC from that of OL and PDDA. Analysis of neat OL and PDDA samples in solvent-submersion compression-torsion set-up is not possible because of the solubility of these polymers in ethylene glycol. However, the dry $T_g$ of OL and PDDA used in this study were determined by DSC to be 93 ºC and 228 ºC respectively (Appendix A 6-3). These values are in very close agreement with the $T_g$ values reported in literature.[26, 27]

The tan δ of NC-OL-PDDA film was found to decrease in intensity in first cool and second heat compared to the first heat. A similar trend was also observed in a study with

compression torsion DMA of ethylene glycol plasticized wood, where the increase in storage modulus and decrease in damping associated with densification was reported.[28]

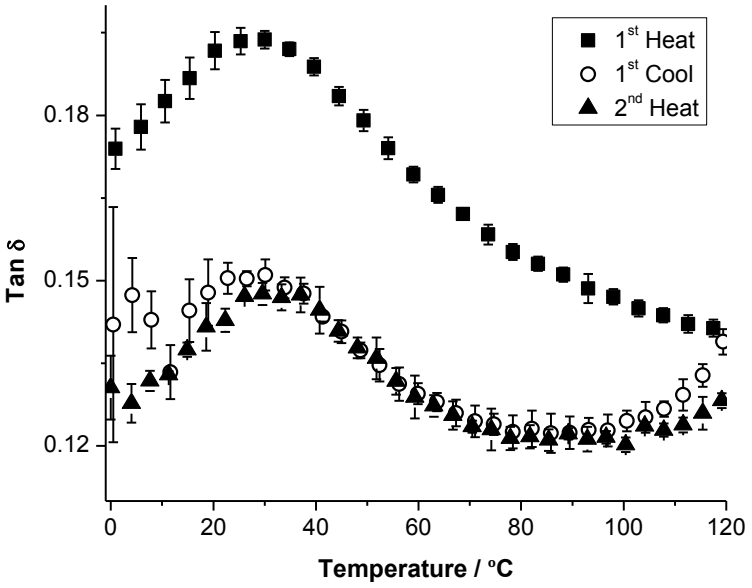


**Figure 6. 5** Average tan δ curves of blended cast films of NC-OL-PDDA in heat-cool-heat experiment at 1.0 Hz (error bars represent ± 1standard deviation; n = 3).

The storage modulus response of neat NC cast films in normal force control, at 1 Hz is shown in Figure 6.6. The storage modulus of plasticized NC films was found to vary between $10^6$ and $10^7$ Pa, which is significantly lower than NC-OL-PDDA films. This difference in modulus suggests that the addition of the OL and PDDA have a significant effect on the mechanical properties of the composite films. Contrasting to NC-OL-PDDA film, the storage modulus in the first heat of NC film did not plateau, but was seen to increase up to the upper temperature limit. The storage modulus of NC-OL-PDDA film was seen to be significantly higher after the first cool at the lower temperature limit. However, the storage modulus returned to approximately similar values at the higher temperature limit for all three steps. The film thickness change response showed a

similar trend as NC-OL-PDDA films in all the three steps (Figure 6. 7). The change in thickness from the beginning of first heat to the end of first cool was found to be approximately 27 %. Hence the neat NC films densified slightly more than NC-OL-PDDA films. From these results it can be suggested that the densification process in both neat NC films and NC-OL-PDDA blend films are very similar, and should be closely associated with NC. Like the NC-OL-PDDA system there is a clear hysteresis effect.

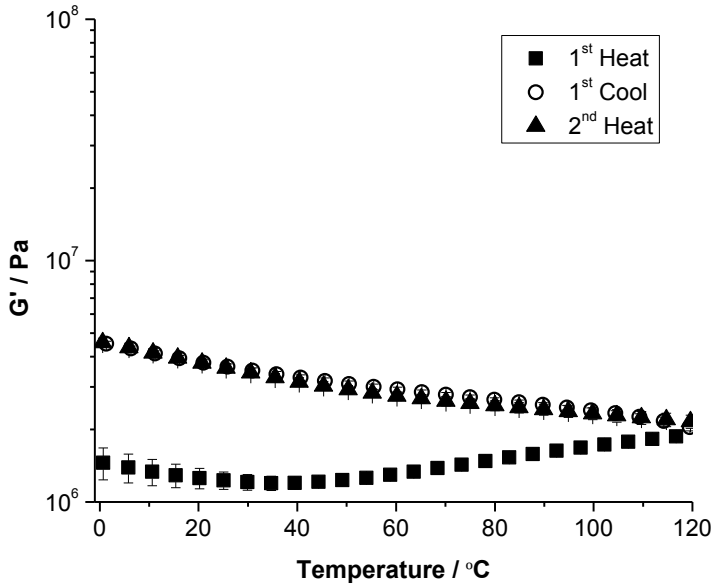


**Figure 6. 6** Average storage modulus (G') curves of cast films of NC in heat-cool-heat experiment at 1.0 Hz (error bars represent ± 1standard deviation; n=3).

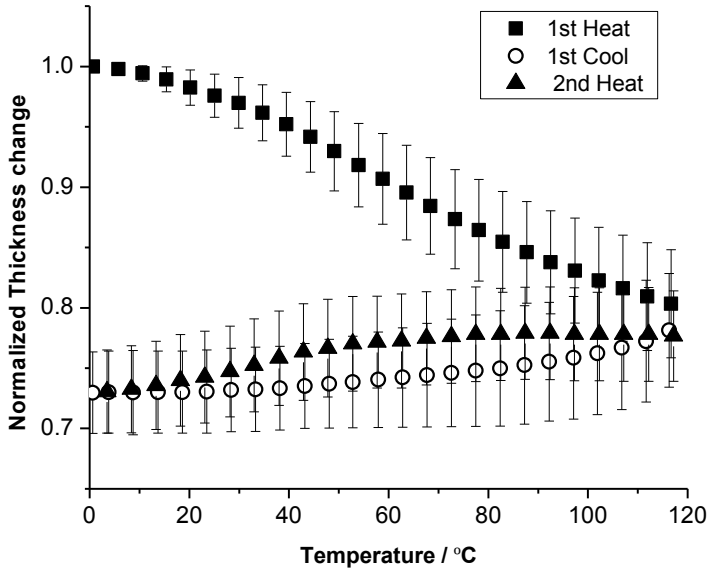


**Figure 6. 7** Average normalized thickness change curves of cast films of NC in heat-cool-heat experiment (error bars represent ± 1standard deviation; n = 3).

Similarities were also observed between NC and NC-OL-PDDA film with respect to the tan δ response. The tan δ peak observed at 30 ºC in NC-OL-PDDA was not as pronounced in NC films, nevertheless, a broad relaxation with a peak at around 27 ºC (Figure 6.8) can be observed in the second heat. This suggests that the relaxation seen at 30 ºC in NC-OL-PDDA is primarily associated with NC, which seems to be more pronounced due to the presence of OL and PDDA. The intensity of the tan δ value was found to be lower in first cool scan and second heat scan compared to first heat scan. This result, again, can be attributed to the effect of densification of the films during first heat.

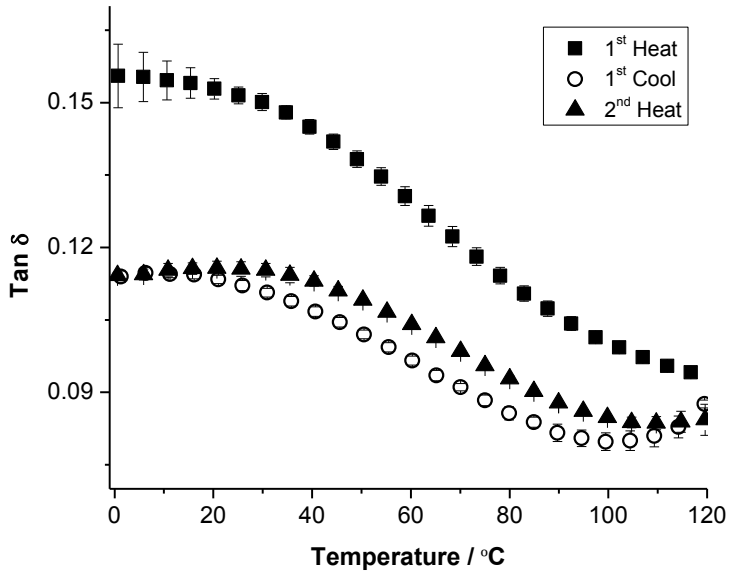


**Figure 6. 8** Average tan δ curves of cast films of NC in heat-cool-heat experiment at 1.0 Hz (error bars represent ± 1standard deviation; n = 3).

The storage modulus response of LbL films in normal force control, at 1 Hz is shown in Figure 6.9. The storage modulus of plasticized LbL films was found to occur in a range between NC-OL-PDDA and NC films. The storage modulus response of LbL films has similarities to NC-OL-PDDA and neat NC films. Like with the other two films, the storage modulus was seen to decrease initially up to 30 ºC in the first heat. This was followed by a slight increase up to 70 ºC, after which there was another decrease in modulus up to 120 ºC. After the first cool, the storage modulus was found to be significantly higher than the beginning of first heat. The second heat was found to be very similar to first cool.

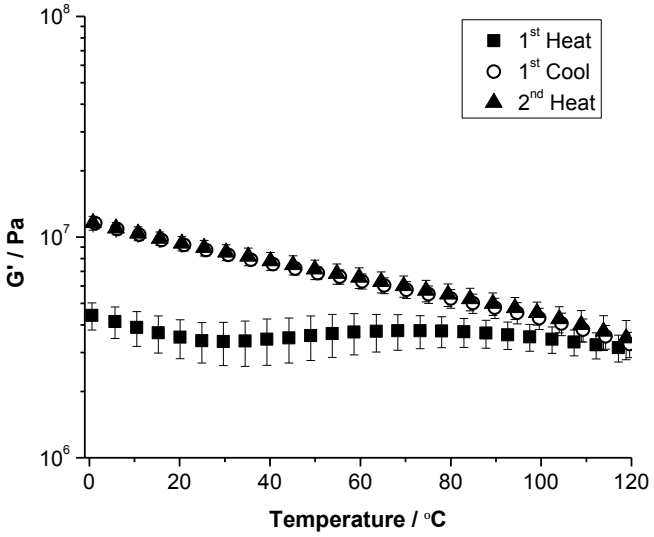


**Figure 6. 9** Average storage modulus (G') curves of LbL films in heat-cool-heat experiment at 1.0 Hz (error bars represent ± 1standard deviation; n=3).

The thickness change data of LbL films (Figure 6. 10) is in stark contrast to that of NC-PDDA-OL and NC films. In case of LbL films, the thickness of the films was seen to increase starting around 40 ºC, which is the opposite effect of the observation with NC-OL-PDDA and NC. Moreover, after the first cool, the thickness at the lower temperature limit was higher than the initial thickness at the beginning of first heat by 7.5 %. This data suggest that the LbL films were swollen after the first heat and first cool, as opposed to densification observed in NC-OL-PDDA and NC films.

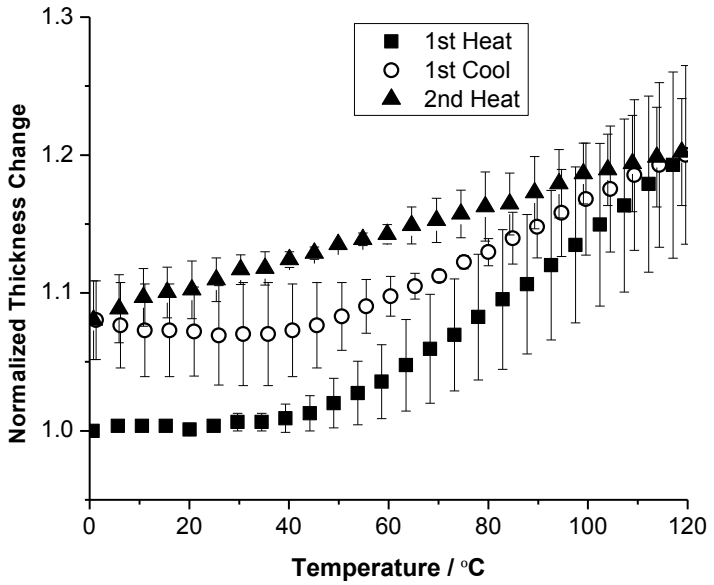


**Figure 6. 10** Average normalized thickness change curves of LbL films in heat-cool-heat experiment (error bars represent ± 1standard deviation; n = 3).

Tan δ response of LbL films showed a peak at 40 ºC in the first heat, however this peak was not observed in first cool or the second heat (Figure 6. 11). The occurrence of this relaxation at the same temperature, which is similar to that of NC-OL-PDDA and NC suggests that the relaxation mechanism is similar in all three films. However, the differences in thickness change and tan δ response of LbL films can be attributed to the distinctly different organization of the polymers due to the LbL deposition. Another observation common to all three films is the appearance of an increasing trend in tan δ at around 90 - 100 ºC in first cool and second heat. The presence of this trend in all three film samples suggests that it is attributed to NC.

Electrostatic interactions between the positively charged quaternary ammonium groups of PDDA and negatively charged carboxylate groups of NC is responsible for polyelectrolyte complex (PEC) formation in blends of NC-OL-PDDA. The same

mechanism is responsible for driving the sequential adsorption process in LbL films.[29] Strong interactions also exist between PDDA and OL.[30, 31] Both NC-OL-PDDA blends and LbL films may essentially be considered as PECs, and the resulting electrostatic interactions between the polymers may be considered as physical cross-links, which results in an increase in the $T_g$ of a blend.[32] Studies on the effect of PEC formation on the $T_g$ of the resulting blends have not been widely reported. It has been reported that at high degrees of complexation, $T_g$ could not be detected in the PECs.[33,34] However, at low degrees of complexation, two different $T_g$ could be seen, which moved closer to each other, as the degree of complexation increased.[32,34,35]

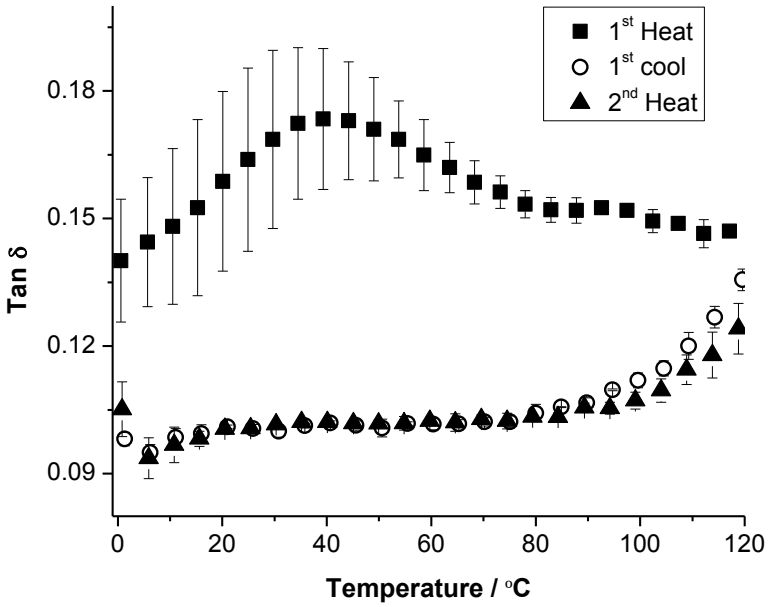


**Figure 6. 11** Average tan δ curves of LbL films in heat-cool-heat experiment at 1.0 Hz (error bars represent ± 1standard deviation; n = 3)

#### *6. 4. 2. 1 Frequency Sweep*

The tan δ peak found in the temperature region 30- 40 ºC was found to be frequency dependent for NC-OL-PPDA films. The frequency dependence was found to be more pronounced in second heat compared to the first heat (Figure 6. 12). In case of NC films, the frequency dependence was not observed in first heat, but was clearly observed in the second heat (Figure 6. 13). Even though a tan δ peak was observed for LbL films in the 35-40 ºC region, this peak did not exhibit clear frequency dependence, moreover, it did not reappear in second heat (Figure 6. 14). The lack of clear frequency dependence in the first heat may be attributed to the fact that the NC-OL-PDDA and NC films were undergoing densification, and the LbL films were undergoing swelling. However, the clearer frequency dependence of NC-OL-PDDA and NC films in the second heat can be explained by the fact that densification/swelling process was mostly complete by the end of the first heat. The second heat was associated with a linear thermal expansion for all three films, as observed from the thickness change data. This means that the material attained a more equilibrium state after the first heat-cool cycle. The disappearance of the tan δ peak in the second heat of LbL films may be explained on the basis that the polymer phase responsible for the relaxation seen in the first heat might have attained a more equilibrium distribution in the bulk phase in the second heat, hence making it difficult to detect.

The apparent activation energy ($E_a$) for the relaxation observed between 27 – 40 ºC for NC-OL-PDDA and NC films in second heat was calculated based on a modified

Arrhenius relation (equation 6.1), by plotting the log of $f$ (Hz) versus 1/T ($K^{-1}$) for four different frequencies (1.0, 2.1, 4.6, and 10.0 Hz).[36]

$$\log f = \log f_0 - E_a/RT \qquad (6.1)$$

The value of $E_a$ for NC-OL-PDDA and NC was found to be 80 kJ $mol^{-1}$ and 65 kJ $mol^{-1}$ respectively. The $\alpha$ transition or the $T_g$ of wood that has been plasticized with water has been found to fall in a temperature region of 80 – 100 ºC. This has been primarily attributed to the *in situ* lignin glass transition, and the associated activation energies have been estimated to be in the range of 300 – 400 kJ $mol^{-1}$.[36,37] Two other low temperature transitions namely $\gamma$ and $\beta$ have been observed in wood at sub-ambient temperatures. The activation energy of the $\beta$ transition in wood has been estimated to be 102 kJ $mol^{-1}$.[36] In a study with amorphous cellulose, the activation energy for the $\beta$ transition was found to be around 85 kJ $mol^{-1}$, which was seen to decrease with increasing moisture content.[38] The $\beta$ transition of amorphous cellulose was frequency dependent, and was found to fall in a range of -83 to -43 ºC, depending on the moisture content. The nature of this relaxation has been proposed to be due to the motion of hydroxymethyl groups in relation with water, however, there is also argument that it is due to the localized motion of the main chain segments.[38] Based on the activation energy, frequency dependence, and the temperature of the transition observed in the composite films used in this study, the nature of the relaxation observed can be associated with a secondary cellulose transition similar to the amorphous cellulose $\beta$-transition. Moreover, the higher temperature of this transition observed in the composite films tested in this study, when compared to

literature may be due to the semi-crystalline nature of the cellulose used. Another factor could be the choice of plasticizer (ethylene glycol), as opposed to water, which is a better plasticizer for cellulose.

Another important observation in the tan δ curves of all samples is the appearance of the beginning of a relaxation at around 90 – 100 ºC in second heat. Since the experiments were conducted only up to 120 ºC, the peak of this transition was not observed. In the narrow window (30 ºC) in which this transition was seen, it was found to be frequency dependent. Again, the appearance of this trend in all three samples suggests that it is associated with NC.

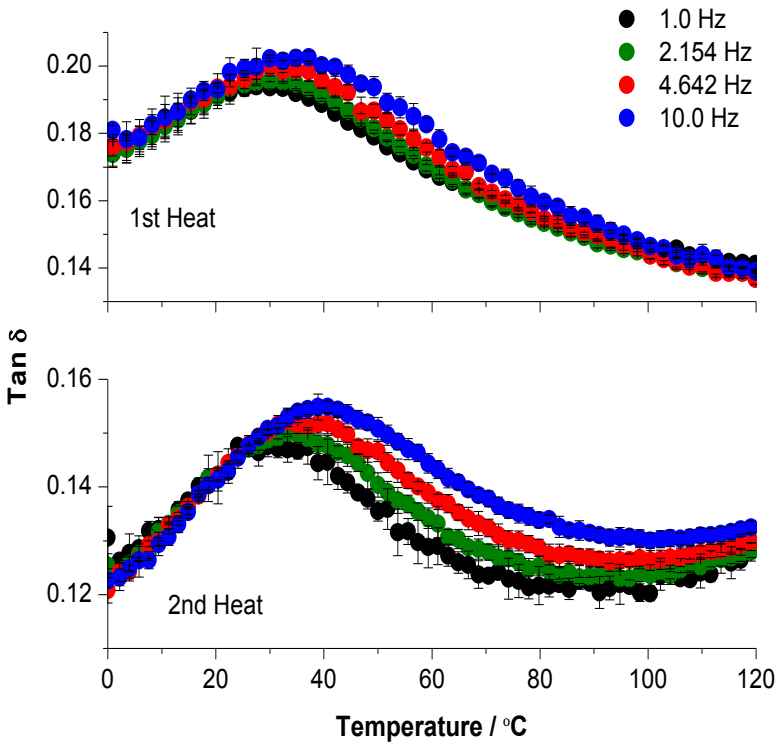


**Figure 6. 12** Tan δ response of NC-OL-PDDA films in first heat and second heat for four different frequencies (error bars represent ± 1standard deviation; n = 3).

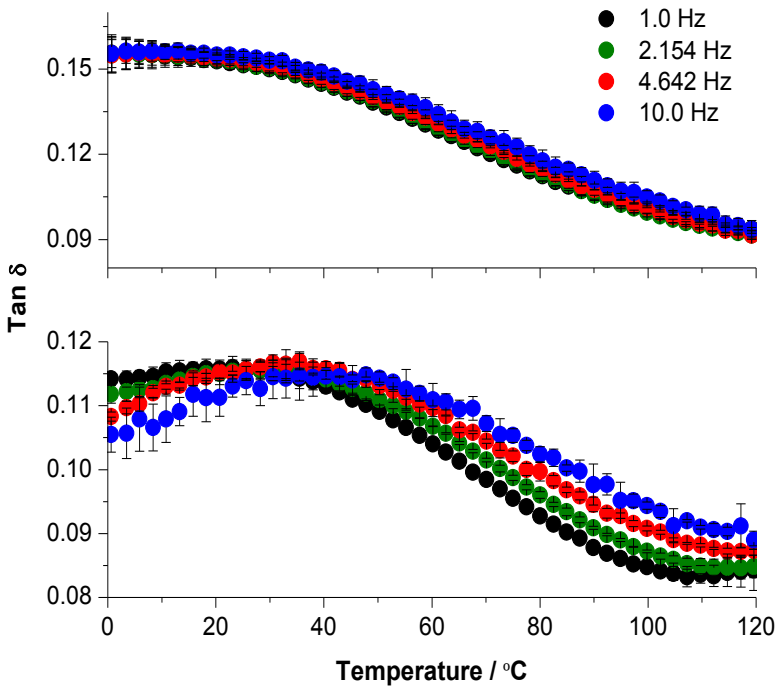


**Figure 6. 13** Tan δ response of NC films in first heat and second heat for four different frequencies (error bars represent ± 1standard deviation; n = 3).

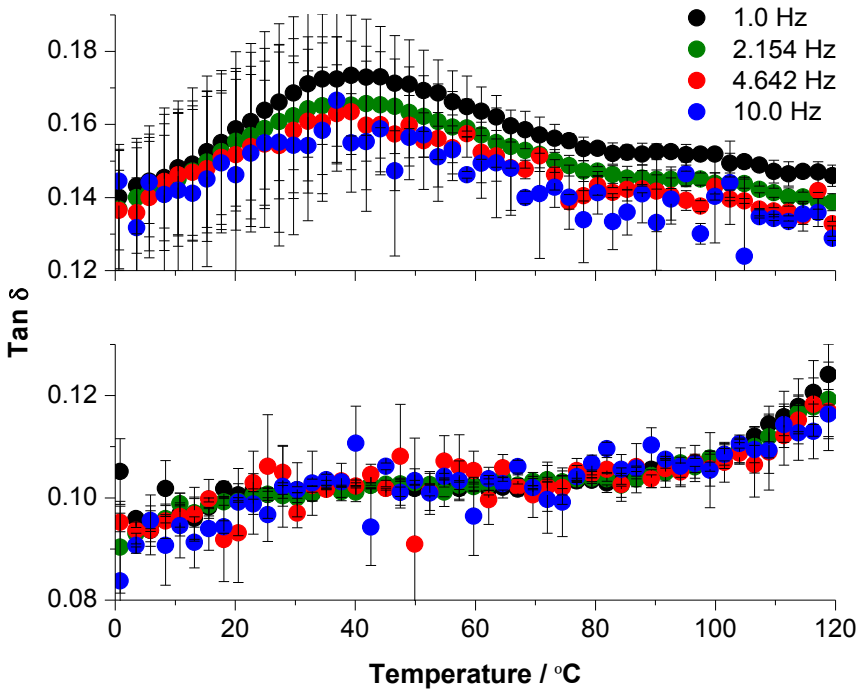


**Figure 6. 14** Tan δ response of LbL films in first heat and second heat for four different frequencies (error bars represent ± 1standard deviation; n = 3).

### *6. 4. 2. 2 Time Temperature Super Position (TTSP) Master Curves*

The storage modulus response of 7 frequencies (0.1, 0.2154, 0.4645, 1.0, 2.154, 4.645 and 10.0 Hz) from the second heat (Figure 6. 15) were used fit to a fifth order polynomial to generate isotherms at every 5 ºC (Figure 6. 16).[39] To create a master curve, the isotherms were shifted horizontally along the frequency scale, by taking the isotherm at 30 ºC as the reference. The isotherm at 30 ºC was chosen was chosen as the reference temperature based on the value of Tan δ peak observed in NC-OL-PDDA films. Smooth master curves were observed with the second heat storage modulus data for all three films (Figures 6. 17 - 6. 19). However, attempts to create master curves for loss modulus (Appendix A 6-2) and Tan δ data did not result in a smooth and continuous fit. The shift factors associated with the master curves for all three films are shown in Figure 6. 20.

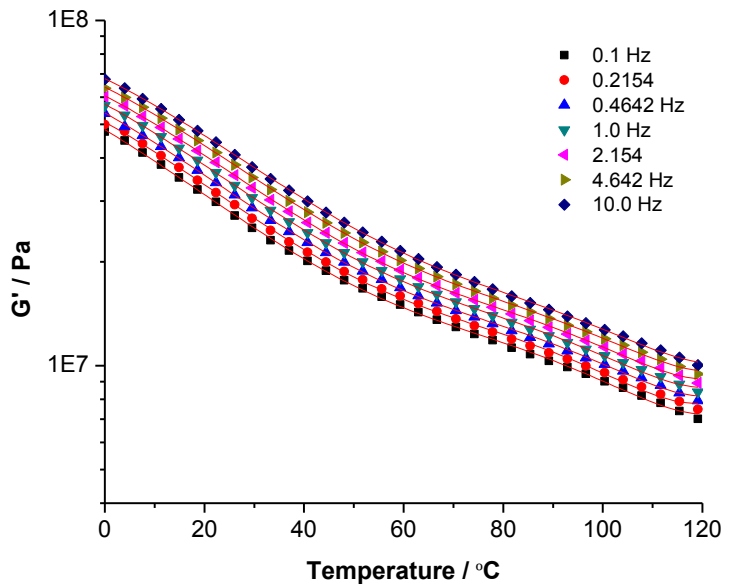


**Figure 6. 15** Representative curves showing 5th order polynomial fits to the storage modulus response in second heat of NC-OL-PDDA films for 7 different frequencies (0.1, 0.2154, 0.4645, 1.0, 2.154, 4.645 and 10.0 Hz).

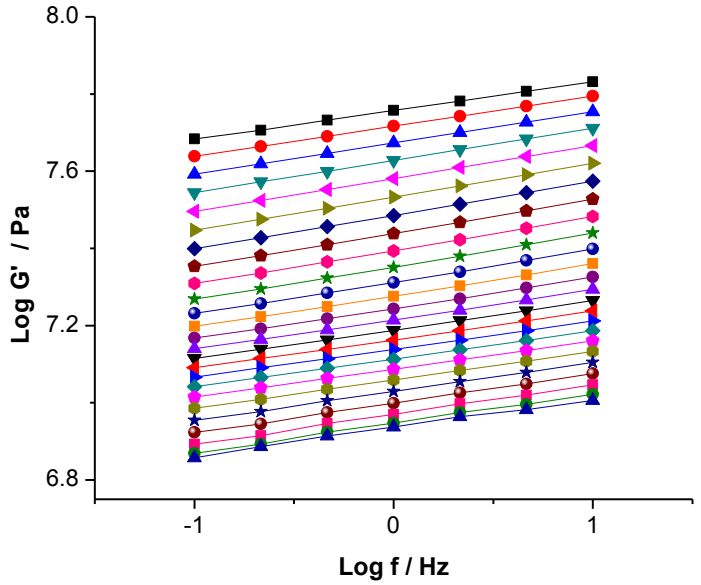


**Figure 6. 16** Isotherms generated from the 5th order polynomial fit described in Figure 6. 15.

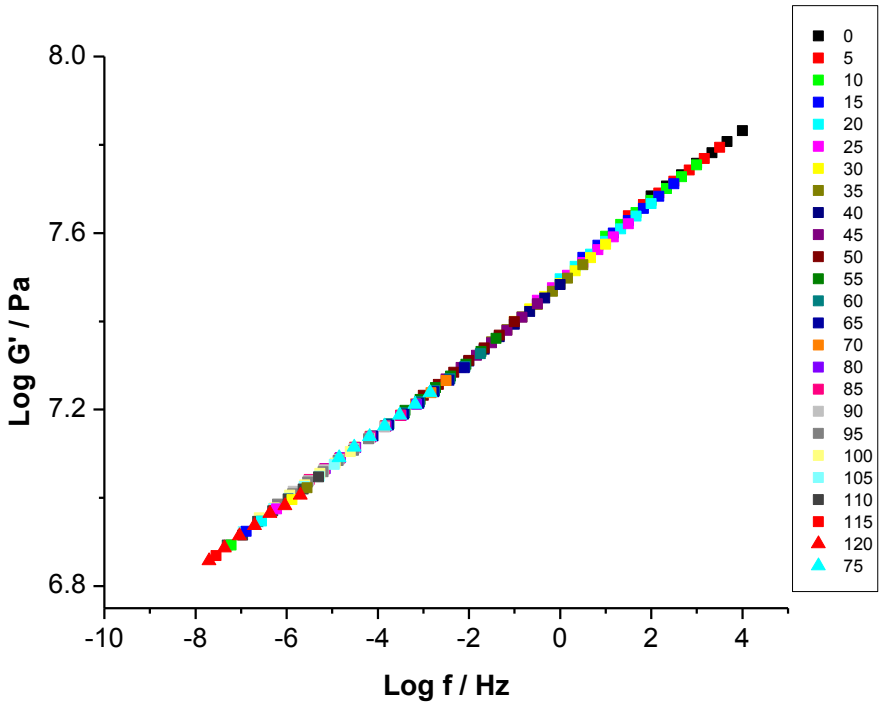


**Figure 6. 17** Storage modulus master curve of NC-OL-PDDA films for second heat.

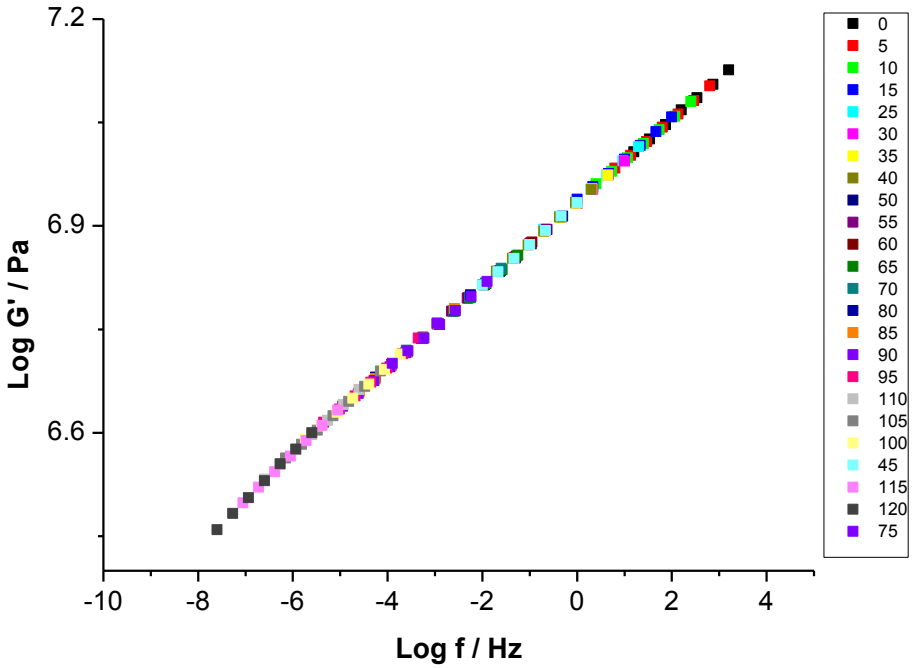


**Figure 6. 18** Storage modulus master curve of LbL films for second heat.

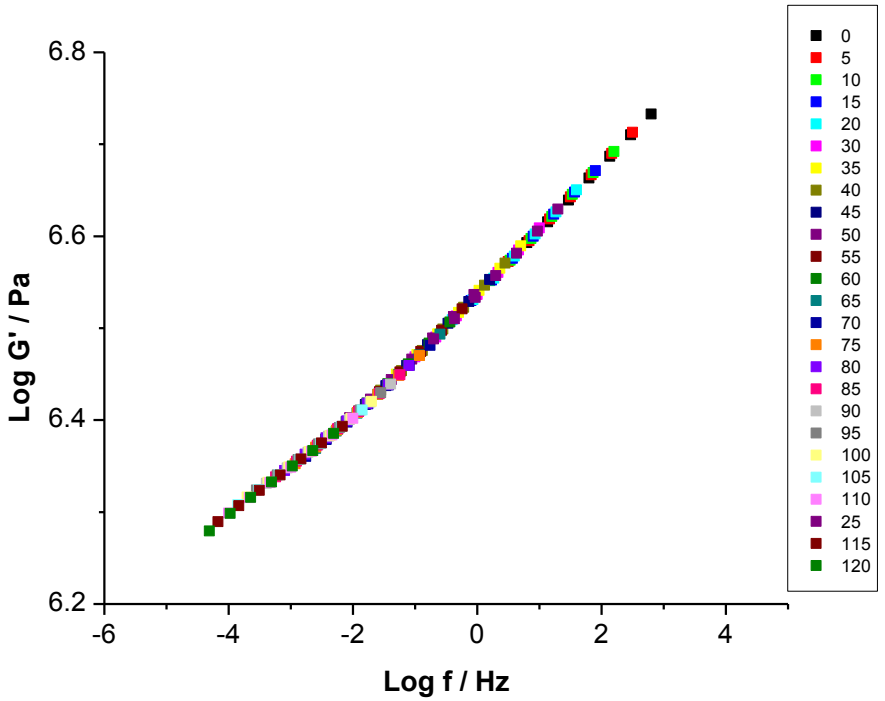


**Figure 6. 19** Storage modulus master curve of NC films for second heat.

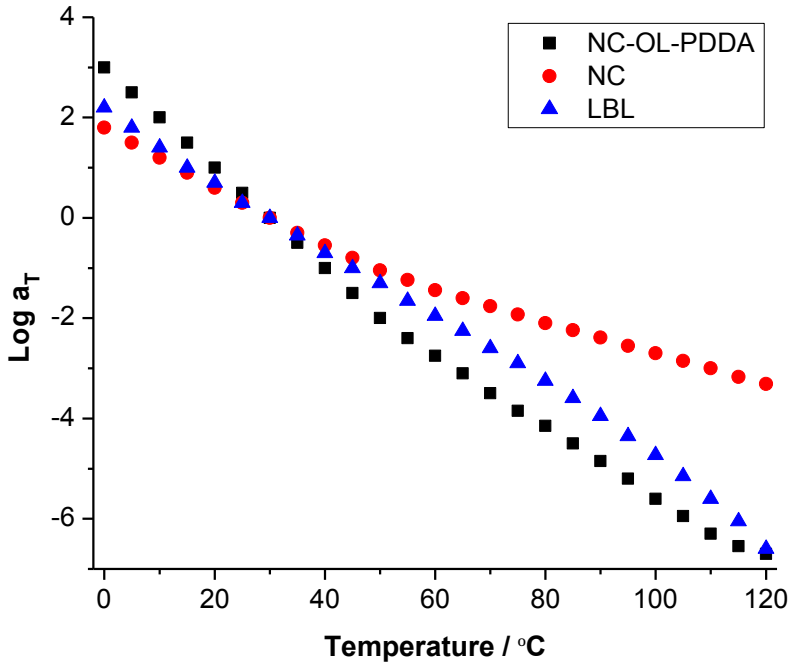


**Figure 6. 20** Shift factor plots obtained from TTSP of storage modulus isotherms of NC-OL-PDDA, NC, and LbL films.

The ability to generate smooth TTSP mastercurves and shift factor plots suggests the predominance of a single type of molecular motion.[40] The principle of TTSP may not hold true for a particular polymeric system due to the presence of more than one type of molecular motion which have different temperature dependencies. This issue is particularly true in the case of polymer blends, where different components have different temperature responses. TTSP also may not hold for materials that undergo significant physical or chemical changes during the experiment.[40] In this respect, it is interesting to note that the NC-OL-PDDA and NC films underwent densification, whereas the LbL films showed swelling during the course of the first heat and first cool, for which mastercurves could not be generated. The distinct difference in the response of LbL films to cast films can be attributed to the differences in the organization of the polymers in the

two different systems. In LbL films, the NC fibrils are present as layers which are only 4-5 nm (chapter 5) in thickness, and complexed closely with PDDA and lignin. Whereas in NC-OL-PDDA cast films, the polymers might be more phase separated.

## 6. 5 Conclusions

Nanocomposite films composed of isolated wood polymers namely NC and OL were made in combination with cationic polymer PDDA. Free-standing composite films were created utilizing a LbL deposition technique. Also, cast films were prepared from the blended mixture of these polymers. SEM analysis of the cross-sections showed that the LbL films had a lamellar architecture, with layers in the nanometer scale. DMA of the ethylene glycol plasticized films were carried out in compression-torsion mode with an 8 mm parallel plate attachment in a rheometer. Both LbL and cast films of NC-OL-PDDA showed a tan $\delta$ peak in 30 – 40 ºC region in first heat, which was seen to disappear in second heat for the LbL films. The LbL films were seen to undergo swelling, whereas the NC-OL-PDDA blend films were seen to undergo densification after the first heat-cool cycle. Comparison of composite films to neat NC cast films showed that the relaxation seen at 30- 40 ºC is found in both systems. This relaxation was found to have clear frequency dependence in second heat for NC-OL-PDDA blend and neat NC films, and the associated $E_a$ for this relaxation was 80 and 65 kJ $mol^{-1}$ respectively. Storage modulus master curves and corresponding shift factor plots could be generated from the second heat data for all three types of films.

## 6. 6 References


1. Munch, E.; Launey, M. E.; Alsem, D. H.; Saiz, E.; Tomsia, A. P.; Ritchie, R. O., *Science* **2008,** 322, 1516-1520.

2. Baer, E.; Hiltner, A., *Phys. Today* **1992,** 45, 60.

3. Salmén, L., *C. R. Biol.* 327, 873-880.

4. Fengel, D., Wegener, G. , *Wood-Chemistry, Ultrastructure, Reactions*. Walter de Gruyter: New York, 1989.

5. Burgert, I., *Am. J. Bot.* **2006,** 93, 1391-1401.

6. Kojima, Y.; Usuki, A.; Kawasumi, M.; Okada, A.; Fukushima, Y.; Kurauchi, T.; Kamigaito, O., *J. Mater. Res.* **1993,** 8, 1185-1189.

7. Favier, V.; Chanzy, H.; Cavaillé, J. Y., *Macromolecules* **1995,** 28, 6365-6367.

8. Samir, M. A. S. A.; Alloin, F.; Dufresne, A., *Biomacromolecules* **2005,** 6, 612-626.

9. Siró, I.; Plackett, D., *Cellulose* **2010,** 17, 459-494.

10. Saito, T.; Nishiyama, Y.; Putaux, J.-L.; Vignon, M.; Isogai, A., *Biomacromolecules* **2006,** 7, 1687-1691.

11. Johnson, R.; Zink-Sharp, A.; Renneckar, S.; Glasser, W., *Cellulose* **2009,** 16, 227-238.

12. Li, Q.; Renneckar, S., *Cellulose* **2009,** 16, 1025-1032.

13. Li, Q.; Renneckar, S., *Biomacromolecules* **2011,** 12, 650-659.

14. Šturcová, A.; Davies, G. R.; Eichhorn, S. J., *Biomacromolecules* **2005,** 6, 1055-1061.

15. Treacy, M. M. J.; Ebbesen, T. W.; Gibson, J. M., *Nature* **1996,** 381, 678-680.

16. Fratzl, P.; Burgert, I.; Gupta, H. S., *Phys. Chem. Chem. Phys.* **2004,** 6, 5575-5579.

17. Rusli, R.; Eichhorn, S. J., *Appl. Phys. Lett.* **2008,** 93, 033111-3.

18. Lin, Z.; Renneckar, S.; Hindman, D., *Cellulose* **2008,** 15, 333-346.

19. Decher, G., *Science* **1997,** 277, 1232.

20. Podsiadlo, P.; Kaushik, A. K.; Arruda, E. M.; Waas, A. M.; Shim, B. S.; Xu, J.; Nandivada, H.; Pumplin, B. G.; Lahann, J.; Ramamoorthy, A.; Kotov, N. A., *Science* **2007,** 318, 80-83.

21. Becker, A. L.; Johnston, A. P. R.; Caruso, F., *Small* **2010,** 6, 1836-1852.

22. Ashcraft, J. N.; Argun, A. A.; Hammond, P. T., *J. Mater. Chem.* **2010,** 20, 6250-6257.

23. Lee, S. W.; Yabuuchi, N.; Gallant, B. M.; Chen, S.; Kim, B.-S.; Hammond, P. T.; Shao-Horn, Y., *Nat Nano* **2010,** 5, 531-537.

24. Karabulut, E.; Wagberg, L., *Soft Matter* **2011,** 7, 3467-3474.

25. Krogman, K. C.; Zacharia, N. S.; Schroeder, S.; Hammond, P. T., *Langmuir* **2007,** 23, 3137-3141.

26. Glasser, W. G.; Barnett, C. A.; Muller, P. C.; Sarkanen, K. V., *J. Agr. Food Chem.* **1983,** 31, 921-930.

27. Gordon, M. A naceous self-assembled nanolaminate for corrosion resistance on 2024-Al alloy. Virginia Tech, Blacksburg, 2001.

28. Chowdhury, S.; Fabiyi, J.; Frazier, C. E., *Holzforschung* **2010,** 64, 747-756.

29. Wagberg, L.; Decher, G.; Norgren, M.; Lindstrom, T.; Ankerfors, M.; Axnas, K., *Langmuir* **2008,** 24, 784-795.

30. Pillai, K. V.; Renneckar, S., *Biomacromolecules* **2009,** 10, 798-804.

31. Norgren, M.; Gärdlund, L.; Notley, S. M.; Htun, M.; Wågberg, L., *Langmuir* **2007,** 23, 3737-3743.

32. Huglin, B. M.; Rego, J. M.; Gooda, S. R., *Macromolecules* **1990,** 23, 5359-5361.

33. Huglin, M. B.; Webster, L.; Robb, I. D., *Polymer* **1996,** 37, 1211-1215.

34. Qian, Q. Z. J.; An, Q.; Yang, Q.; Gui, Z., *ACS Appl. Mater. Interfaces* **2009,** 1, 90-96.

35. Zhang, G.; Jiang, M.; Zhu, L.; Wu, C., *Polymer* **2001,** 42, 151-159.

36. Kelley, S.; Rials, T.; Glasser, W., *J. Mater. Sci.* **1987,** 22, 617-624.

37. Salmén, L., *J. Mater. Sci.* **1984,** 19, 3090-3096.

38. Montès, H.; Mazeau, K.; Cavaillé, J. Y., *Macromolecules* **1997,** 30, 6977-6984.

39. Laborie, M. P. G.; Salmén, L.; Frazier, C. E., *Holzforschung* **2004,** 58, 129-133.

40. van Gurp, M.; Palmen, J., *Rheology Bulletin* **1998,** 67, 5.

# Chapter 7. Conclusions

Inspired by nature's high performance material wood, this work was undertaken to study the possibility of assembling isolated wood polymers into organized structures, and to investigate the result of such ordering on physical response of the polymers. In the first phase of the study, it was found that strong non-covalent interactions exist between lignin and cationic species. This interaction was found to exist in ionized as well as partially ionized conditions of alkali lignin, as observed from the high affinity coefficients, and also in ethanol, where the phenolic and carboxylic ionization is low. Furthermore, when the phenolic groups of lignin (the primary ionizing group of lignin) were replaced with methyl groups, the adsorption to cationic surface remained unchanged. An interaction between the cationic group of the polyelectrolyte PDDA and the aromatic group of alkali lignin was found by infra-red spectroscopy. This non-covalent interaction termed as cation-$\pi$ interaction is being proposed as a promising mechanism for the adsorption of lignin on positively charged surfaces, which has been utilized in the bottom-up build-up of isolated wood polymers in this study.

To meet the objective of layered organization of wood polymers, LbL assembly was utilized to combine nanocellulose and lignin with PDDA. QCM-D showed that sequential adsorption of isolated wood polymers is possible, when nanocellulose and lignin are alternated with PDDA. Moreover, the LbL process was similar for different types of lignins namely organosolv and hardwood milled wood lignin. When the LbL process was carried out repeatedly up to 250 cycles (500 bilayers) on a cellulose acetate substrate, free-standing films were obtained upon dissolving the substrate. Cross-sections

of the LbL assembled films observed under SEM were found to have a lamellar structure, with a thickness of ~ 4.3 µm, suggesting a layer thickness of ~ 17 nm per deposition cycle.

The physical response of the LbL assembled polymers were tested using DMA in compression torsion set-up after they were plasticized in ethylene glycol. The LbL films were compared to solvent-cast films prepared from the blend of the same materials (nanocellulose, organosolv lignin, and PDDA). Both LbL and blended cast films showed a tan δ peak in 30 – 40 ºC region in first heat, which was seen to disappear in second heat for the LbL films. Comparison of composite films to neat nanocellulose cast films showed that the relaxation seen at 30- 40 ºC is from nanocellulose. The LbL films were seen to undergo swelling, whereas the cast films were seen to undergo densification after the first heat-cool cycle. It is concluded that the differences observed in DMA response arise due to the lamellar organization of the polymers in the LbL films.

## Appendix A 5-1. Conductometric Titration Curves

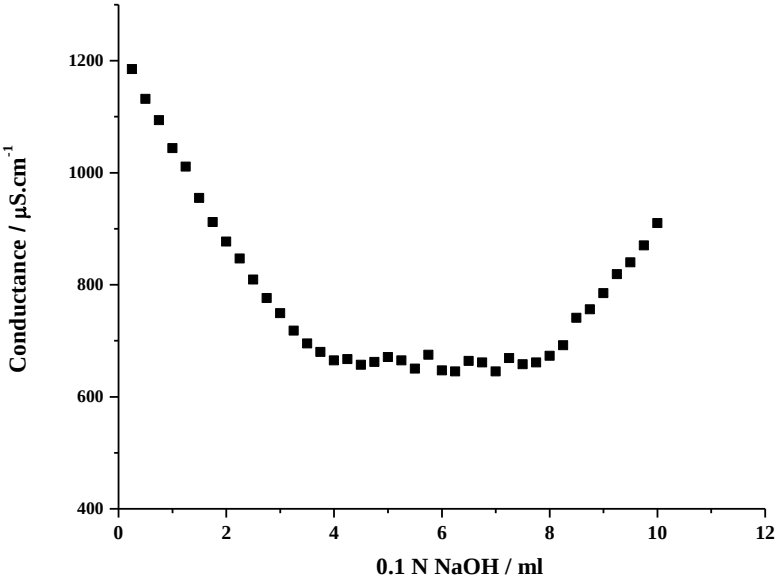


**Figure A 5. 1** Conductometric titration curve of TEMPO oxidized cellulose.

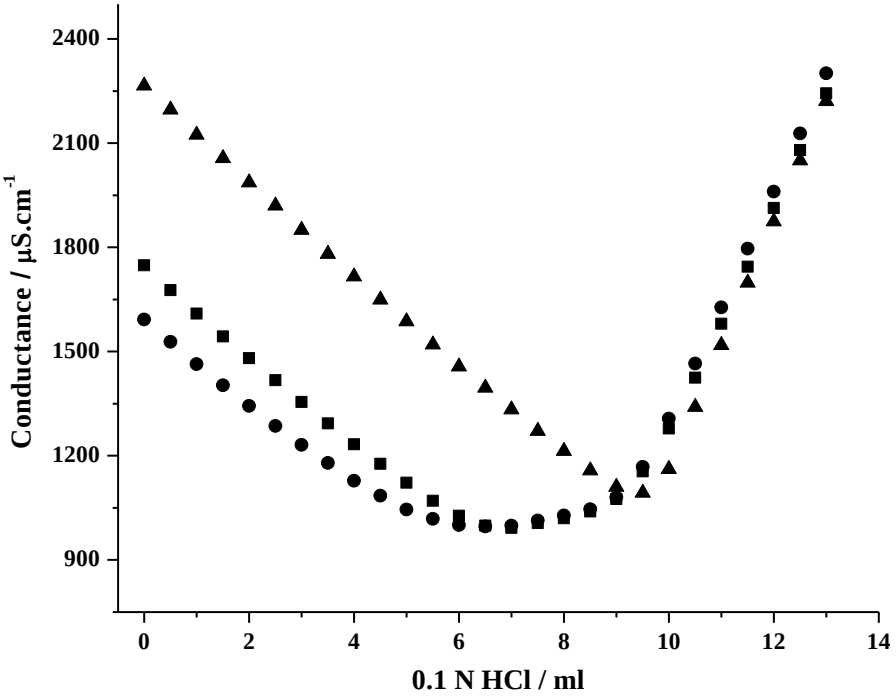


**Figure A 5. 2** Conductometric titration curves of blank (▲), HMWL (■), and OL(●).

## Appendix A 5-2. $^{1}$H NMR Spectra of Lignins

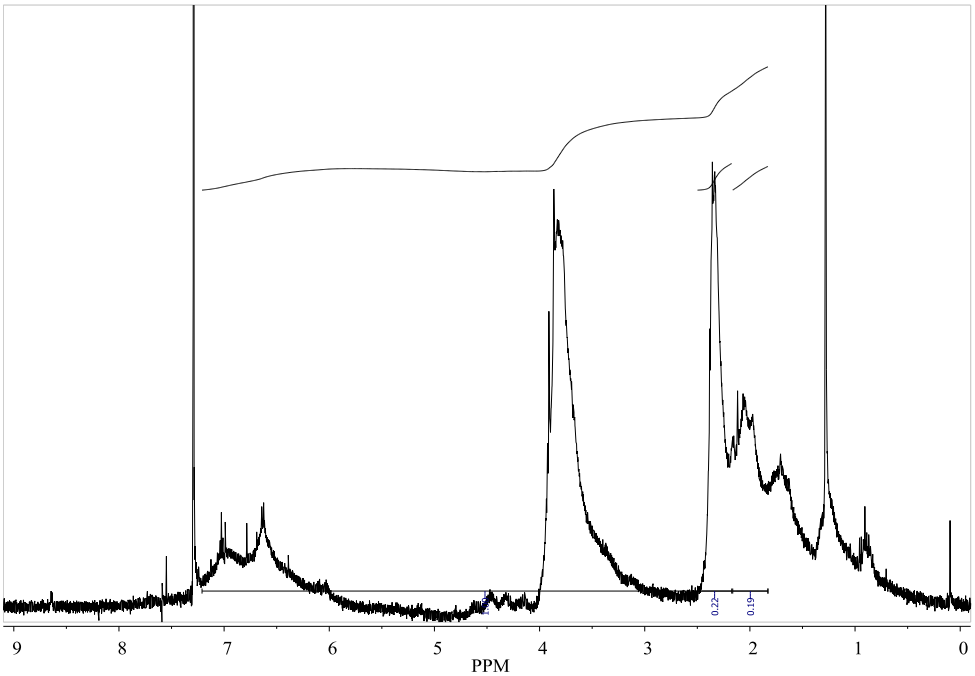


**Figure A 5. 3** $^{1}$H NMR spectra of acetylated OL.

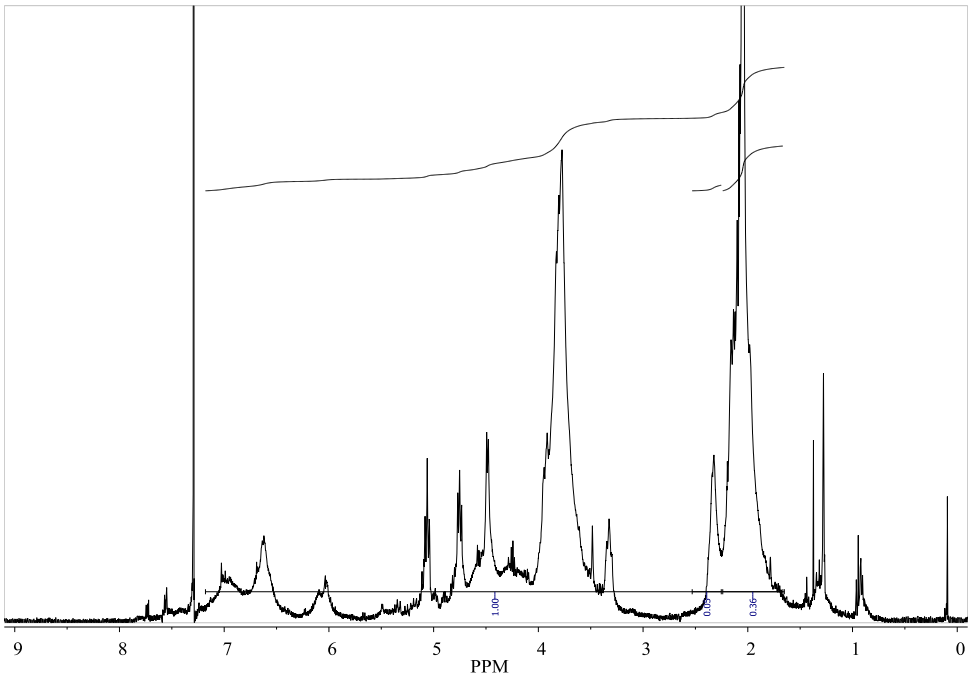


**Figure A 5. 4** $^{1}$H NMR spectra of acetylated HMWL.

## Appendix A 5-3. AFM Scratch Analysis

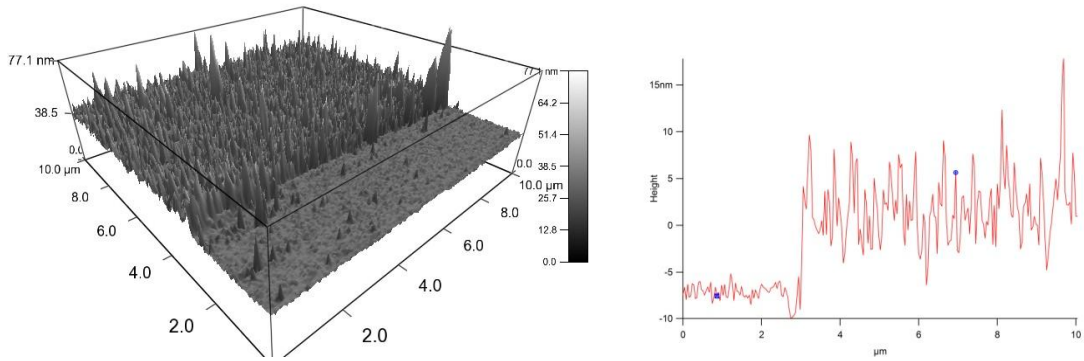


**Figure A 5. 5** AFM image of the scratch test used to estimate the film thickness, and the corresponding line graph.

## Appendix A 5-4. QCM-D Principle

QCM-D measures the change in resonant frequency and dissipation of the vibrating quartz crystal as a function of the adsorption process. Provided a rigid layer is formed, the mass of the adsorbed layer will be proportional to the change in resonant frequency, given by the Sauerbrey equation:

$$\Delta f_m = -\frac{2 \times f_o^2 \times \Delta m}{A \times \sqrt{\rho_q \mu_q}} \tag{A1}$$

where $\Delta f_m$ = change in frequency, $f_0$ = fundamental frequency, $\Delta m$ = change in mass, A = piezo-electrically active area, $\rho_q$ = density of quartz (2.648 g $cm^{-2}$), and $\mu_q$ = shear modulus of quartz (2.947 x 10-11 dynes $cm^{-2}$). The dissipation in the vibrating system associated with the adsorbed mass is given by

$$D = \frac{E_d}{2\pi E_s} = \frac{1}{\pi f \tau} \tag{A2}$$

where $E_d$ and $E_s$ are the energy dissipated and energy stored in the vibrating system, $f$ = frequency and $\tau$ = the decay time.

## Appendix A 5-5. Viscoelastic Models

Assuming that the films behave like a Voigt viscoelastic material, the film thickness, density and viscoelastic properties can be related to ΔF and ΔD using the derivations of Voinova et al. [5]

$$\Delta f \approx -\frac{1}{2\pi\rho_0 h_0} h\rho\omega\left(1+\frac{2h^2\chi}{3\delta^2(1+\chi^2)}\right) \tag{A3}$$

$$\Delta D \approx \frac{2h^3\rho\omega}{3\pi f\rho_0 h_0}\frac{1}{\delta^2(1+\chi^2)}, \qquad \chi = \frac{\mu}{\eta\omega}, \qquad \delta = \sqrt{\frac{2\eta}{\rho\omega}} \tag{A4}$$

where $\rho_0$ and $h_0$ are the density and thickness of the quartz crystal, $\rho$, h, $\mu$ and $\eta$ are the density, thickness, shear modulus and shear viscosity of the film, $\omega$ = angular frequency ($2\pi f$), and $\delta$ is the viscous penetration depth.

The Johannsmann model allows for the calculation of the true sensed mass of a viscoelastic layer based on equation (A3):

$$\delta\hat{f} \approx -f_0\frac{1}{\pi\sqrt{\rho_q\mu_q}}\left(f\rho d + \hat{J}(f)\frac{f^3\rho^2 d^3}{3}\right) \tag{A5}$$

where $\delta\hat{f}$ is the shift in complex frequency, $f_0$ is the fundamental resonance frequency of the quartz crystal in air (4.95 MHz), $f$ is the resonance frequency of the crystal in contact with liquid, $\rho$ and $d$ are the density and thickness of the deposited film, $\rho_q$ and $\mu_q$ are the density and shear modulus of quartz, and $\hat{J}(f)$ is the complex shear compliance

of the film. By introducing the equivalent mass $m*$, equation (A5) can be expressed in a more convenient form:

$$\hat{m}^* = \frac{\sqrt{\rho_q \mu_q}}{2f_0} \frac{\delta \hat{f}}{f} \tag{A6}$$

$$m^* = m^0 \left(1 + \hat{J}(f) \frac{\rho f^2 d^2}{3}\right) \tag{A7}$$

Equation (A7) is used under the assumption that $\hat{J}(f)$ is independent of the frequency in the accessible frequency range. A plot of $m*$ vs $f^2$ for different overtones gives the true sensed mass ($m^0$) as the y-intercept.

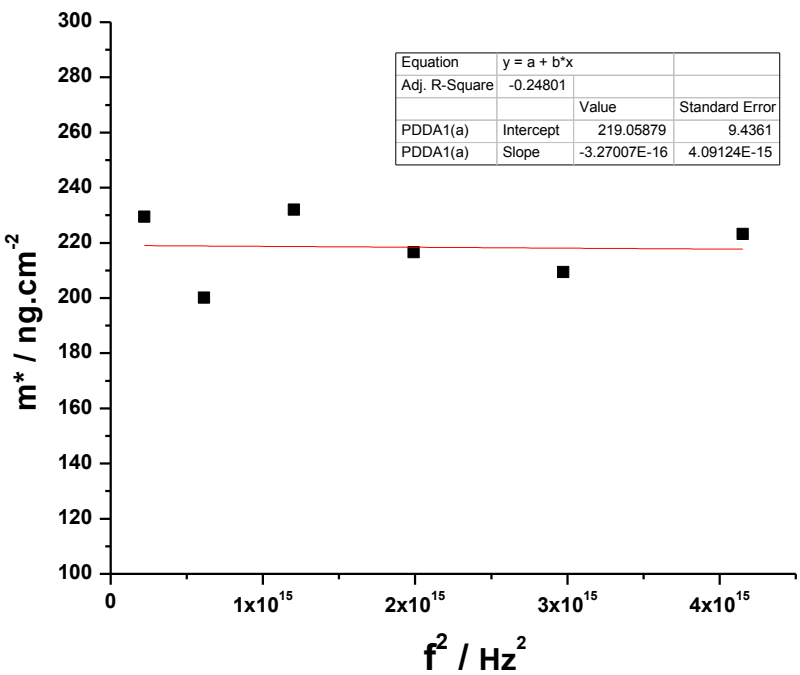


**Figure A 5. 6** Johannsmann model areal mass estimate of PDDA (layer 1; cycle 1) in NC-PDDA-HMWL

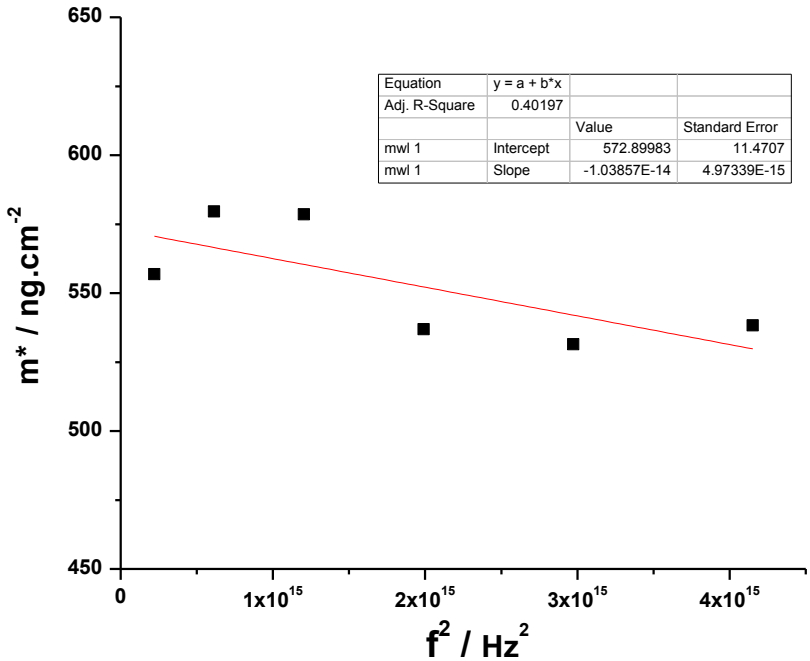


**Figure A 5. 7** Johannsmann model areal mass estimate of HMWL (cycle 1) in NC-PDDA-HMWL

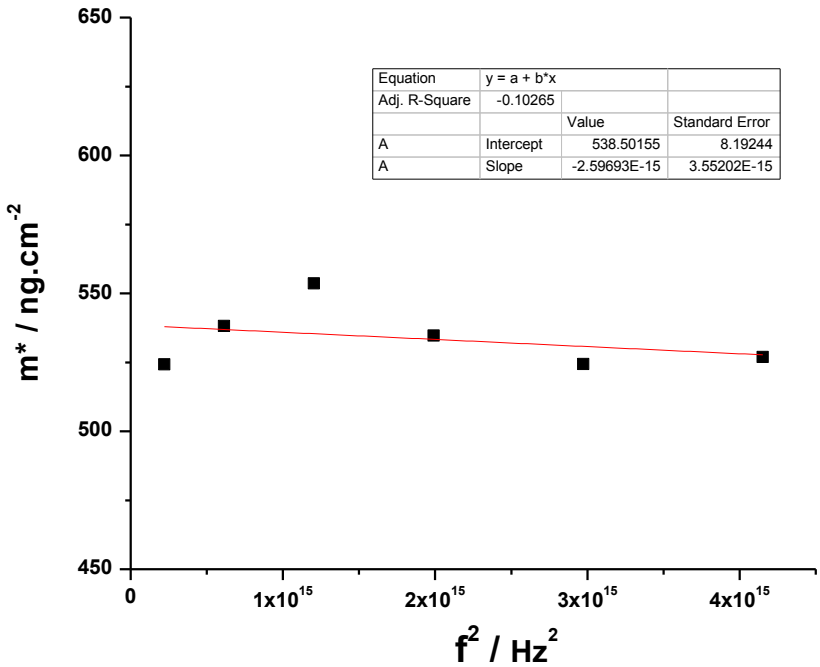


**Figure A 5. 8** Johannsmann model areal mass estimate of PDDA (layer 2; cycle 1) in NC-PDDA-HMWL

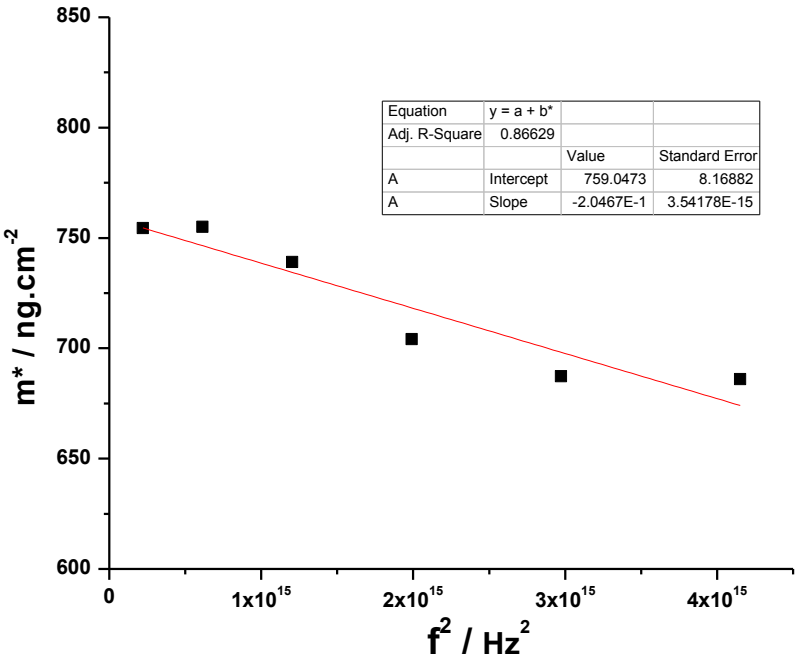


**Figure A 5. 9** Johannsmann model areal mass estimate of NC (cycle 1) in NC-PDDA-HMWL

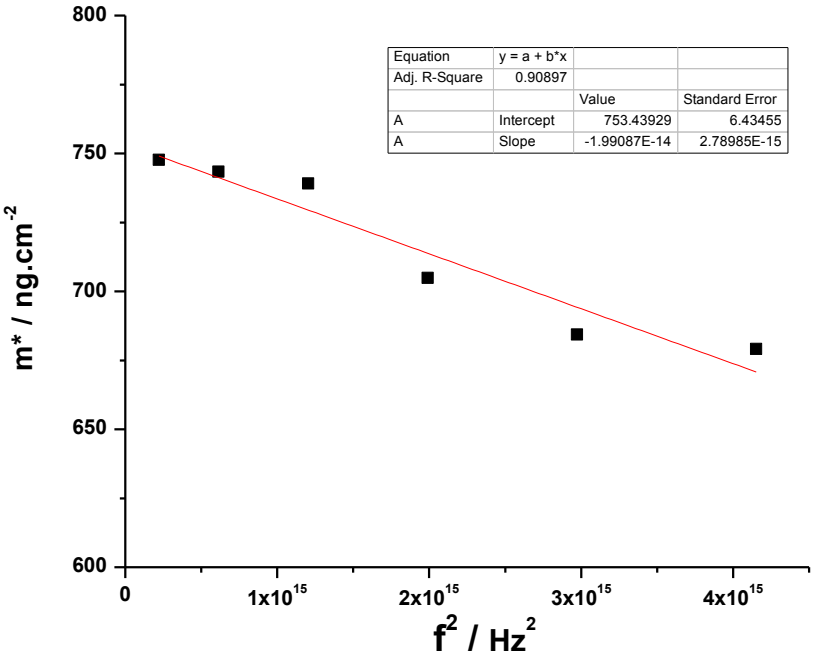


**Figure A 5. 10** Johannsmann model areal mass estimate of PDDA (layer 1; cycle 2) in NC-PDDA-HMWL

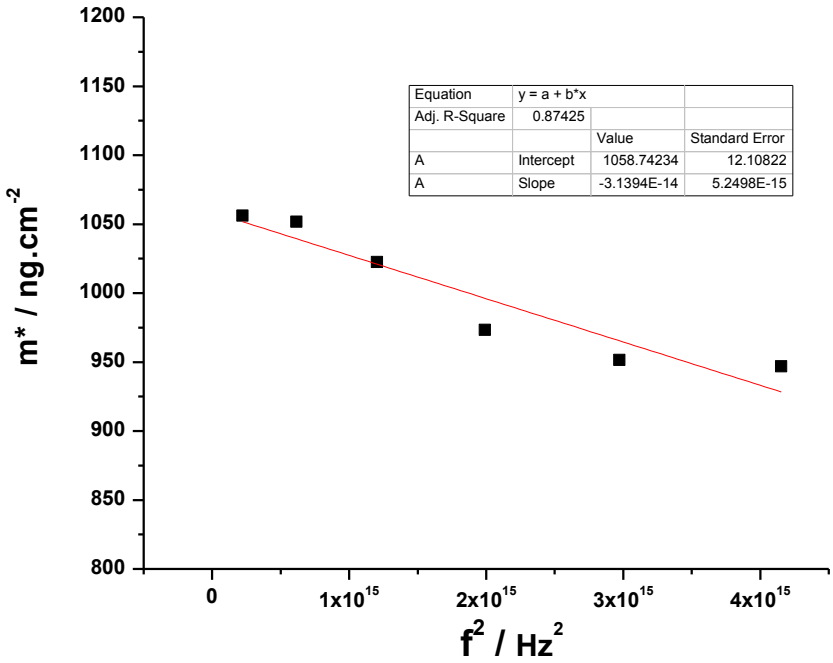


**Figure A 5. 11** Johannsman model areal mass estimate of HMWL (cycle 2) in NC-PDDA-HMWL

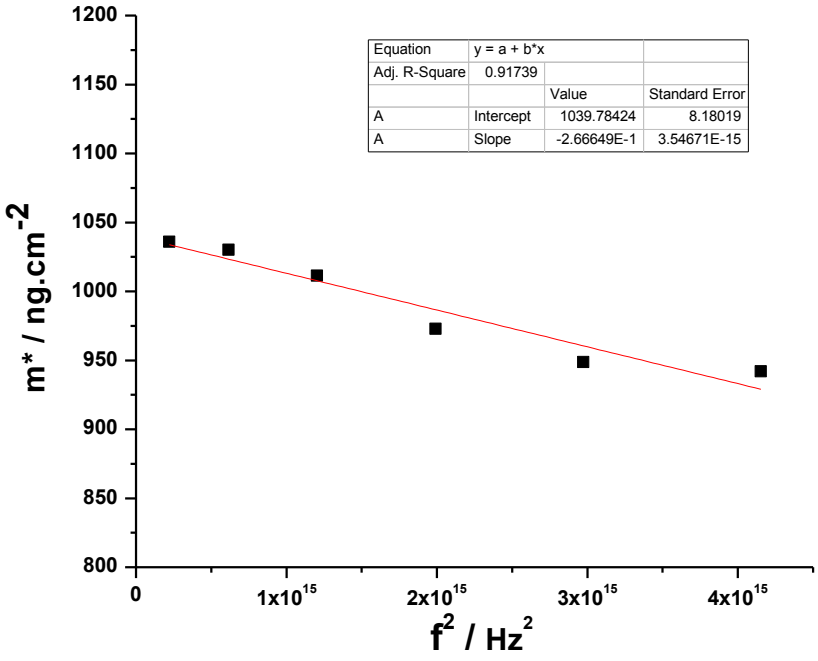


**Figure A 5. 12** Johannsmann model areal mass estimate of PDDA (layer 2; cycle 2) in NC-PDDA-HMWL

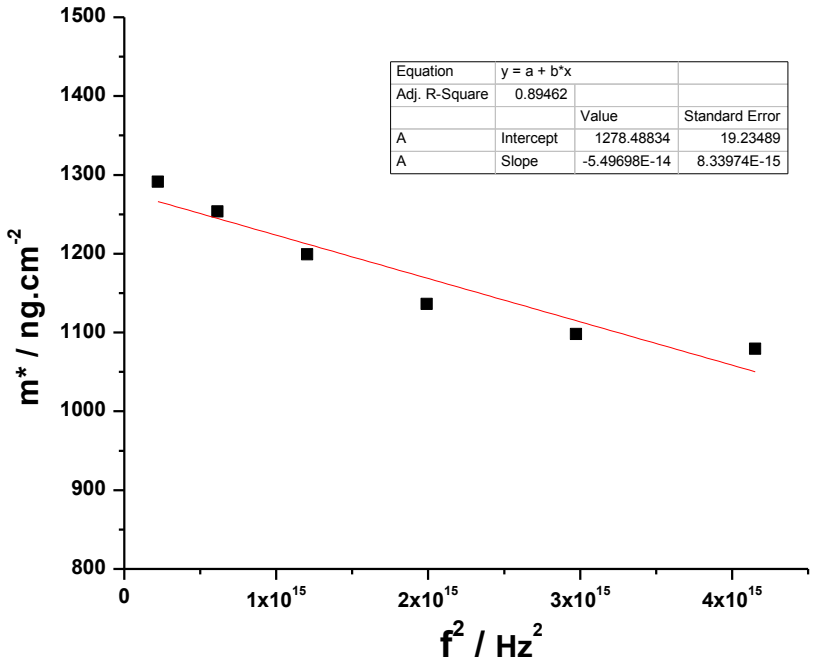


**Figure A 5. 13** Johannsmann model areal mass estimate of NC (cycle 2) in NC-PDDA-HMWL

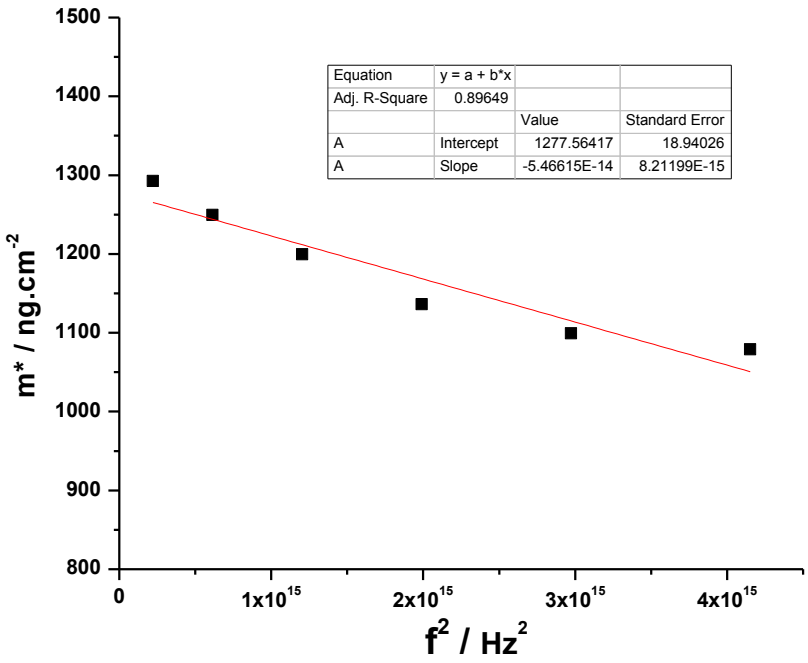


**Figure A 5. 14** Johannsmann model areal mass estimate of PDDA (layer 1; cycle 3) in NC-PDDA-HMWL

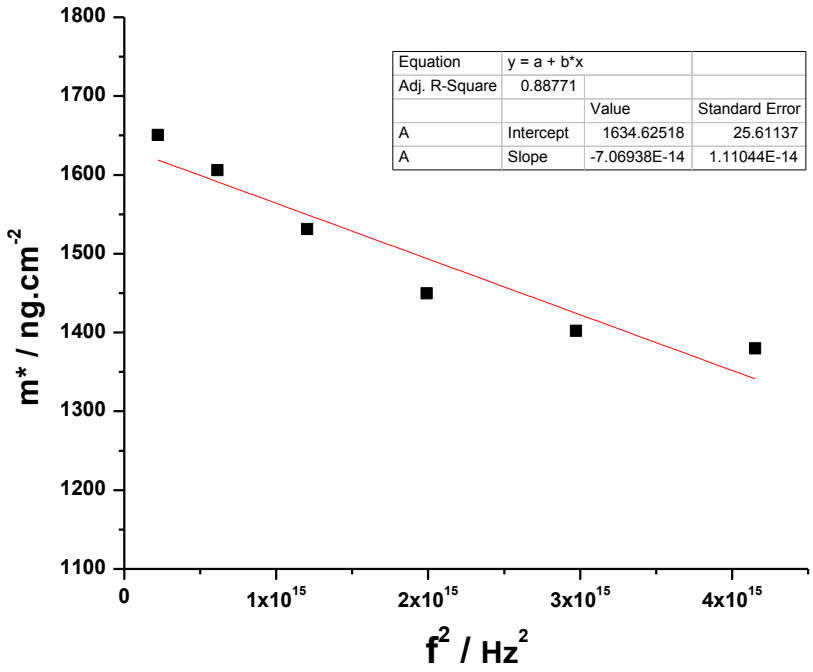


**Figure A 5. 15** Johannsmann model areal mass estimate of HMWL (cycle 3) in NC-PDDA-HMWL

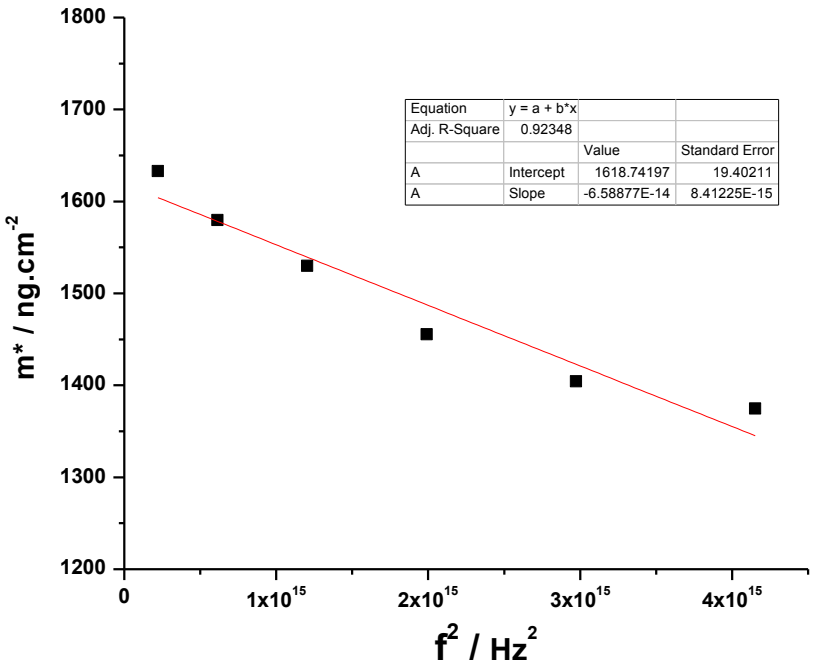


**Figure A 5. 16** Johannsmann model areal mass estimate of PDDA (layer 2; cycle 3) in NC-PDDA-HMWL

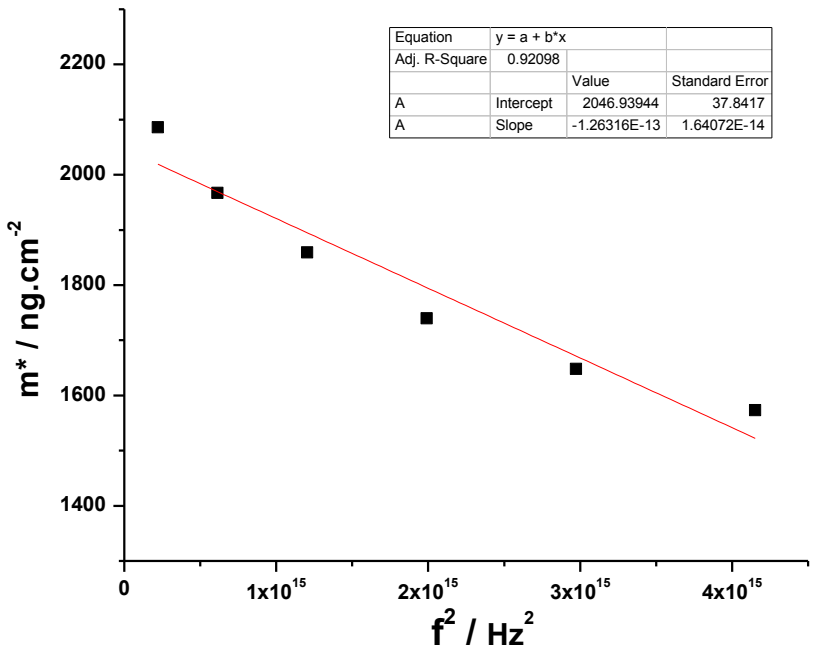


**Figure A 5. 17** Johannsmann model areal mass estimate of NC (cycle 3) in NC-PDDA-HMWL

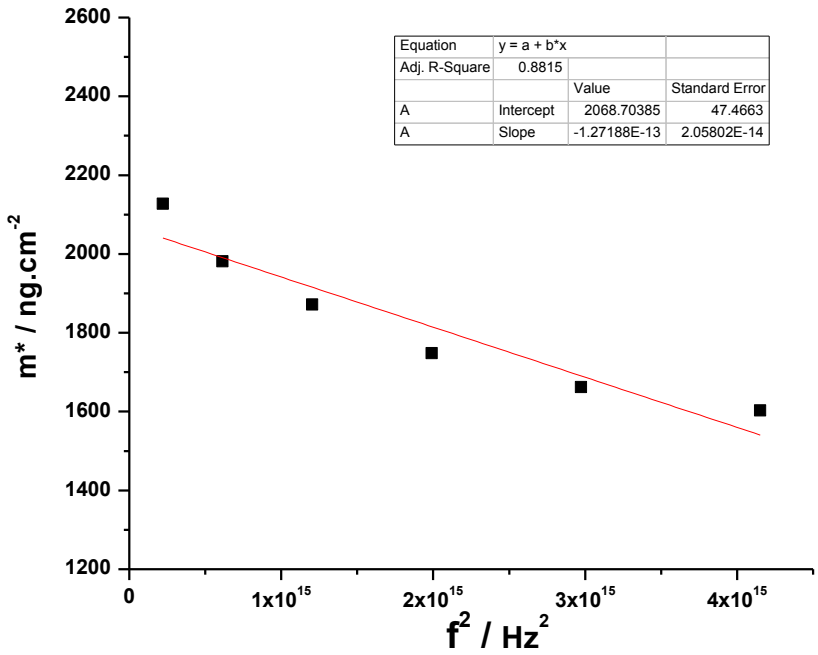


**Figure A 5. 18** Johannsmann model areal mass estimate of PDDA (layer 1; cycle 4) in NC-PDDA-HMWL

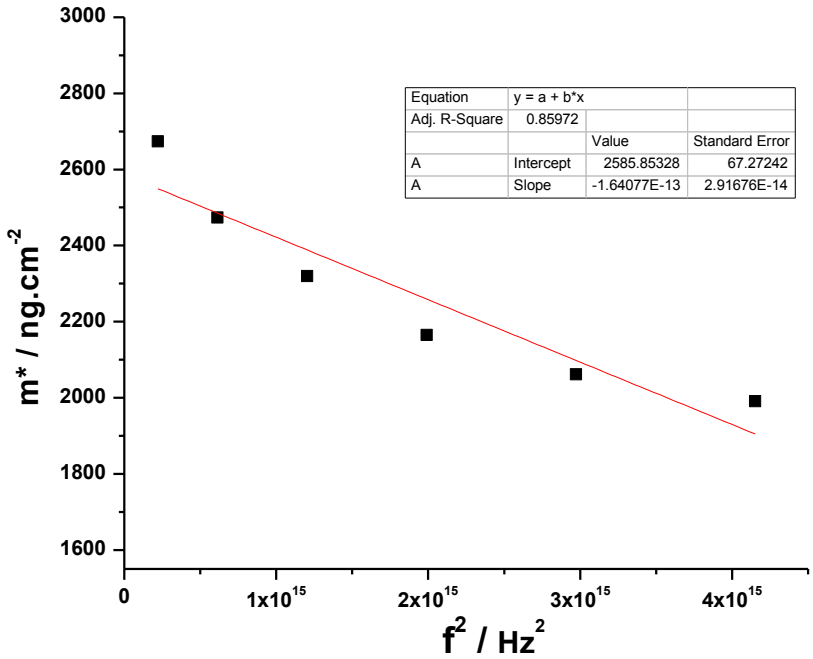


**Figure A 5. 19** Johannsmann model areal mass estimate of HMWL (cycle 4) in NC-PDDA-HMWL

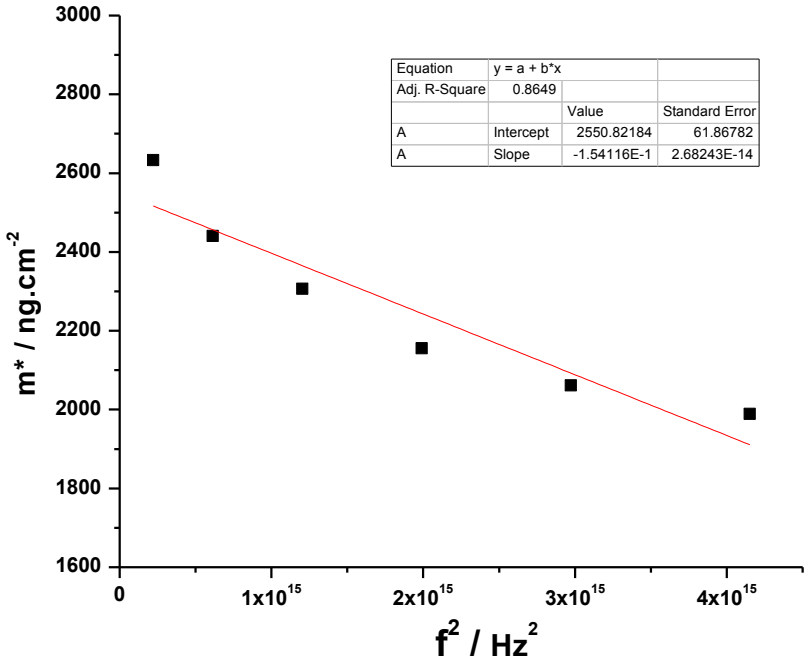


**Figure A 5. 20** Johannsmann model areal mass estimate of PDDA (layer 2; cycle 4) in NC-PDDA-HMWL

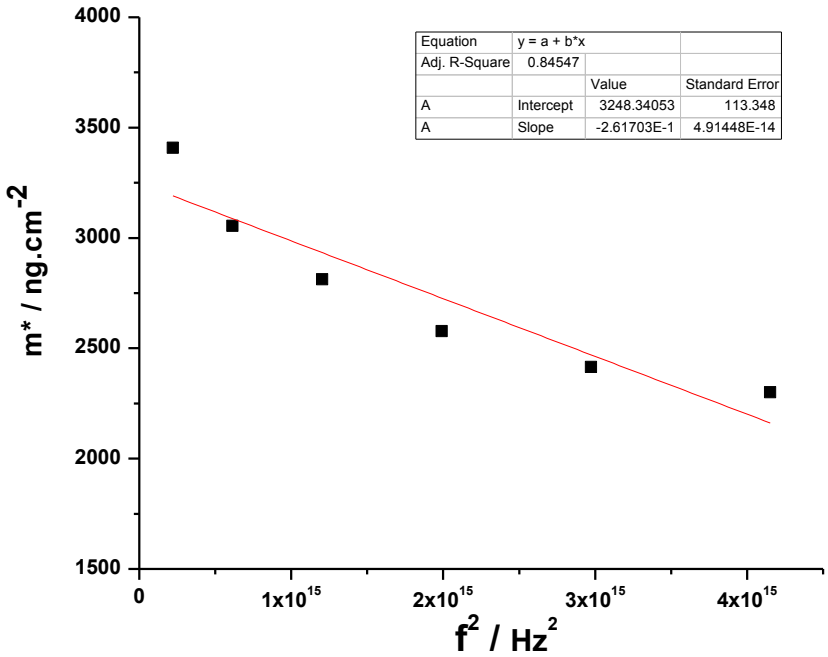


**Figure A 5. 21** Johannsmann model areal mass estimate of NC (cycle 4) in NC-PDDA-HMWL

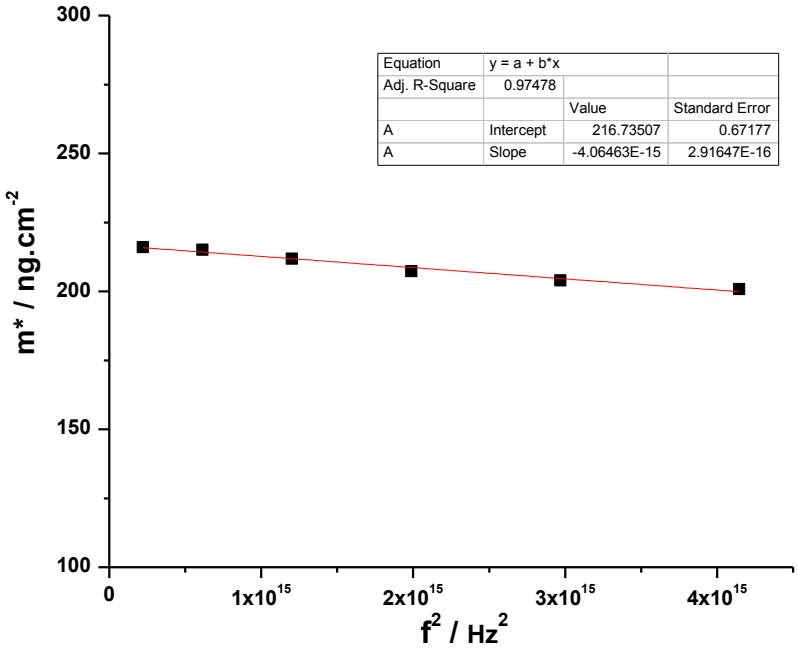


**Figure A 5. 22** Johannsmann model areal mass estimate of PDDA (layer 1; cycle 1) in NC-PDDA-OL

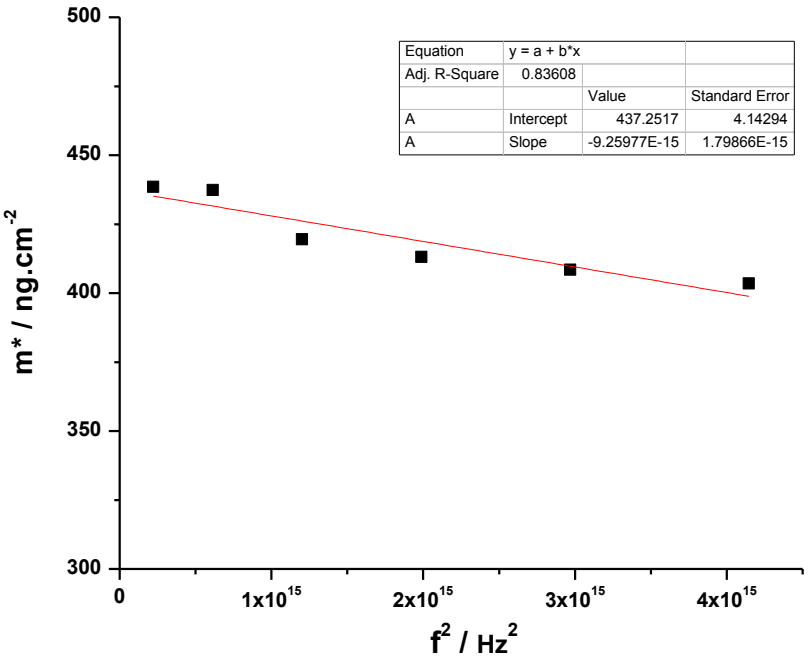


**Figure A 5. 23** Johannsmann model areal mass estimate of OL (cycle 1) in NC-PDDA-OL

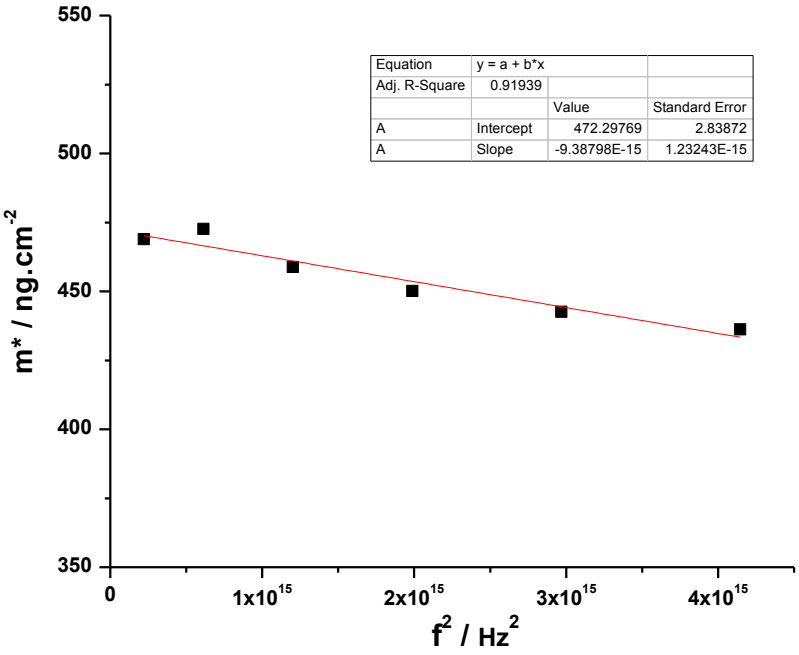


**Figure A 5. 24** Johannsmann model areal mass estimate of PDDA (layer 2; cycle 1) in NC-PDDA-OL

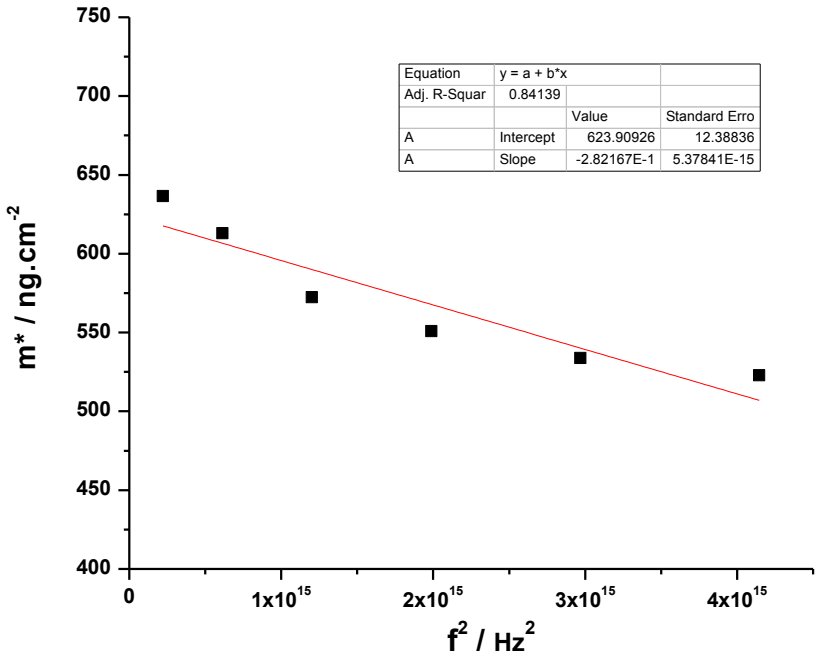


**Figure A 5. 25** Johannsmann model areal mass estimate of NC (cycle 1) in NC-PDDA-OL

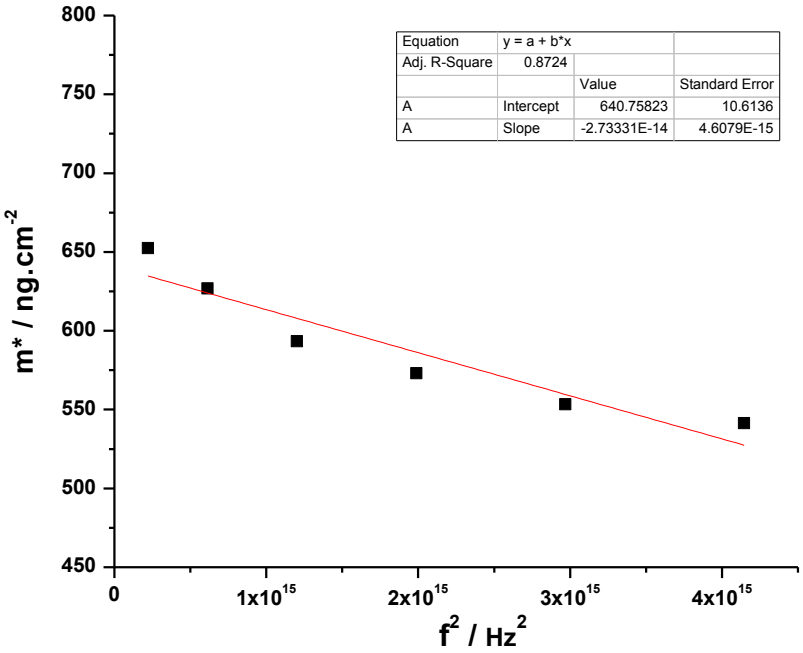


**Figure A 5. 26** Johannsmann model areal mass estimate of PDDA (layer 1; cycle 2) in NC-PDDA-OL

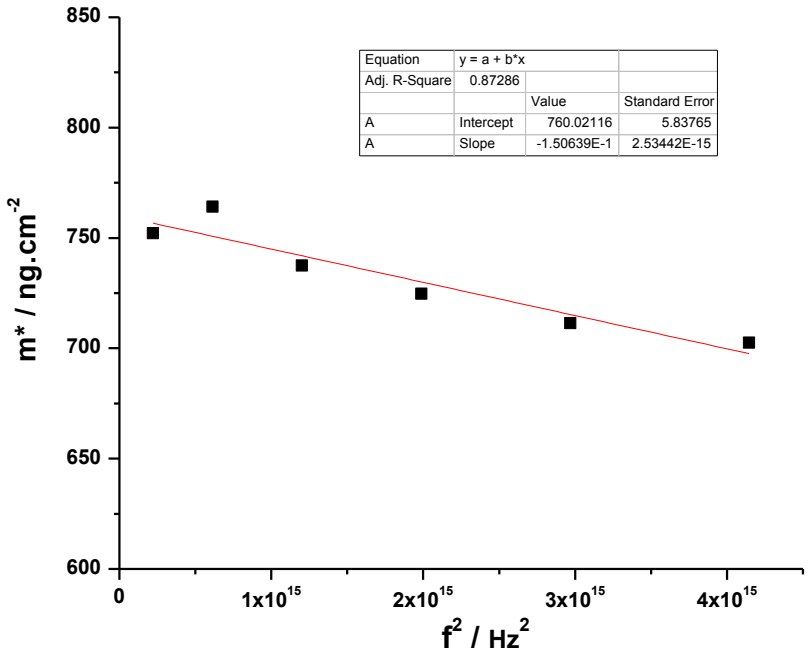


**Figure A 5. 27** Johannsmann model areal mass estimate of OL (cycle 2) in NC-PDDA-OL

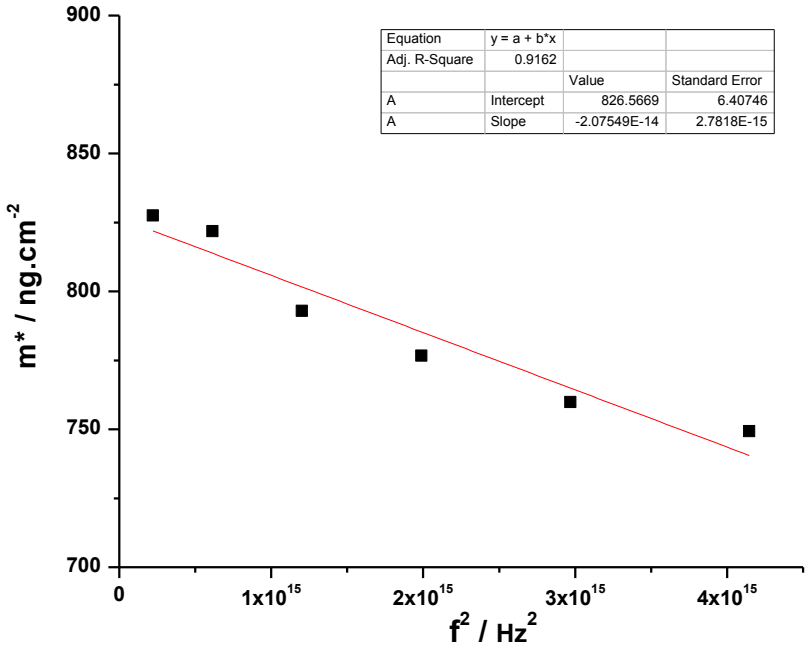


**Figure A 5. 28** Johannsmann model areal mass estimate of PDDA (layer 2; cycle 2) in NC-PDDA-OL

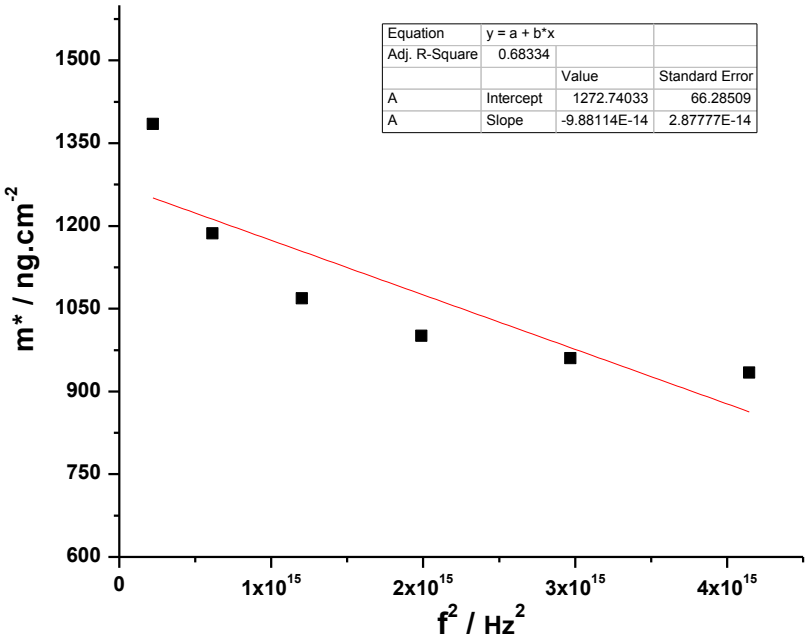


**Figure A 5. 29** Johannsmann model areal mass estimate of NC (cycle 2) in NC-PDDA-OL

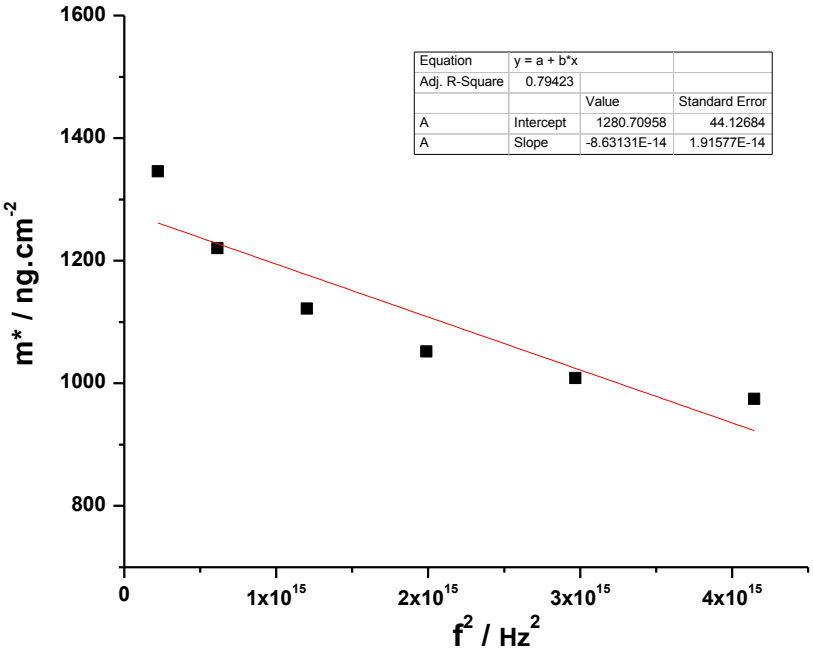


**Figure A 5. 30** Johannsmann model areal mass estimate of PDDA (layer 1; cycle 3) in NC-PDDA-OL

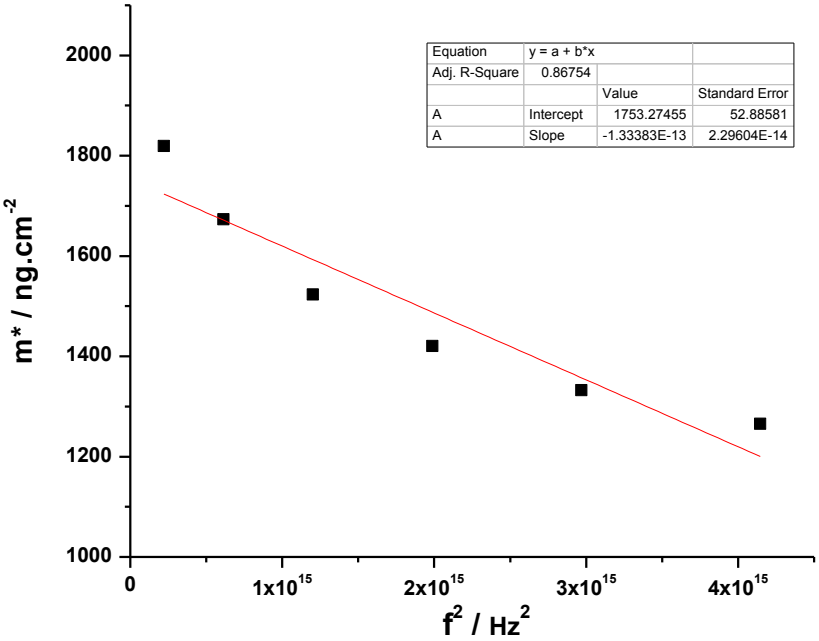


**Figure A 5. 31** Johannsmann model areal mass estimate of OL (cycle 3) in NC-PDDA-OL

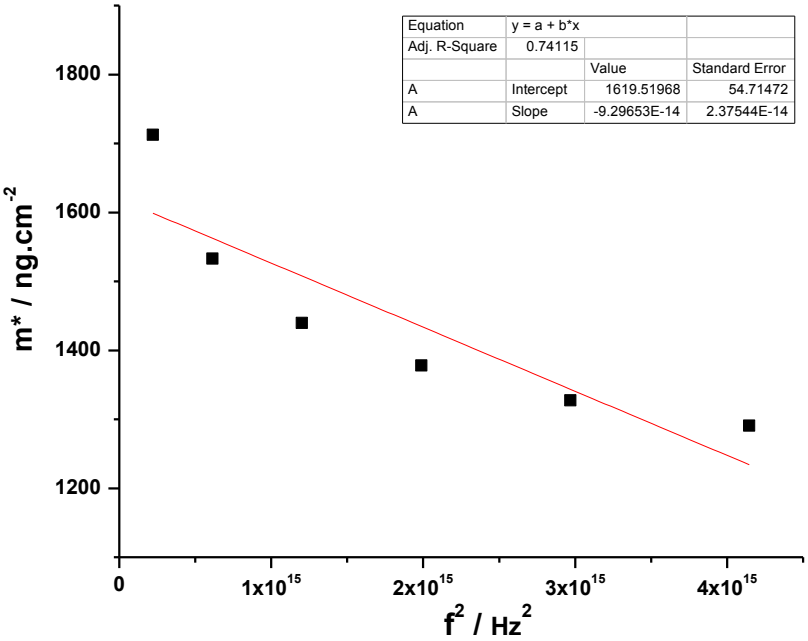


**Figure A 5. 32** Johannsmann model areal mass estimate of PDDA (layer 2; cycle 3) in NC-PDDA-OL

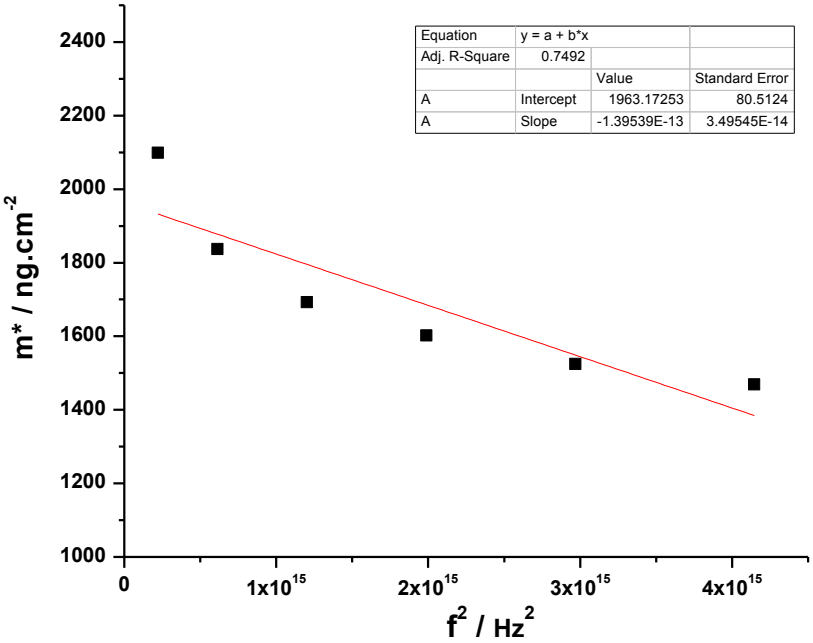


**Figure A 5. 33** Johannsmann model areal mass estimate of NC (cycle 3) in NC-PDDA-OL

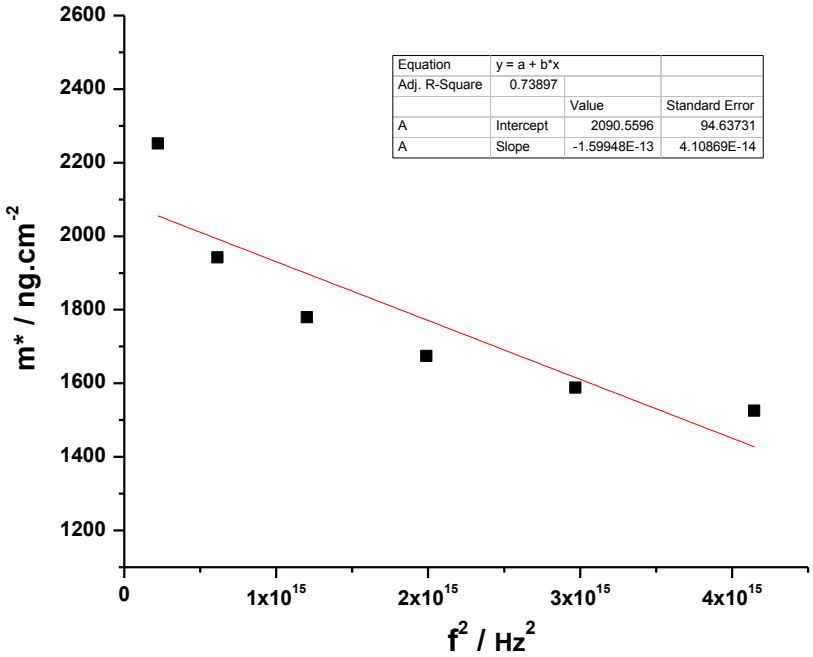


**Figure A 5. 34** Johannsmann model areal mass estimate of PDDA (layer 1; cycle 4) in NC-PDDA-OL

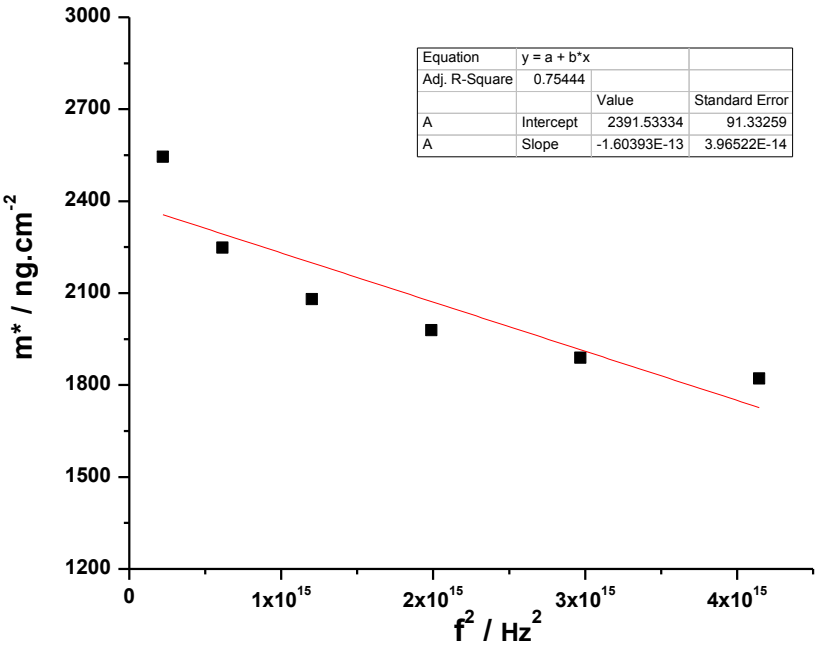


**Figure A 5. 35** Johannsmann model areal mass estimate of OL(cycle 4) in NC-PDDA-OL

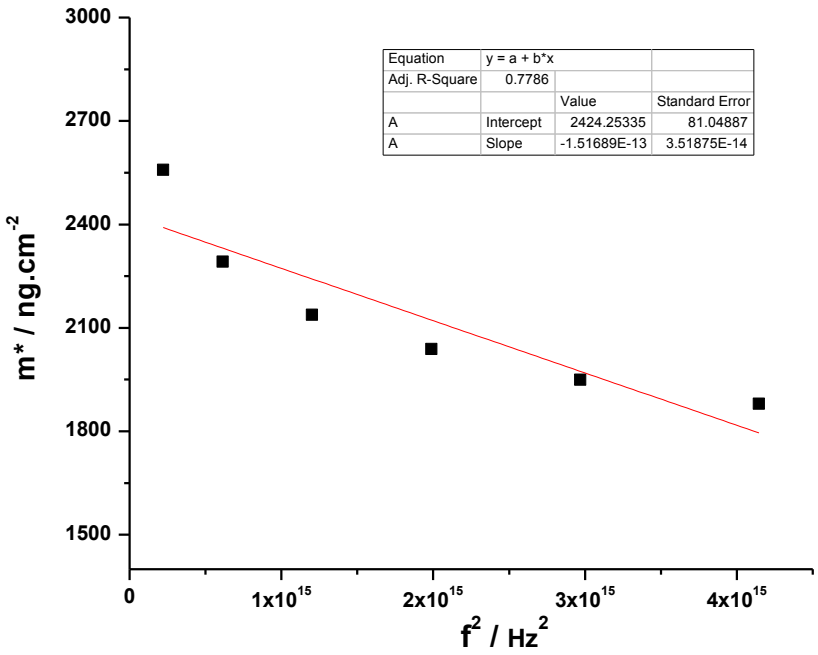


**Figure A 5. 36** Johannsmann model areal mass estimate of PDDA (layer 2; cycle 4) in NC-PDDA-OL

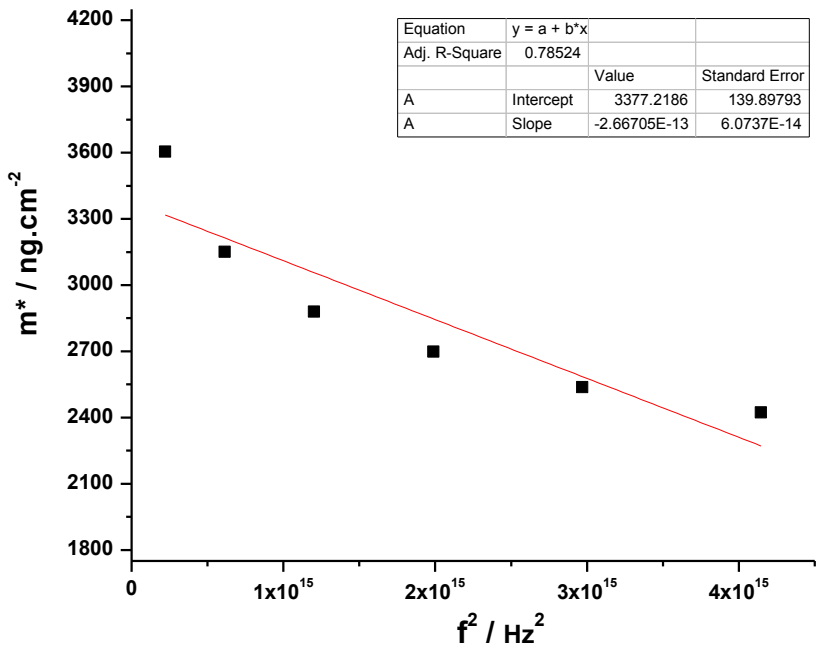


**Figure A 5. 37** Johannsmann model areal mass estimate of NC (cycle 4) in NC-PDDA-OL

## Appendix A 5-6. Ellipsometry Principles

Ellipsometry is a surface sensitive technique which measures the state of polarization of the light reflected from an interface. The fundamental equation for ellipsometry is given by the reflectivity ratio of s and p polarized light:

$$r = r_p/r_s = \mathrm{Re}(r) + i\mathrm{Im}(r) = \tan \Psi \exp(i\Delta) \qquad \text{(A8)}$$

where $\Psi$ and $\Delta$ are the ellipsometric angles. At brewsters angle ($\mathrm{Re}(r) = 0$ or $\Delta = 90º$), equation can be expressed as:

$$\rho = r_p/r_s = i\mathrm{Im}(r) = \tan \Psi \qquad \text{(A9)}$$

where ρ is defined as ellipticity. If the thickness (t) of a film in consideration is much smaller compared to the λ of the light, ρ can be expressed as a power series in terms of t/λ, the first term of which is gives the Drude's equation:[6]

$$\rho = \frac{\pi}{\lambda}\frac{(\varepsilon_1 + \varepsilon_2)^{1/2}}{(\varepsilon_1 + \varepsilon_2)}\int_0^D \frac{(\varepsilon - \varepsilon_1)(\varepsilon - \varepsilon_2)}{\varepsilon}dz \tag{A10}$$

where ε is the dielectric constant at a point z in the thin film, $\varepsilon_1$ is the dielectric constant of the ambient medium, and $\varepsilon_2$ is the dielectric constant of the substrate. If the thin film in consideration has a negligible surface roughness, which means ε is constant with respect to z, equation reduces to the form:

$$t = \frac{\rho}{\frac{\pi}{\lambda}\frac{(\varepsilon_1 + \varepsilon_2)^{1/2}}{(\varepsilon_1 - \varepsilon_2)}\frac{(\varepsilon_1 - \varepsilon_2)(\varepsilon - \varepsilon_2)}{\varepsilon}} \tag{A11}$$

The ε of the films were determined the refractive index (n), since $n = (\varepsilon\mu)^{1/2}$, and where the relative permeability μ is unity for naturally occurring materials. The refractive index of NC:PDDA:HMWL and NC:PDDA:OL were determined by an Abbe refractometer to be 1.53 and 1.56 rspectively.

## Appendix A 5-7. References


1. Saito, T.; Isogai, A. *Cellulose Communications* **2004**, *11*, 192-196.
2. Saito, T.; Kimura, S.; Nishiyama, Y.; Isogai, A. *Biomacromolecules* **2007**, *8*, 2485-2491.
3. Li, Q.; Renneckar, S. *Cellulose* **2009**, *16*, 1025-1032.
4. Saito, T.; Shibata, I.; Isogai, A.; Suguri, N.; Sumikawa, N. *Carbohydrate Polymers* **2005**, *61*, 414-419.

5. Voinova, M. V.; Rodahl, M.; Jonson, M.; Kasemo, B. *Physica Scripta* **1999**, *54*, 391-396.

6. Drude, P., *Ann. Phys.* **1889**, 36, 532-560.

## Appendix A 6-1. Loss Modulus Curves

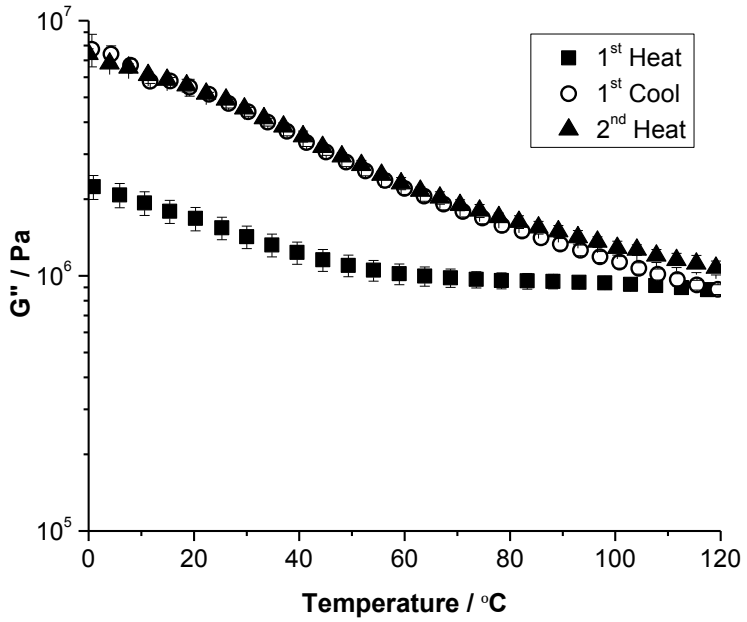


**Figure A 6. 1** Average DMA loss modulus (G') curves of blended cast films of NC-OL-PDDA in heat-cool-heat experiment at 1.0 Hz (error bars represent ± 1standard deviation; n = 3)

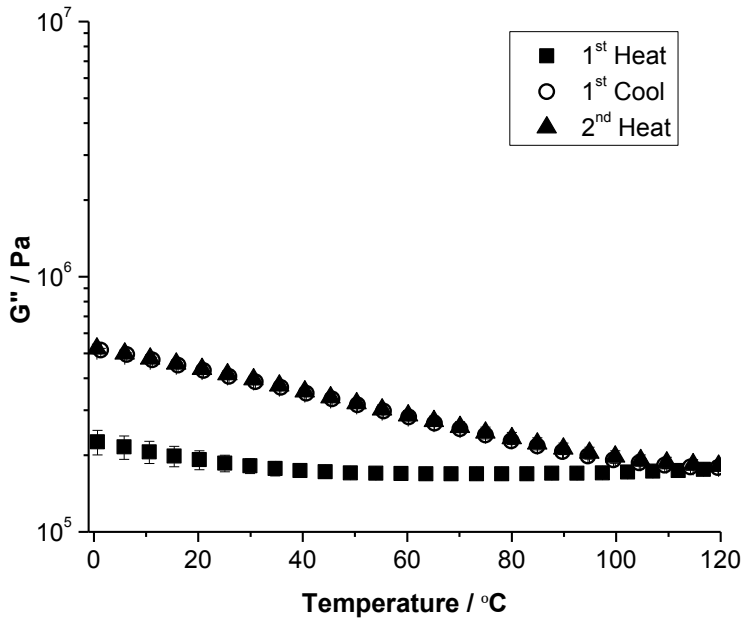


**Figure A 6. 2** Average loss modulus (G') curves of cast films of NC in heat-cool-heat experiment at 1.0 Hz (error bars represent ± 1standard deviation; n=3)

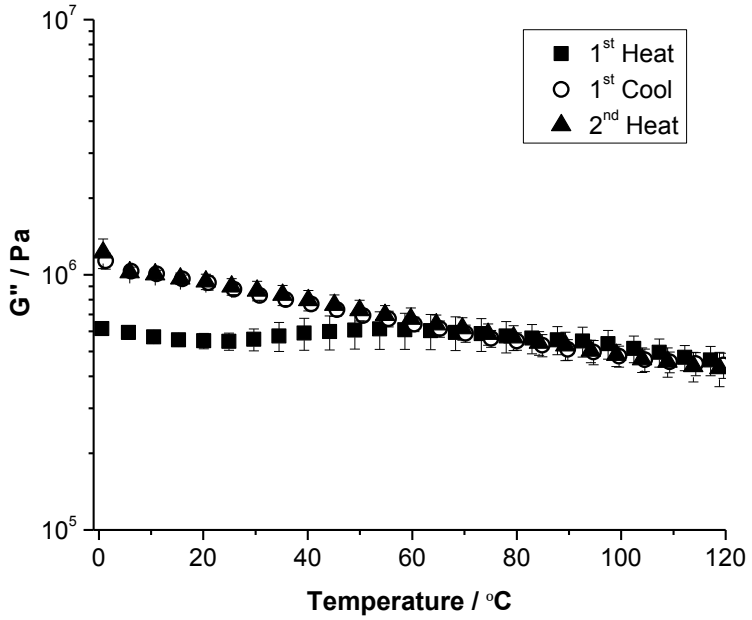


**Figure A 6. 3** Average loss modulus (G') curves of LbL films in heat-cool-heat experiment at 1.0 Hz (error bars represent ± 1standard deviation; n=3)

## Appendix A 6-2. Loss Modulus TTSP Curves

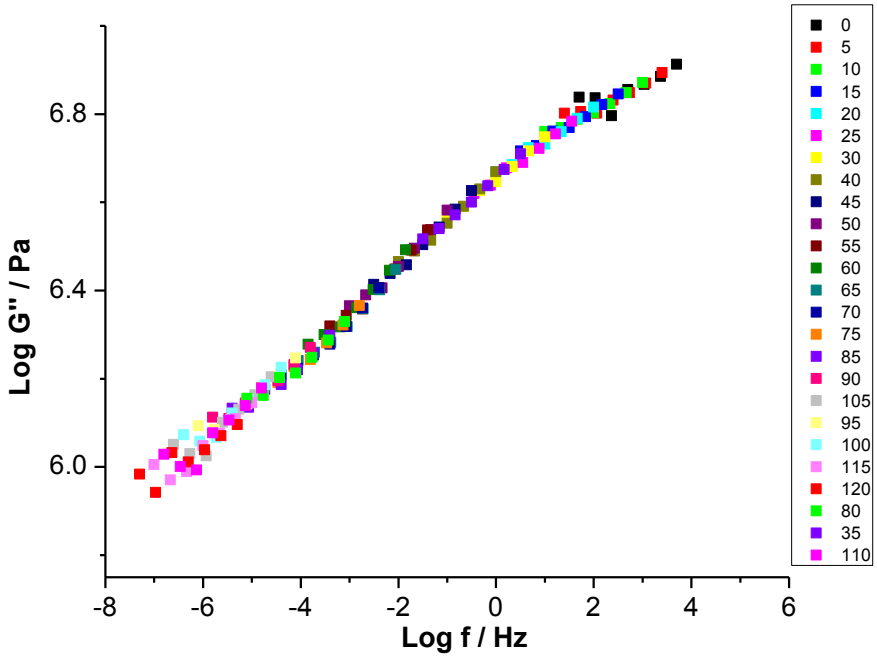


**Figure A 6. 4** Loss modulus master curve of NC-OL-PDDA films

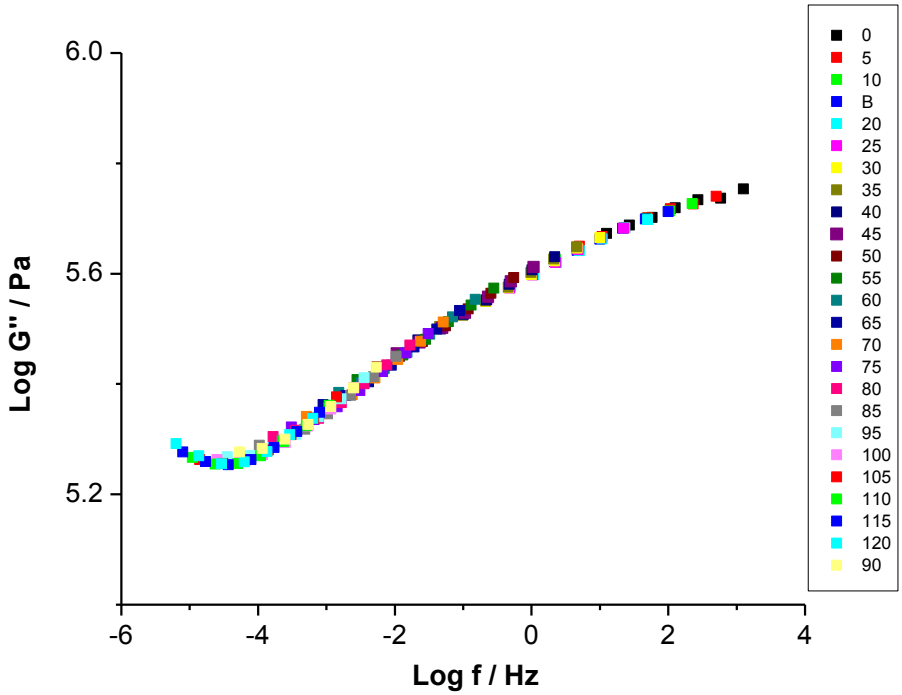


**Figure A 6. 5** Loss modulus master curve of NC films

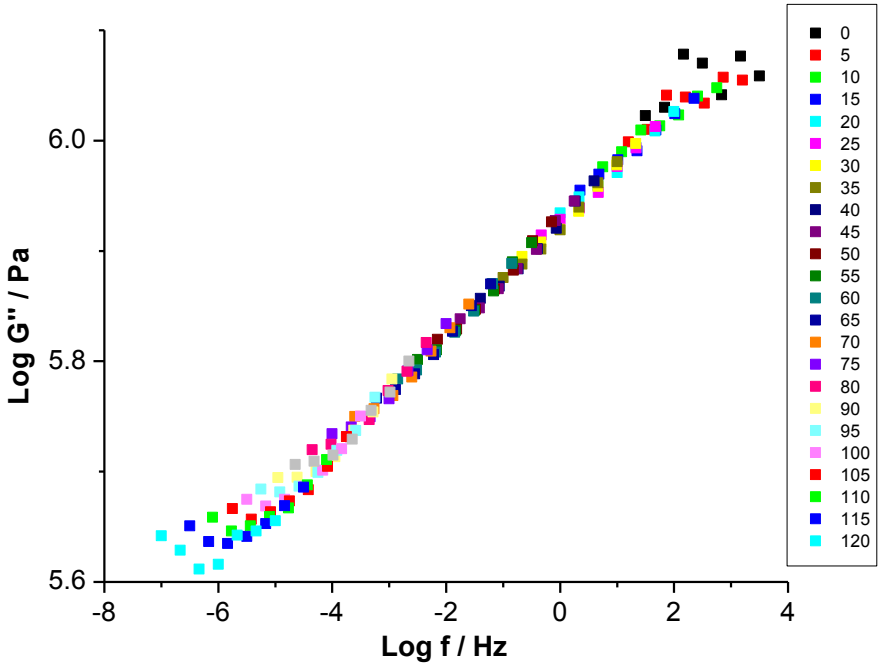


**Figure A 6. 6** Loss modulus master curve of LbL films

## Appendix A 6-3. DSC Thermograms

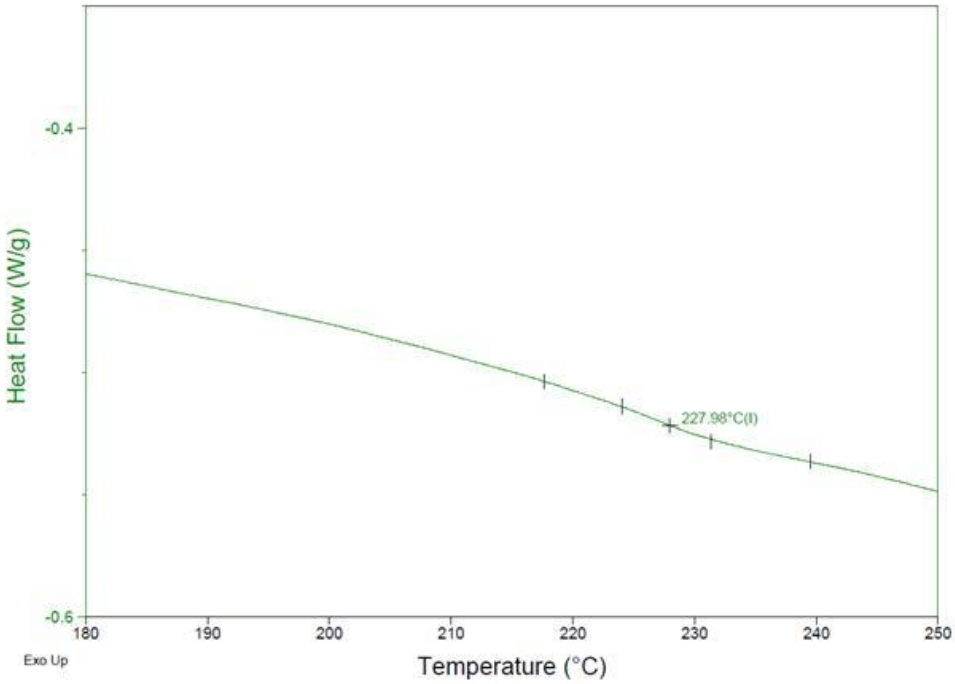


**Figure A 6. 7** DSC thermogram of PDDA in second heat (heating rate 10 ºC $min^{-1}$)

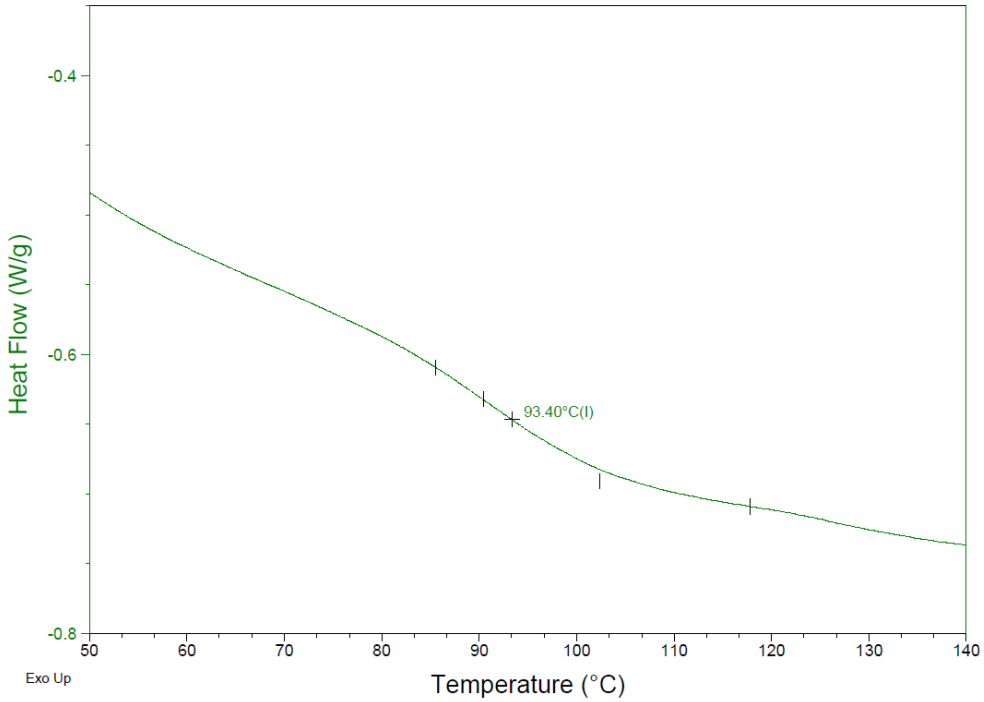


**Figure A 6. 8** DSC thermogram of OL in second heat (heating rate 10 ºC $min^{-1}$)